University of Birmingham

Thesis

Experimental set-up for realising long-range interaction using strontium atoms in an optical lattice

Author:
Marco Menchetti

Supervisor:
Prof. Kai Bongs
Dr. Yeshpal Singh

Abstract

Ultracold interacting gases represent a new and exciting frontier for technological applications, such as quantum information processing, and they also offer an ideal test bench for condensed matter systems.

This work examines the case of atoms in the alkaline earth metal family. These atoms can exhibit long-range dipolar interactions, generated via coherent exchange of photons on the $^3P_0 \rightarrow {}^3D_1$ transition. In particular, the progress in realising an experiment to study this coherent exchange of atoms in bosonic strontium is discussed. A review of the experimental techniques developed over the last 50 years to cool, manipulate and study atoms and molecules used in long-range interaction experiments is given from a historical viewpoint. Techniques to laser cool and trap atomic strontium are described, and a novel study of different geometries for magneto-optical traps (MOTs) is presented.

This thesis describes the long-range interaction strontium experiment under development at the University of Birmingham. In particular, the characterisation of a self assembled Zeeman slower is presented, along with a novel repump scheme for the first stage of cooling using the $^3P_0 \rightarrow {}^3D_1$ transition.

This work also reports the use of the $^3P_1 \rightarrow {}^3S_1$ transition to populate the $^3P_0$ level, and the realisation of a monolithic (Interference Filter External Cavity Diode Laser) IFECDL.

The new techniques that I present here have the potential to facilitate future studies of long-range interaction in strontium and other cold atoms experiments.

Acknowledgements

I would like to start by thanking my parents Massimo and Natascia and all the rest of my family who always supported me over all those years. Thank you to my colleagues for the company and support and especially thanks to David, Johnny J. and B., Matt, Richard and Chang for proofreading this thesis, without you it would have been a mess. Thank you to my supervisors Kai and Yeshpal to give me this opportunity. Thank you to my brother because if not, it looks bad. Thanks to Ian, Richard and William that welcomed me at NPL when I could barely speak English. Thank you to Valentina for helping me to move here four years ago. Thanks to my friends Ily and Sara who always make me feel as I never left when I go back home. Thank you to DSTL that funded my PhD and allowed me to be here. Thank you to all the people at the quantum HUB, Physics East and NPL for welcoming me. A special thanks to my girlfriend Liisa who bore me along this voyage and always helped me when I needed it.

Ringraziamenti

Vorrei iniziare ringraziando i miei genitori Massimo e Natascia e tutto il resto della mia famiglia che mi ha sempre sostenuto in tutti questi anni. Grazie ai miei colleghi per la compagnia e il supporto e soprattutto grazie a Davide, Giovanni J. e B., Mattia, Riccardo e Ciang per la correzione di questa tesi, senza di voi sarebbe stato un casino. Grazie ai miei supervisori Cai e Iespal per darmi questa opportunità. Grazie a mio fratello perché se no, sta brutto. Grazie a Giovanni, Riccardo e Guglielmo che mi hanno dato il benvenuto all'NPL quando riuscivo a malapena a parlare inglese. Grazie a Valentina che mi aiuta a trasferirmi qui quattro anni fa. Grazie ai miei amici Ily e Sara che mi fanno sempre sentire come non me ne sono mai andato quando torno a casa. Grazie a DSTL che finanzia il mio dottorato di ricerca e mi ha permesso di essere qui. Grazie a tutte le persone del Quantum HUB, Physics East e NPL per avermi dato il benvenuto. Un ringraziamento speciale alla mia ragazza Liisa che mi sostenuto lungo questa viaggio e mi ha sempre aiutato quando ne ho avuto bisogno.

Contents

List of Figures

CHAPTER 1

Introduction

As a brain is more than the sum of its cells, the behaviour of interacting atoms is much richer than a simple multitude of isolated particles. As the number of interacting particles grows the complexity of such systems grows exponentially, and many aspects of these highly interactive systems have not yet been fully understood.

The discipline which studies these systems is called 'many-body physics'. Over the last decades, advancements made in cold atoms experiments have allowed the creation of a controlled environment, where it is possible to selectively tune the interaction between the particles forming the system, allowing the generation of an ad hoc benchmark to study many-body physics [1, 2].

Furthermore, some of those interactions can be used to overcome some of the limits of modern technology. In particular, the study of an atomic system with long-range interaction is essential to the field of quantum information, since it allows the realisation of entangling gate operations among distant qubits [3–5].

There are four approaches currently used to achieve long-range interaction in cold atoms: using atoms with large magnetic dipole moment (such as chromium) [6], using polar molecules [7], using Rydberg atoms [8] or light-induced dipoles [9–11]

In this thesis we focus on the latter. Light induced dipoles are based on the coherent exchange of photons between atoms. In the case of the experiment that I worked on during my PhD and that is reported in this thesis, the coherent

exchange uses the ${}^3P_0 \rightarrow {}^3D_1$ transition of strontium atoms to realise and study mixtures of hard-core lattice bosons that feature long-range interactions [12]. Presented in this thesis is the progress made so far in this experiment.

1.1. Brief history of long-range interacting cold atoms

First described in 1975 by T. W. Hänsch and A. L. Schawlow [13] and then experimentally demonstrated in 1978 by D. J. Wineland, R. E. Drullinger and F. L. Walls [14], the cooling of atoms by laser radiation signalled the start for cold atoms and molecules physics. In Wineland's article is demonstrated for the first time that it is possible to cool down Mg^{+2} ions to 50 K using radiation pressure like the one produced by lasers.

Four years later, in 1982, W. D. Phillips and H. Metcalf showed that the cooling could be applied to neutral atoms as well [15]. In this article Phillips and Metcalf used what will be called a Zeeman slower (see ch. 2.2.1) to keep the atoms in resonance with the laser, which allowed them to slow down the atoms to 40% of their initial velocity.

In 1986 S. Chu et al. were able to trap atoms using dipole force [16] and in the following year the first magneto optical trap (MOT) was realised [17].

C. Cohen-Tannoudj, S. Chu and W. D. Phillips were awarded the Nobel price in physics in 1997 for their work on atoms cooling [18]. In the 1980s the physics community put great effort in the study of highly excited states, e.g. Rydberg states [19].

In 1995 the first Bose-Einstein condensate (BEC) was realised by evaporative cooling [20]. With the realisation of BEC, cold atoms systems were considered as a promising tool to study many-body physics [21]. In a BEC the density of the atoms is several order of magnitude higher than in a MOT, the resulting reduction of interatomic distance enabled researchers to study now interactions that were too weak to be noticed before.

1998 was the year when J. Weinstein and colleagues trapped polar molecules in a MOT for the first time [22]. In the same year, Rydberg gas was cooled and trapped as well [23, 24].

A few months later, in 1999, B. DeMarco and D. S. Jin obtained the first Fermi degenerate gas [25].

In 2001 it was proposed theoretically to utilise the dipole blockade generated by Rydberg atoms to process quantum information [26]. The dipole blockade was demonstrated eight years later by A. Gaëtan et al. [27]. In the following

year L. Isenhower et al. realised a NOT gate using Rydberg atoms[3] for the first time.

In 2002 a Mott insulator was realised using ^{87}Rb in an optical lattice [28]. In this experiment it was possible to confine a single atom in a lattice site where motion of atoms across lattice sites was prohibited, making the system more similar to a crystal than an atomic cloud.

The techniques of photoassociation and Feshbach-resonance were demonstrated in 2004 [29, 30] enabling the creation of cold molecules starting from cold atoms, and in 2009, molecules formed by Rydberg atoms were demonstrated [31, 32].

J. F. Sherson et al. showed a single atom resolution in a Mott insulator in 2010 [33]. In the following year, J. Struck and colleagues demonstrated how it is possible to use atoms trapped in a 2D lattice to simulate the magnetic properties of solid state matter [34].

In more recent years the cold atoms community has concentrated its efforts on a number of subjects, such as the integration of cold atoms and solid state devices [35–37] and the study of subradiance [38]. Apart from the two aforementioned research areas, extensive studies have been made on the use of polar atoms and molecules for quantum simulation [39] as well as researching the possibility of using the long range interaction to enhance the performance of metrological quantum devices [40]. Great efforts are also directed to the integration of atoms and molecules with long range interaction in an optical cavity [41–43].

1.2. Long-range interactions in strontium

A strontium (Sr) atom in its ground state ($5s^2\,{}^1S_0$) does not have any multipole moment, this means that for a dilute gas (average distance between atoms $\approx 100\,\mathrm{nm}$) it is possible to use shape-independent approximation, where the interaction between atoms are treated as a delta function [44]. Long range interaction effects are only possible by the coherent exchange of photons, allowed for by the rich electronic structure of Sr. In bosonic strontium, the transition between the states $5s5p^3P_0$ and $5s4d^3D_1$ has a wavelength of $\lambda = 2.6\,\mu\mathrm{m}$ and a transition dipole moment of 4.03 D [45].

The magic wavelength[1] for this transition is found to be at 430 nm (see

[1] A magic wavelength is the wavelength that has the same AC polarisability for both states that allows trapping the atoms in a dipole trap without perturbing the transition.

ch.2.5.3). A laser at this wavelength can be used to create a blue detuned lattice with lattice spacing $a = \lambda/2$.

Combining small interatomic distance[2] and long wavelength[3] leads to dipolar interaction [46]. An atom that absorbs a photon will re-emit it soon after. However, the photon can be adsorbed again by a neighbouring atom an so on, creating thus interactions between distant atoms.

To understand the effects of the long-range interaction on strontium atoms, consider a 1D chain of atoms trapped in a periodic lattice with interatomic spacing a. If we assume that the atoms interact weakly with the environment, an atom in this chain is excited by a photon, the evolution of the system is given by the master equation of the density matrix ρ,

$$\dot{\rho} = -\frac{i}{\hbar}[H, \rho] + D(\rho). \tag{1.1}$$

The first term describes how the excitation moves along the chain, while the second describes how it dissipates. A detailed description of the master equation is out of the scope of this thesis; more details can be found in [45–47]. In general, the dissipative effect decreases for transitions with longer wavelength and for chains with smaller interatomic spacing. Using the transition between the $^3P_0$ and the $^3D_1$ states and a=215 nm, the excitation lifetime is longer than the decay rate of the single atom [45].

In the specific case of the $^3P_0 \rightarrow^3 D_1$ transition of strontium atoms, the interaction between atoms has a strength comparable with the one between polar molecules (e.g. KRb[48] or LiCs[49]), that is 3 orders of magnitude stronger than the one among atoms with large magnetic dipole moments like Cr[6]. Although this interaction is much weaker than the one produced by Rydberg atoms [21], the coherent exchange of photons uses long-lying states and is less sensitive to external magnetic fields. This, plus the high number of particles[4], make this experiment an interesting experiment for the study of long-range interacting atomic system.

[2]Distance between the atoms smaller than the dipole length $l_d = Md^2/(4\pi\epsilon_0\hbar^2)$ where M is the reduced mass, d is the dipole moment [21].

[3]Longer than several lattice sites.

[4]compared with polar molecules

1.3. Effect of long range interaction in strontium spectroscopy

To show that the effect of the long range interaction, we can perform spectroscopy of this transition. Let's start by considering the effect of the dipolar interaction between two atoms. The spectrum of the radiation emitted during a transition of the first atom will be modified by the presence of the second atom and vice versa. This can be represented by the following equation:

$$S(\omega) \propto \frac{1}{(\omega - \omega_a - W_{12})^2 + (\Gamma + \Gamma_{12})^2/4}, \tag{1.2}$$

with

$$W_{12} = \frac{3\Gamma}{4}\left[y_0(kd) - \frac{y_1(kd)}{kd}\right] \qquad \text{and} \qquad \Gamma_{12} = \frac{3\Gamma}{2}\left[j_0(kd) - \frac{j_1(kd)}{kd}\right],$$

where $\omega = kc$ is the frequency of the laser, $\omega_a = k_a c$ is the frequency of the transition and Γ its linewidth, d is the distance between the two atoms, j_n and y_n are the nth order spherical Bessel function of the first and second kind respectively. This translates to a shift towards a higher frequency and a broadening of the transition linewidth [50, 51].

There is no analytic solution for systems more complex than two atoms, but it is possible to calculate the spectrum numerically [45]. The results display a more pronounced shift and broadening than in the case of two atoms, along with the appearance of narrow peaks belonging to long-lived subradiant states [52].

1.4. Contributions of the author

This thesis is based on the work I performed over the four years of my PhD. During this period I performed a study of several geometries for the cooling and trapping of cold atoms (ch. 3). I also built and characterised majority of the experiment described here. In particular, I worked on the first demonstration of the use of self-assembled Zeeman slower in cooling atoms (ch. 5). I demonstrated the use of a 2.6 μm laser as repump for the first stage of cooling of strontium atoms (ch. 5), and I designed, built and tested a monolithic interference filter external cavity diode laser (IFECDL) (ch. 4).

Although this experiment did not allow me to study the effect of long-range interaction in strontium atoms, my work established strong foundation to these studies. The experiment will continue at the University of Birmingham and

the first scientific results are expected to arrive within the next year.

1.5. Outline of the thesis

A brief overview of the long-range interaction effect on strontium atoms and an examination of the latest developments in the field has been provided in this introduction. The remainder of this thesis is structured as follows:

- **In Chapter 2** the basis on which the cooling and trapping of strontium atoms is founded are presented.
- **In Chapter 3** a numerical study of three different geometries for magneto optical trap that are used in cold atoms experiments is presented, along with their feasibility in the use of this particular experiment.
- **In Chapter 4** the experiment is described along with the characterisation of its components.
- **In Chapter 5** the measurements done on the atomic samples are presented.

Finally, **in Chapter 6**, the thesis concludes with an outlook for the future prospects of the long-range interaction experiment at the University of Birmingham.

CHAPTER 2

Cooling and trapping of strontium atoms

2.1. Strontium

Strontium is an alkaline earth metal. It reacts readily when in contact with air, forming strontium oxide (SrO) and, in lower concentrations, Strontium hydroxide ($Sr(OH)_2$). As a result, handling and storage must be performed in an inert environment (vacuum, Nitrogen, Argon or oil). Strontium is sold commercially as a pure element in its dendritic form. Its ground state configuration is $5s^2$ and the element occurs in nature as three different bosonic isotopes (^{84}Sr, ^{86}Sr and ^{88}Sr) and as a fermionic isotope ^{87}Sr.

Atomic mass (au)	Nuclear spin	Natural abundance (%)	Elastic cross section (a_0)
84	0	0.56	123
86	0	9.86	800
87	9/2	7.00	96
88	0	82.58	-2

Table 2.1: Natural abundance of Sr isotopes and elastic cross section with itself. [53]

The energy level structure of strontium, shown in fig. 2.1, leads to its use in several studies of atomic physics, especially in metrology [54] and in interferometry [55]. In particular the ${}^1S_0 \rightarrow {}^1P_1$ and the ${}^1S_0 \rightarrow {}^3P_1$ transitions, both relatively easy to reach with modern lasers, allow for Doppler cooling of strontium to a temperature of a few hundred nK [56]. The large elastic cross section (see tab. 2.1) enables the formation of Bose-Einstein condensates for ^{84}Sr, ^{86}Sr and degenerate Fermi gases for ^{87}Sr. Although the cross section of pure ^{88}Sr does not allow the formation of a BEC, it is possible to condense it via sympathetic cooling [53, 57]. The natural abundance of ^{88}Sr makes it simple to obtain a large magneto-optical trap (MOT) using this isotope, which is why it has been chosen for use in this experiment.

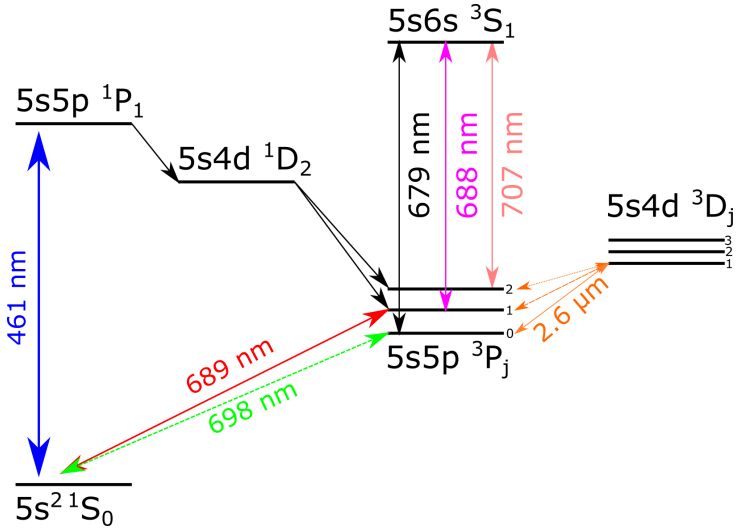

Figure 2.1: Relevant energy levels of ^{88}Sr used in this thesis, more detail of the transitions can be found in tab. 2.2.

2.1.1. Strontium source

At room temperature Sr is solid. Before it can be used in atomic spectroscopy experiments it needs to be transformed to a gas, and an oven is usually used for this purpose. The number of atoms produced by an oven depends on the vapour pressure of the substance inside [58] and this pressure is well described by the Antoine equation [59]:

$$\log_{10} p = A - \frac{B}{C + T}, \tag{2.1}$$

Transition	Wavelength (nm)	Transition rate ($10^6 s^{-1}$)	$I_{sat}(mW/cm^{-2})$
${}^1S_0 \rightarrow {}^1P_1$	460.86	190.01	40
${}^1S_0 \rightarrow {}^3P_1$	689.45	0.0469	3×10^{-3}
${}^1S_0 \rightarrow {}^3P_0$	698.40	-	-
${}^3P_0 \rightarrow {}^1D_1$	2603.1	0.4587	5.4×10^{-4}
${}^3P_2 \rightarrow {}^3S_1$	707.21	39.73	2.3
${}^3P_1 \rightarrow {}^3S_1$	688.02	25.89	1.7
${}^3P_0 \rightarrow {}^3S_1$	679.29	8.90	0.6

Table 2.2: ^{88}Sr transitions relevant for this project.

where A, B and C are constants specific to each substance, and T is the temperature in °C.

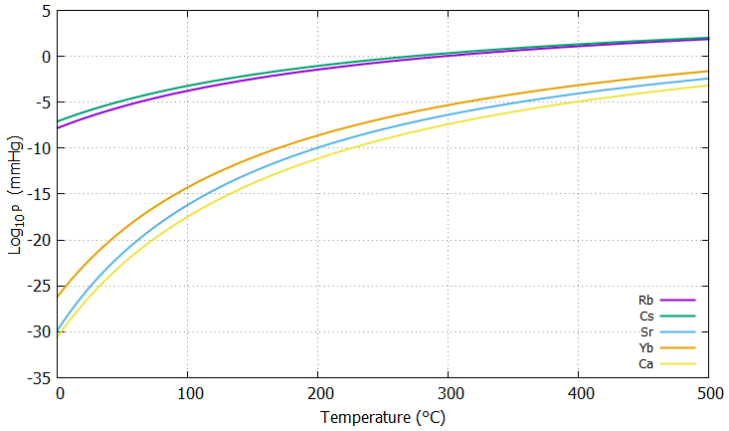

Figure 2.2: Vapour pressure of commonly used elements in cold atoms experiments [60], as calculated with eq. 2.1.

Compared with other common elements used in cold atoms experiments, strontium's vapour pressure is low at room temperature (see fig. 2.2); this means that high temperatures are required to achieve a useful flux of atoms. Increasing the temperature has the consequence of increasing the velocity of the atoms emitted from the oven. The horizontal velocity distribution of the atoms outside the oven is well described by the Maxwell Boltzmann distribution [61]:

$$P(v) = \left(\frac{m}{2\pi k_B T}\right)^{3/2} 4\pi v^2 e^{-\frac{mv^2}{2k_B T}}. \tag{2.2}$$

Let us now consider the effect that this velocity distribution has on the frequency of the atomic transition: when an atom moves with velocity v respect the system of reference of the laboratory its transitions will be shifted due to the Doppler effect:

$$\Delta f = f_0(1 + \frac{v}{c}), \tag{2.3}$$

where c is the speed of light, and f_0 the frequency of the transition. Since each atom has a different velocity from the others, combining eq. 2.2 and 2.3 it is easy to see that the measured linewidth of a transition depends on the temperature of the atoms (Doppler broadening):

$$\sigma_f = \sqrt{\frac{K_B T}{mc^2}} f_0, \tag{2.4}$$

where m is the mass of the atom.

In a typical Sr experiment, the temperature of the oven is around 800 K, that translates in a Doppler broadening of $\approx$ 800 MHz for the ${}^3P_0 \rightarrow {}^1 D_1$ transition. In contrast the interaction between atoms shifts the transition by a few kHz. It is then clear that the first goal of this experiment is to reduce Doppler broadening by decreasing the temperature of the atoms. This is done via laser cooling.

2.2. Light matter interaction

When a stream of photons with wave-vector $\vec{k}$ interact with an atom of mass m, each photon exchanges momentum equal to $\hbar\vec{k}$ that leads to a recoil velocity for the atom:

$$\vec{v_r} = \frac{\hbar\vec{k}}{m} \tag{2.5}$$

When the atom re-emits the photon it has a near even probability of emitting in any direction providing a momentum exchange to the atom in the opposite direction. Over many atom-photon interactions the average emission direction becomes isotropic, resulting in a zero net change in velocity due to photon emission, and an overall deceleration along the vector of the photons due to photons absorption:

$$\vec{a} = \frac{\vec{F}}{m} = P\frac{\vec{v_r}}{\tau} = P\frac{\hbar\vec{k}}{m\tau} \tag{2.6}$$

where P is the probability for the atom to absorb the photon and τ the

lifetime of the transition.

As an example, let us take an atom of ^{88}Sr interacting with a photon in resonance with the $^1S_0 \rightarrow {}^1P_1$ transition. The mass of the atom is ~ 87.9 atomic mass units and the transition requires a photon with a wavelength of 461 nm. Using eq. 2.5 we obtain a recoil velocity of 1.5 mm/s. Even if it seems a small quantity, after around 5 ns the photon is re-emitted and the atom is ready to absorb another photon. This means that under ideal conditions a deceleration of up to 285 km/s^2 can be obtained.

In more detail, we can consider a two-level atom ($|g\rangle$ and $|e\rangle$) separated by an energy $E_e - E_g = h\nu_0$, which interacts with a monochromatic plane wave of intensity I and frequency ν_L. The number of absorption and spontaneous re-emission cycles, in photons per second, is given by the rate of spontaneous emissions $1/\tau$ multiplied by the probability of occupation of the excited state:

$$P = \frac{1}{2}\frac{S}{1 + S + \Delta_f^2/\Gamma^2}, \tag{2.7}$$

$$\text{with} \quad S = \frac{I}{I_0} \quad \text{and} \quad \Delta_f = \gamma - \vec{k}\cdot\vec{v}.$$

Where $\gamma = \nu_L - \nu_0$ is the difference between the frequency of the laser and that of the transition, and $\Gamma = 1/(2\pi\tau)$ is its natural width (in Hz), I is the intensity of the laser, I_0 the saturation intensity[1], and the quantity $\vec{k}\cdot\vec{v}$ is the shift in frequency as perceived by the atom due to the Doppler effect [62].

2.2.1. Zeeman slower

To obtain a sufficient flux of atoms, it is required to heat the strontium to several hundred degrees which translates to an atomic velocity of hundreds of metres per second. As shown in eq. 2.7, the probability for the laser to interact with the atom depends on the velocity of the atom. Hence, only a specific range of speeds can efficiently be slowed down using a pure monochromatic beam.

To overcome this problem it is possible to: ramp the frequency of the laser as the atom slows down (chirping [63]), increase the width of the laser frequency (power or frequency broadening) or use a magnetic field gradient to change the frequency of the transition along the flight of the atoms (Zeeman slower). Each of these techniques has its benefits, but the last one, in particular, is the one that produces a constant flux of cold atoms and has low power requirements.

[1] The saturation intensity is the intensity for which the probability of excite an atom using resonance light, is 25% and is calculated as $I_0 = \frac{2\pi^2\hbar c\Gamma}{3\lambda^3}$

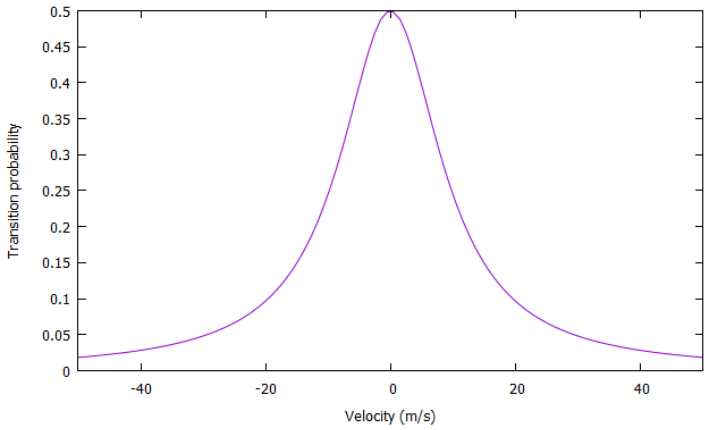

Figure 2.3: Transition probability distribution as a function of the velocity of the atom using the ${}^1S_0 \rightarrow {}^1P_1$ transition of strontium.

For these reasons, the Zeeman slower has been implemented as a pre-cooling stage in this experiment; this will be the subject of the discussion in this section.

In presence of magnetic fields the Δ_f of eq.2.7 becomes:

$$\Delta_f = \gamma - \vec{k} \cdot \vec{v} - \mu B(z)/\hbar. \tag{2.8}$$

Here $\mu = (g_e m_e - g_g m_g)\mu_B$ is the transition magnetic moment, $g_{e,g}$ is Landé g-factor for the exited and ground state, z is position along the Zeeman slower and $m_{e,g}$ is the magnetic quantum number [64].

The maximal deceleration ($a_{max} = F_{max}/m_{atom}$) occurs at $\Delta_f = 0$ i.e. on resonance. This means we need to vary the magnetic field in parallel with the velocity of the atom to keep the light in resonant with the transition:

$$\Delta_f = 0 \Rightarrow \gamma - \vec{k} \cdot \vec{v}(z) = \frac{\mu B(z)}{\hbar} \Rightarrow B(z) = \frac{\hbar}{\mu}\left(\gamma - \vec{k} \cdot \vec{v}(z)\right). \tag{2.9}$$

Assuming constant deceleration we obtain:

$$B(z) = \frac{\hbar}{\mu}\left(\gamma - |k| \cdot \sqrt{\frac{2|a|z}{m}}\right). \tag{2.10}$$

Combining eq. 2.10 and eq. 2.6 with $\Delta_f = 0 \leftarrow P = 1/2$ we obtain:

$$B(z) = B_0 - \frac{1}{\mu m}\sqrt{\frac{\hbar^3 |k|^3}{2\tau}\frac{S}{1+S}}, \tag{2.11}$$

where $B_0 = \frac{\hbar}{\mu}\gamma$ is the offset of the magnetic field. This offset is essential to ensure that the laser used in the Zeeman slower does not interact with the atoms after they exit the slower. Otherwise, the continued interaction will cause the atoms to come to rest and then continue accelerating in the opposite direction without having the chance to be captured.

This magnetic profile can be achieved by using a carefully designed coil, with the number of turns of wire changing along the Zeeman slower axis [65] or by using permanent magnets with variable positions and/or strengths [64, 66]. Due to the lower cost and simplicity of use, we opted for the second type and realised a design proposed by V. Lebedev and D. M. Weld [67] (see chapter 4.2.1).

Equation 2.11 represents an ideal case. If a gradient higher than the one calculated in eq. 2.11 is present, the atoms will not have the time to slow down enough to remain in resonance with the light. It is also necessary to consider imperfections in the coil (or magnets) used to create the magnetic field and fluctuations in the power of the Zeeman slower beam. For these reasons the Zeeman slower uses in the experiment has lower gradient than the one calculated in equation 2.11.

It is also worth noting that an atom will interact with the light only when it is in a region where $\vec{k} \cdot \vec{v} + \mu B z/\hbar \approx \gamma$. This means that faster atoms will start to interact earlier than the slower ones, obtaining a compression in the velocity distribution in addition to a reduction of the average speed.

2.3. Magneto Optical Trap (MOT)

With a single laser beam, the velocity of an atom will decrease until it stops and eventually will start to be pushed back. Instead of using a single beam, a pair of counter-propagating beams with a frequency that is red detuned from the transition could be used. In this case the Doppler effect will ensure higher probability for the atom to interact with the beam propagating in the opposite direction, hence opposing the motion of the atom.

Figure. 2.4 shows an atom moving to the right and interacting with a co- and counter-propagating beam. The beam moving against the motion of the atom will appear to have a higher frequency in the reference frame of the atom and the beam with the same direction a lower frequency. When the beam is red detuned from resonance, the counter propagating beam is Doppler shifted closer to resonance and has a higher probability of interacting with the atom.

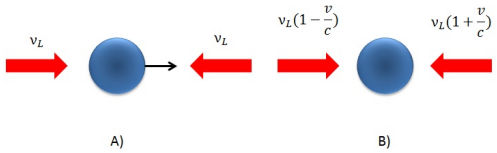

Figure 2.4: Schematic representation of the Doppler cooling. A) in the system of reference of the lab, B) in the system of reference of the atom.

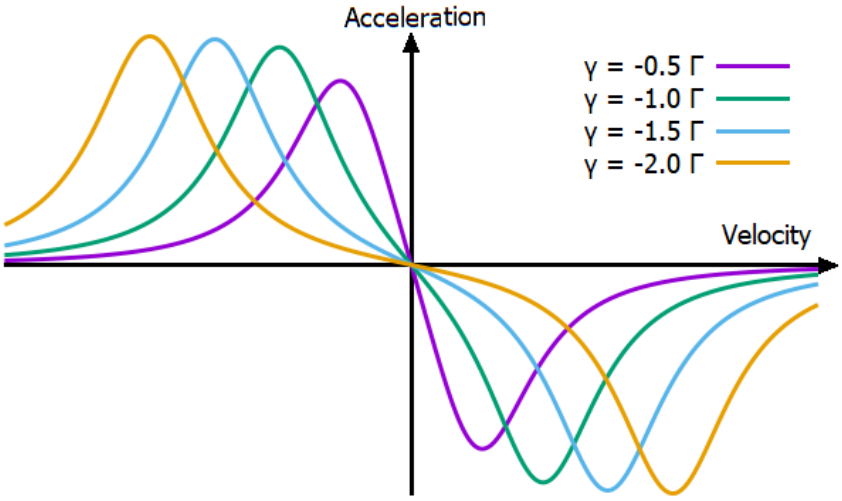

Figure 2.5: Acceleration perceived by an atom in the presence of counter-propagating beams for different detuning Γ, as calculated in the one dimensional case using eq.2.12.

So far we have discussed only how to slow the atoms, but not how to trap them. Again considering the ${}^1S_0 \rightarrow {}^1P_1$ transition, if a linear magnetic field $B_z = B_0 z$ is applied, then due to the Zeeman effect the ${}^1P_1$ state will be split into sub-levels as shown in fig. 2.6.

Applying now two counter-propagating beams with opposite circular polarisation and red detuning, the beam coming from the positive z-direction will interact predominantly with atoms that are located at $z > 0$ and vice versa, thus obtaining atomic confinement along one axis.

In general, eq 2.6 can be rewritten as [68, 69]:

$$\vec{F}_j = \alpha\beta_j\hat{k}_j \sum_{n=-1,0,1} \eta_n / \left(1 + \beta_{tot} + 4\left(\gamma - k_\Gamma \hat{k}_j \cdot \vec{v} - \mu_\Gamma n \left|\vec{B}\right|\right)^2\right), \quad (2.12)$$

where $\alpha = h\pi\Gamma/\lambda$, $\beta_j = I_j/I_s$ is the intensity of the beam j respective to the saturation intensity, $\beta_{tot} = \sum_j \beta_j$ and

$$\eta_0 = (1 - \varsigma^2)/2 \qquad \eta_{\pm 1} = (1 \mp s\varsigma)^2/4 \quad (2.13)$$

where $\varsigma = \hat{k}_j \cdot \hat{B}$ and $s = \pm 1$ is the handedness of the polarisation, resulting in the equation of motion of a damped harmonic oscillator:

$$\ddot{z} - \gamma\dot{z} + \omega_{trap}^2 z = 0. \quad (2.14)$$

The magnetic field can be generated by two coils in anti-Helmholtz configuration:

$$B_r = \frac{\mu I}{2\pi r} \frac{z - A}{[(R-r)^2 + (z-A)^2]^{1/2}} \left[-K(k^2) + \frac{R^2 + r^2 + (z-A)^2}{(R-r)^2 + (z-A)^2} E(k^2)\right] \quad (2.15)$$

$$B_z = \frac{\mu I}{2\pi r} \frac{z - A}{[(R-r)^2 + (z-A)^2]^{1/2}} \left[K(k^2) + \frac{R^2 - r^2 - (z-A)^2}{(R-r)^2 + (z-A)^2} E(k^2)\right] \quad (2.16)$$

$$k^2 = \frac{ARr}{(R-r)^2 + (z-A)^2} \quad (2.17)$$

where R is the coil radius, A the location of its centre on the z-axis, r and z the radial and axial coordinates, and K and E are the incomplete elliptic integrals of the first and second kind [70].

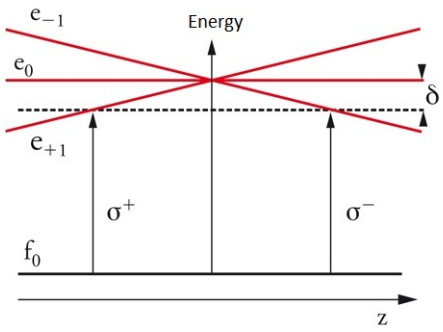

Figure 2.6: Splitting of the atomic levels caused by the Zeeman effect in a 1D Magnetic Optical Trap, the split in energy $\delta = \mu B(z)/\hbar$ is produced by the magnetic field.

2.3.1. Doppler limit

For small velocity and $\vec{B} = 0$, eq. 2.12 can be rewritten as:

$$\left(\frac{d\langle E\rangle}{dt}\right)_{cooling} = Fv \approx \hbar k \frac{8\gamma}{\Gamma}\left[\frac{I/I_0}{[1+(2\gamma/\Gamma)^2]^2}\right] v. \tag{2.18}$$

Each time an atom emits a photon, it will acquire a recoil velocity v_r. The resulting motion is analogous to the motion of a tiny particle on the surface of a fluid (Brownian motion). To find the rate of energy increase, we consider a two level atom where with each emitted photon is associated with a quantity of motion equal to $\hbar k$ with opposite direction to the photon emitted. After time t has passed, the average quadratic pulse that transferred to the atom will be:

$$< p^2 >= \frac{t}{\tau} p_e (\hbar k)^2. \tag{2.19}$$

For small velocity:

$$\left(\frac{d < E >}{dt}\right)_{heating} = \frac{1}{2m}\frac{d < p^2 >}{dt} = \frac{1}{2m}(\hbar k)^2 \frac{1}{2\tau}\frac{I/I_0}{1 + I/I_0 + (2\gamma/\Gamma)^2}. \tag{2.20}$$

The equilibrium will be obtained when:

$$\left(\frac{d < E >}{dt}\right)_{heating} = \left(\frac{d < E >}{dt}\right)_{cooling} = 0. \tag{2.21}$$

Assuming Maxwell-Boltzmann distribution of the velocity, eq.2.21 can be rewritten as [62]:

$$k_b T = \frac{\hbar\Gamma}{4}\left(\frac{\Gamma}{2\mid\gamma\mid} + \frac{2\mid\gamma\mid}{\Gamma}\right) \tag{2.22}$$

The minimum temperature is achieved for $\gamma = \Gamma/2$. In the case of Sr, using 461 nm laser for cooling, a temperature of 110 μK can be reached.

2.3.2. Repumps

The $^1S_0 \rightarrow ^1P_1$ cooling cycle is not completely closed, from the $^1P_1$ state an atom can also decay into the $^1D_2$ with a probability of 1 in ≈12000 [71]. From there they then decay into the $^3P_1$ and $^3P_2$ state with a probability of 2/3 and 1/3 respectively. The $^3P_1$ states decay into the $^1S_0$ with a lifetime of 21 μs where the atom can re-enter the cooling cycle. In contrast, the $^3P_2$ state decays with a lifetime ≈ 120 s, meaning that atoms in this state are lost from the MOT. To keep the atoms in the cooling cycle, we need to repump the atoms back to the ground state.

One possibility to repump the atoms back to the ground state is using a 3 μm laser pointed at the MOT. A laser with this wavelength can excite the atoms from the $^3P_2$ state into the $5s4d\ ^3D_2$, from here they can then decay into the $5s5p\ ^3P_{2,1}$ states, with the majority of the atoms decaying into the $^3P_1$ state. The difficulty of using this transition emerges from the wavelength of the laser. Until recently laser diodes with this wavelength were not commercially available and the light was obtained via optical parametric oscillators [72].

The second solution, most frequently used in atomic clocks, is via the $5s5p\ ^3P_2$ state using a 707 nm laser. From this state the atom will decay into all three ^3P_j states. In particular, with a probability of 1/4 the atoms will decay into the $^3P_0$ state. This state has a lifetime of several minutes, so an additional 679 nm laser is required to pump back the atoms into the $5s5p\ ^3P_2$ state closing the cycle.

The 679 nm laser can be substituted with the 2.6 μm laser. This wavelength is in resonance with the $^3P_0 \rightarrow 5s4d\ ^3D_1$ transition, from here the atoms decay into the ^3P_j manifold with probability 2%, 39% and 59% for j=2, 1 and 0 respectively. We are using this scheme because the $5s4d\ ^3D_1$ is the same transition required to generate the long-range interaction and the results are 35% better than those obtained by the 679 nm laser (see fig.5.7 in chapter 5.3.3).

2.4. Red MOT

As shown before, the minimum temperature that is possible to achieve using the ${}^1S_0 \rightarrow {}^1P_1$ transition is in the order of hundreds of μK. If a lower temperature is required, a second stage of cooling is needed.

The ${}^1S_0 \rightarrow {}^3P_1$ transition is available for strontium at 689 nm, this transition has a linewidth $\Gamma = 7.5kHz$ and saturation intensity of $3\,\mu\mathrm{W/cm^2}$. Using this transition, it is possible to reach a temperature of 460 nK, limited by the recoil energy[2] of photons at this wavelength [73]. This transition is so narrow that even starting from the final stage of the blue MOT, the 689 nm laser will interact with less than 2% of the atoms due to the Doppler effect. For this reason the laser needs initially to be broadened to capture the maximum number of atoms and then gradually decrease the broadening until the minimum temperature is reached. This is done by increasing the power of the laser over saturation and modulating its frequency. The initial phase is called broadband red MOT and the second phase single frequency red MOT. An exhaustive explanation of the physics involved in this cooling stage can be found in [73–75]. Below are reported only few key points about this cooling mechanism.

- The maximum acceleration imposed to the atoms by the 689 nm laser is comparable to the gravitational acceleration ($a_{max}/g = 16$), and therefore it is non-negligible.
- The need to interact with a class of velocity higher than the natural linewidth would allow, requiring frequency and/or power broadening of the laser.
- The minimum temperature calculated by eq. 2.22 is lower than the recoil temperature that is equal to 490 nK which is towards the lower limit of temperatures achievable using this cooling transition [76].

2.5. 1D lattice trap

2.5.1. Dipole potential

In contrast with the MOT, in an optical lattice, the confinement is not produced by optical pressure, but by the interaction between the electric field of a laser and the induced electric dipole of the atoms. By using a far-detuned laser, the

[2]The recoil temperature is $T = \frac{\hbar^2 k^2}{3mk_b}$.

resulting trap potential is much weaker compared to the one produced by a MOT, but the optical excitation can be kept low. Under the right conditions, it is possible to create a conservative potential that is insensitive to the internal state of the atoms, making the far detuned optical lattice an ideal tool to study the internal state of an atom.

Starting by considering an atom as a classical oscillator [77], an atom placed in an oscillating electric field $E(r,t) = \widehat{e}E_0 e^{-i\omega t} + c.c.$[3] (as in a laser beam) will experience an induced dipole moment $p(r,t) = \widehat{e}P_0 e^{-i\omega t} + c.c.$. The relation between electric field and polarizability is:

$$P_0 = \alpha E_0, \tag{2.23}$$

where α is the complex polarizability, which depends on the frequency of the electric field (ω). This induced polarizability will create an interaction between the electric field and the atom:

$$U_{dip} = -\frac{1}{2}\langle pE\rangle = -\frac{1}{2}\mathrm{Re}(\alpha)\langle E^2\rangle = -\frac{1}{2\epsilon_0 c}\mathrm{Re}(\alpha)I, \tag{2.24}$$

where $\langle\ \rangle$ is the average over time and $I = 2\epsilon_0 c|E_0^2|$ is the intensity of the electric field. The resulting dipole force is:

$$F_{dip}(r) = -\nabla U_{dip}(r) = -\frac{1}{2\epsilon_0 c}\mathrm{Re}(\alpha)\nabla I(r). \tag{2.25}$$

The absorbed power is:

$$P_{abs} = \langle \dot{p}E\rangle = \frac{\omega}{\epsilon_0 c}\mathrm{Im}(\alpha)I, \tag{2.26}$$

that translates to a scattering rate:

$$\Gamma_{abs}(r) = \frac{P_{abs}}{\hbar\omega} = \frac{1}{\hbar\epsilon_0 c}\mathrm{Im}(\alpha)I(r). \tag{2.27}$$

Using the Lorentz's model of a classical oscillator [78], we have:

$$\alpha = 6\pi\epsilon_0 c^3 \frac{\gamma/\omega_0^2}{\omega_0^2 - \omega^2 - i(\omega^3/\omega_0^2)\Gamma}, \tag{2.28}$$

where ω_0 is the frequency of the transition, Γ its spontaneous decay rate and

[3] $\widehat{e}$ is the direction where the electric field propagate, E_0 its amplitude, ω its frequency and c.c. is its complex conjugate

ω the frequency of the electric field.

Now we can replace α in eq. 2.26 and 2.24, obtaining:

$$U_{dip}(r) = \frac{3\pi c^2}{2\omega_0^3}\frac{\Gamma}{\Delta}I(r), \tag{2.29}$$

$$P_{abs}(r) = \frac{3\pi c^2}{2\hbar\omega_0^3}\left(\frac{\Gamma}{\Delta}\right)^2 I(r), \tag{2.30}$$

where $\Delta = \omega - \omega_0$.

These two equations give us two significant results:

- For red-detuned light ($a > 0$) the potential is attractive, and the atom will sit in the maximum of the intensity, for blue-detuned light ($a < 0$) the potential is repulsive, and the atoms will sit in the intensity minimum.
- The dipole potential scales as I/Δ and the scattering rate as I/Δ^2, therefore to avoid heating the atomic sample it is possible to use a far-detuned laser with high intensity.

2.5.2. Multi-level atoms

So far we have modelled atoms as having a single electron elastically bound to the nucleus. In reality, the dipole potential depends on the state of the atom. In general, the polarizability of the state a at the frequency ω_0 is given by the sum of the polarizability over all levels k:

$$\alpha_a = \frac{2}{\hbar}\sum_k |d_{ak}|^2 \frac{\omega_{ak}}{\omega_{ak}^2 - \omega_0}, \tag{2.31}$$

where ω_{ak} is the frequency of the transition between the state a and the state k and where d_{ak} is the dipole matrix element of the same transition:

$$|d_{ak}|^2 = \frac{6\pi\epsilon_0\hbar c^3}{2\omega_{ak}^3}\Gamma_{ak}. \tag{2.32}$$

Unfortunately, a direct measurement of the transition rate is often challenging and in the literature it is easier to find the total decay rate equivalent to the state lifetime $\tau_a = 1/\Gamma_a$. Therefore, it is more useful to rewrite eq. 2.31 as [78]:

$$\alpha_a(\omega) = 6\pi\epsilon_0 c^3 \frac{\omega_{ak}}{\omega_{cm}^3(\omega_{ak}^2 - \omega_0)} b_{ak} b_{M_{ak}} \Gamma_a, \tag{2.33}$$

where b_{ak} is the branching ratio for the transition rates between fine structure states, $b_{M_{ak}}$ is the normalised magnetic branching ratio and $\omega_{cm}^3 = \sum_n b_n \omega_n^3$ is the centre-of-mass frequency. For linearly polarised light $b_{M_{ak}} = 1$ and hence can be ignored.

2.5.3. Calculation of the polarizability

During the measurement of the long-range interaction we are interested in three states in particular: $^1S_0$, $^3P_1$ and the $^3D_1$. For these states, we need to know how much the attractive force generated by the lattice laser is, and the frequency shift generated by the light. To do that, it is important to know the polarizability of those states. Using eq. 2.33 along with the data in tab. 2.3 it is possible to calculate the expected polarizability for those states, and the results are shown in fig. 2.7.

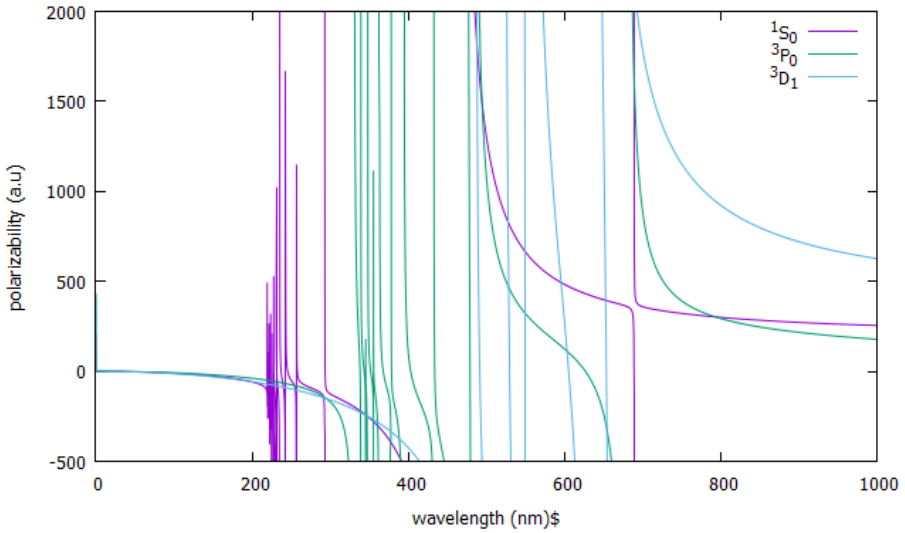

Figure 2.7: Polarizability of $^1S_0$, $^3P_0$ and $^3D_1$ states as calculated using eq. 2.33 and the data from tab. 2.3.

Lower level	Upper level	Wavelength (nm)	ω $(10^{-15}\,s^{-1})$	Γ $(10^{-5}\,s^{-1})$	b	ω_{cm} $(10^{-15}\,s^{-1})$
$5s^2\ {}^1S_0$	$5s20p^1P_1$	219.3977	8.59	2.560	1	8.59
	$5s19p^1P_1$	219.6214	8.58	3.200		8.58
	$5s18p^1P_1$	219.8892	8.57	4.200		8.57
	$5s17p^1P_1$	220.2176	8.55	5.000		8.55
	$5s16p^1P_1$	220.6239	8.54	6.400		8.54
	$5s15p^1P_1$	221.131	8.52	8.500		8.52
	$5s14p^1P_1$	221.7816	8.49	11.700		8.49
	$5s13p^1P_1$	222.6304	8.46	15.700		8.46
	$5s12p^1P_1$	223.7655	8.42	24.000		8.42
	$5s11p^1P_1$	225.3256	8.36	37.000		8.36
	$5s10p^1P_1$	227.5304	8.28	66.000		8.28
	$5s9p^1P_1$	230.7264	8.16	115.000		8.16
	$5s8p^1P_1$	235.4319	8.00	180.000		8.00
	$4d5p^1P_1$	242.8095	7.76	170.000		7.76
	$5s7p^1P_1$	256.9469	7.33	53.000		7.33
	$5s6p^1P_1$	293.183	6.42	19.000		6.42
	$5s5p^1P_1$	460.7331	4.09	2010.000		4.09
	$5s5p^3P_1$	689.2585	2.73	0.469		2.73
$5s5p^3P_0$	$5s6s^3S_1$	679.289	2.773	74.58	1/9	2.701
	$5s7s^3S_1$	432.766	4.353	21.6		4.28
	$5s8s^3S_1$	378.16	4.981	8.22		4.909
	$5s9s^3S_1$	355.446	5.299	4.53		5.227
	$5s10s^3S_1$	343.525	5.453	2.77		5.411
	$5s4d^3D_1$	2603.13	0.7236	0.381	5/9	0.666
	$5s5d^3D_1$	483.339	3.897	61		3.88
	$5s6d^3D_1$	394.192	4.779	26.7		4.761
	$5s7d^3D_1$	363.018	5.189	14.2		5.171
	$5s8d^3D_1$	348.099	5.411	8.51		5.394
	$5s9d^3D_1$	339.326	5.551	5.51		5.534
	$5p^2\ {}^3P_1$	474.325	3.971	120	1/3	3.917
	$4d^2\ {}^3P_1$	330.753	5.703	59	1	5.703
$5s4d^3D_1$	$4d5p^3P_2$	521.2978	3.61	19.00	1	3.61
	$4d5p^3P_1$	522.2198	3.61	340.00		3.61
	$4d5p^3D_2$	548.6136	3.43	153.00		3.43
	$4d5p^3D_1$	552.1765	3.41	630.00		3.41
	$4d5p^1D_2$	638.0728	2.95	52.00		2.95
	$4d5p^3F_2$	661.7266	2.85	160.00		2.85
	$5s4f^3F_2$	485.5045	3.88	263.00		3.88
	$5s6p^1P_1$	627.2042	3.00	0.14		3.00
	$5s6p^3P_1$	636.391	2.96	37.00		2.96
	$5s6p^3P_0$	636.9918	2.96	180.00		2.96

Table 2.3: Parameters for calculation of the polarizability. The data for the ${}^1S_0$ and ${}^3D_1$ states comes from the [79] the data for the ${}^3P_1$ state from [78].

2.5.4. Confinement using light

Equation 2.25 shows how the dipole force is connected to the gradient of the intensity of the beam. Considering a Gaussian beam:

$$I(r,z) = I_0 \left(\frac{w_0}{w(z)}\right)^2 \exp\left\{\frac{-2r^2}{w_0^2}\right\}, \tag{2.34}$$

where w_0 is the waist radius, I_0 is the peak intensity and

$$w(z) = w_0\sqrt{1+\left(\frac{z}{z_r}\right)^2}; \qquad z_r = \frac{\pi w_0^2}{\lambda}. \tag{2.35}$$

It is easy to see that the confinement along the direction of propagation of the beam is much smaller than the one along the perpendicular to it (see fig. 2.8). This result in a very low density, incompatible with the measurement of the long-range interaction. This problem can be solved by retro-reflecting the beam, generating a standing wave with a much higher gradient of the intensity along the direction of the propagation. The resulting potential is:

$$U = U_0 \left(\frac{w_0}{w(z)}\right)^2 e^{-2(r/w(z))^2} \cos^2(kz), \tag{2.36}$$

where

$$U_0 = -\alpha \frac{4P}{\epsilon_0 c \pi w_0^2}, \tag{2.37}$$

with P being the total optical power.

2.5.5. Inhomogeneous AC Stark broadening

When an atom sits in a region where an oscillating electric field is present, it will experience a shift of its levels due to the polarizability induced by the electric field itself (AC Stark effect). In particular, if we consider a transition from level $|a\rangle$ to the level $|b\rangle$, the transition will be shifted by the electric field by an amount equal to:

$$\delta\omega = -\frac{1}{2\hbar}\left(\alpha_a - \alpha_b\right)\langle E^2\rangle = -\frac{1}{4\hbar}\Delta\alpha E_0^2 = -\frac{1}{\epsilon_0 c}\Delta\alpha I. \tag{2.38}$$

To calculate the broadening produced by the optical trap, we need to find the distribution of the atoms and start by considering the unidimensional case, however the result is the same in higher dimensions. For $k_b T \ll U_{dip}$ we can

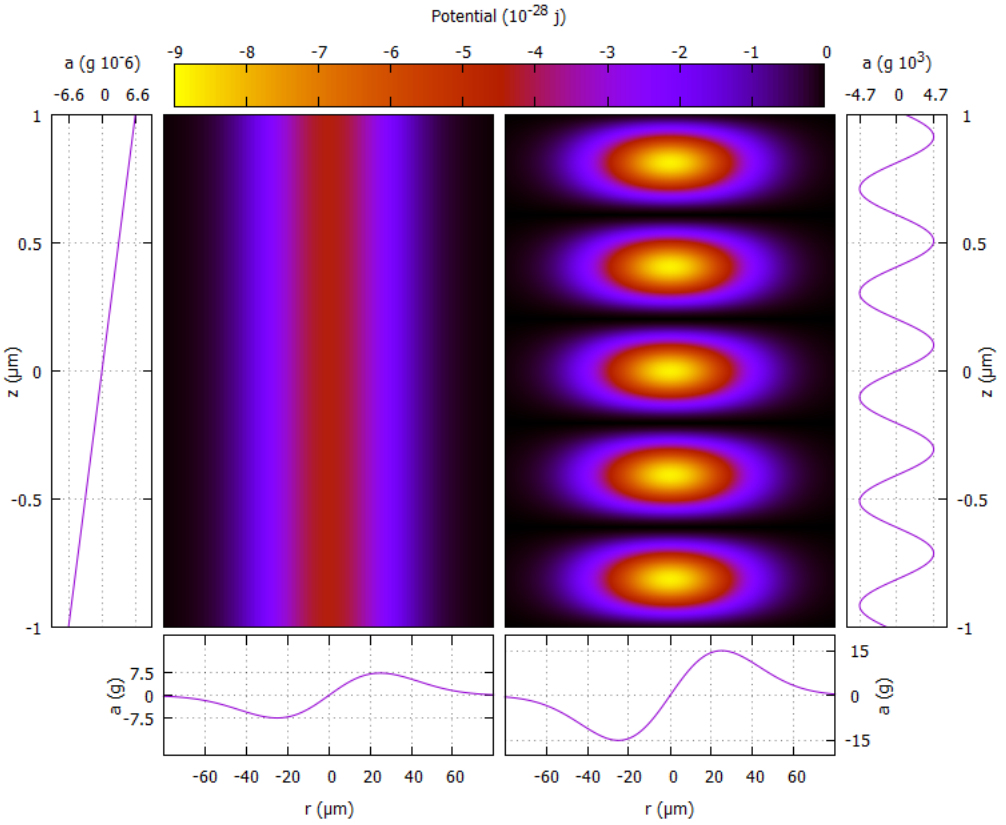

Figure 2.8: Potential generated by 500 mW of 813 nm laser focused at a waist of 50 μm in a region of 80 x 1 μm around the focus point and relative induced acceleration (left). Potential and relative acceleration generated by the same laser but with a counter-propagating beam, resulting in a standing wave (right).

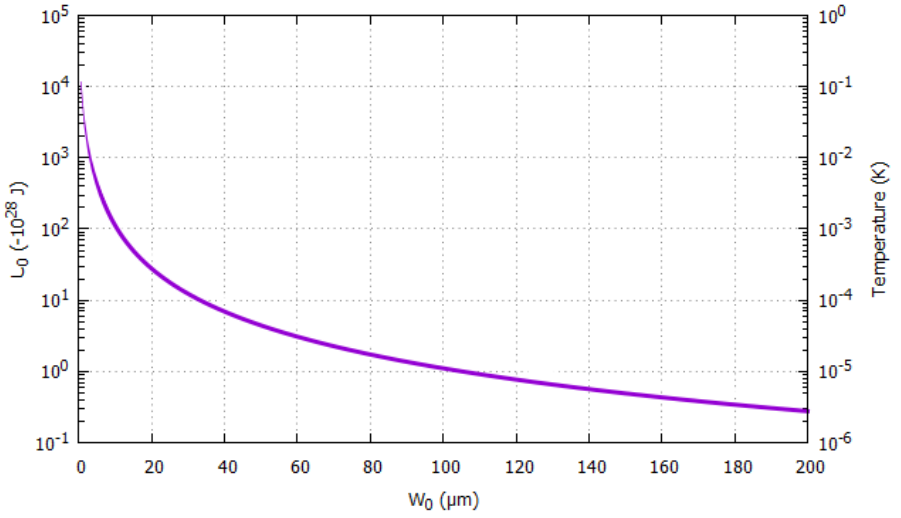

Figure 2.9: Trap depth and relative confinement temperature in $r = 0$, $z = 0$ versus lattice waist for 1 W of optical power.

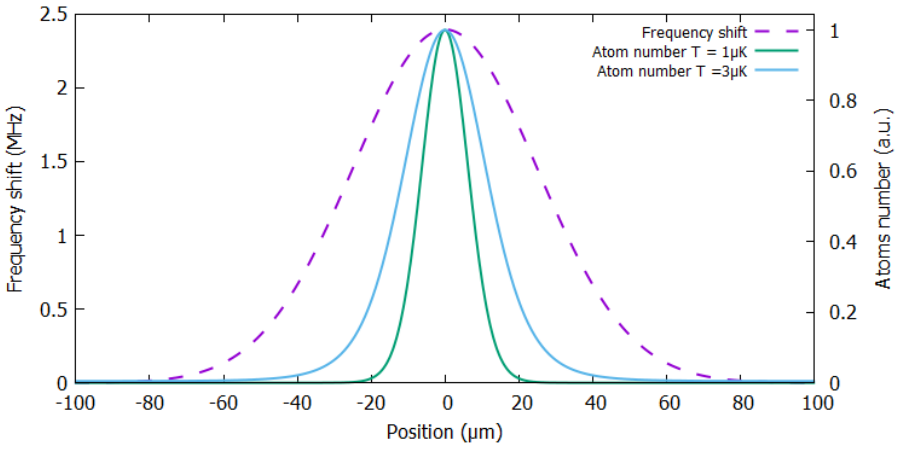

Figure 2.10: Frequency shift produced by an 813 nm lattice with P= 500 mW and $w_0 = 50\,\mu$m (dashed line). Atomic distribution inside the same lattice at different temperature (solid line).

consider the atoms effectively in an infinitely deep trap. In this case, the density distribution of the atoms will be [80]:

$$n(r) = n_0 e^{-\frac{U(r)}{k_b T}}, \tag{2.39}$$

where n_0 is the atoms density at the minimum of the trap and $U(r)$ is given by eq. 2.36. The resulting spectroscopy figure in parametric form is:

$$\omega = \frac{1}{4\hbar}\Delta\alpha I(r), \tag{2.40}$$

$$n = n_0 \exp\left(-\frac{\frac{1}{2}\alpha_a I(r)}{k_b T}\right). \tag{2.41}$$

The result of this equation is shown in fig. 2.11. To avoid this broadening, it is

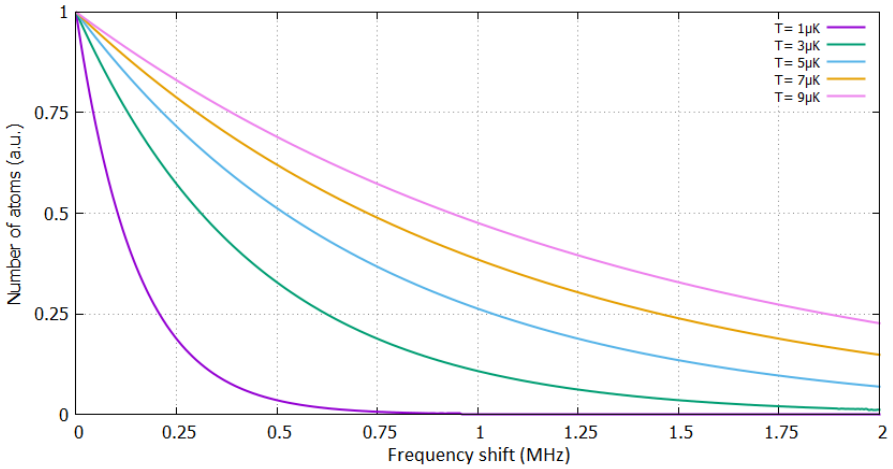

Figure 2.11: Power-broadening generated by the inhomogeneity of the lattice trap.

possible to either decrease the difference between the polarisability of the two states [81], to decrease the temperature of the sample or to use an additional laser that is spatially mode matched with the trapping field and with frequency that is tuned in between the two hyperfine levels [82].

2.6. Excite atoms in the $^3D_1$ state

To study the LRI it is important to control the number of atoms in the excited state. This controlled excitation can be done by sending a short pulse of resonant light to the atoms. The probability for an atom to be excited by a pulse of length t with frequency ω is [69]:

$$P(t) = \frac{\Omega}{W} \sin \frac{Wt}{2}, \tag{2.42}$$

Where $\Omega = \vec{p} \cdot \vec{E_0}/\hbar$ is the Rabi frequency, and

$$W^2 = \Omega^2 + (\omega - \omega_0)^2, \tag{2.43}$$

with ω_0 the frequency of the transition, $\vec{p}$ the transition dipole moment and $\vec{E_0}$ the electric field. Sending a pulse in resonance with length $\Omega t = \pi$ the probability of transitions is 100%, for obvious reasons this type of pulse is called π-pulse.

2.7. Normalised detection

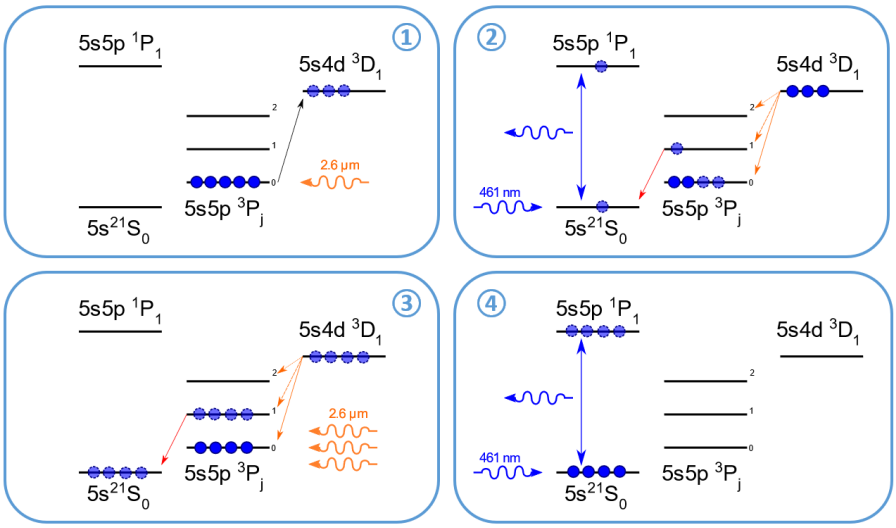

Figure 2.12: Schematic of the sequence used for the detection of the transfer efficiency.

The number of atoms captured in the MOT will vary between each mea-

surement sequence, therefore it is important to measure the total number of atoms present in the $^3P_0$ state before and after the pulse in order to normalise the detection signal. Starting with the atoms in the $^3P_0$ state, the detection can be split into 4 phases:

1. A 2.6 µm pulse is sent to the atoms.

2. After 5 ms, 39% of the exited atoms will decay into the $^3P_1$ state, 59% will go back to the $^3P_0$ state and 2% will decay into the $^3P_2$ state and are lost. Atoms from the $^3P_1$ state will then go in the ground state where they can be detected using 461 nm light (N_1).

3. The 2.6 µm laser is turned on again, but this time it stays on for several ms to ensure that the majority[4] of the atoms are pumped into the ground state ($^3P_0 \to {}^3D_1 \to {}^3P_1 \to {}^1S_0$).

4. The atoms in the ground state are counted again using the 461 nm light (N_2).

The transfer efficiency will be:

$$\eta = \frac{\frac{N_1}{0.39}}{\frac{N_2}{0.98} + \left(1 + \frac{0.02}{0.39} N_1\right)}. \tag{2.44}$$

2.8. Chapter summary

This chapter discussed the theory behind the cooling and trapping of Sr atoms, as well the effect of dipolar traps on the transitions levels and how to manipulate and measure the states of an atom.

To complete this experiment we need to cool, trap, probe and detect atoms. Each of those tasks uses one or more lasers, each with a different wavelength and each of them needs to be kept to few MHz or less ($\approx$ 1 kHz for the second stage of cooling) from the required frequency. This requires a complex and robust stabilisation system. In particular, the 2.6 µm laser used to induce the long-range interaction is outside the spectrum of most commonly used lasers (VIS-NIR) and it requires particular care. When possible, I tried to minimise the number of lasers required and use lasers that require less stringent stabilisation or power requirements.

[4] 2% of the atoms will be lost in the $^3P_2$ state

I the next chapter is presented a study of different geometries of magneto-optical trap for strontium atoms to find the most suitable one for this experiment.

CHAPTER 3

Study of different geometries for Magneto Optical Traps

In this chapter are presented and compared three different schemes to realise the cooling of strontium atoms. This study has been performed to asses which of those geometries will capture the largest sample of atoms when given a limited amount of power. As will be explained in more detail in ch. 5.3.2, the number of atoms captured in a MOT depends of the rate at which the atoms are captured (R) and of the rate at which they escape the MOT (β). β depends mostly of the pressure inside the chamber and it is independent from the geometry of the MOT. R depends of the flux of atoms reaching the MOT and of the fraction of atoms that can be captured. An atom will be captured if its direction and speed are inside a certain parameter range that depends on the geometry of the MOT. This study has been performed with the goal to find which geometry results in the broadest parameter. Those geometries have already been studied previously when they were used for trapping other atoms (especially rubidium), however this is the first time that those geometries are been studied in this manner for trapping strontium.

- **Six-beam MOT** is the most common scheme used in cold atoms. It consists of three pairs of mutually orthogonal counter-propagating beams (see fig. 3.1). Of the ones considered, this scheme is the most flexible and easy to realise, but it requires careful alignment and is subject to loss of alignment over time.

- **Pyramidal MOT** is conceptually similar to the previous scheme. In a pyramidal MOT, the confinement is achieved by the use of six beams, but only one beam enters the chamber. The cooling in the non input beam axis is provided by the reflections of the beam by mirrors in vacuum (see fig. 3.6). This scheme was used for production of a rubidium MOT for the first time in 1996 [83]. The scalability of this scheme has allowed integrating a MOT into an atom chip [84]. In caparison to the six-beam MOT the pyramidal design is more compact and robust to misalignment; however, the disadvantages are a more difficult construction, an increase of scattering light due to reflection against the edge of the mirror inside the vacuum chamber, and a decrease of optical access.

- **Tetrahedral MOT** has four beams. Each beam can be seen as generated from a corner of a tetrahedron and directed at the centre of it (see fig 3.11). Similarly to the pyramidal MOT, only one beam enters the chamber, the other three are generated by the reflection of the mirrors. The mirrors need to have an angle of $\approx 35^\circ$ to balance the intensity of the main beam. This scheme was demonstrated by Vangeleyn et al. [85] using rubidium. It is also suitable for the production of a chip-based MOT [86]. The advantages of the tetrahedral MOT compared to the pyramidal MOT is the fact that confinement of the atoms is located above the mirrors, giving more optical access.

To help to decide which scheme is the most favourable for the experiment, I wrote a C++ program to simulate the trajectories of the atoms in the MOT (see appendix A), and to use this information to calculate the number of atoms captured with each design.

For each of these schemes we calculate the direction of the forces produced by the light and the trajectory for the atoms when entering the MOT. Then the best direction the atoms should enter the MOT from is found. The analysis concludes with finding the relation between power and detuning for the cooling beams.

3.1. Six-beam MOT

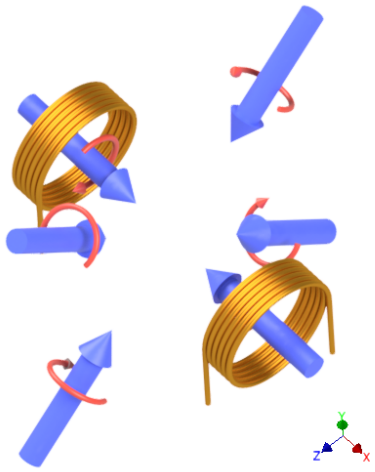

Figure 3.1: Schematic representation of a six-beam MOT. The big arrows represent the direction of the beams with their polarisation. The coils in anti-Helmholtz configuration provide the magnetic field necessary for the confinement.

This is the standard scheme used in cold atoms experiments. Each beam is balanced by another one in the opposite direction; the counter-propagating beams can be generated by retro-reflection or be independent. Each beam is required to be polarised in the right direction using $\frac{\lambda}{4}$ waveplate. This scheme allows for excellent control of the MOT and can be used to accelerate the atoms in a specific direction, as in the case of atomic fountains [87].

The main advantages of a six-beams MOT are:

- it allows the change of the scope of the experiment with little effort;
- it does not require a particular chamber to be used.

On the other hand, compared to the other schemes discussed below, six-beam MOT requires more physical space for optics and more regular re-alignment.

3.1.1. Simulation

Figure 3.2 shows the calculated acceleration of the atoms at rest. This figure has been used to ensure that the direction and polarisation of the beams used

in the simulation were correct. Figure 3.3 shows the trajectory of an atom when it enters the MOT as calculated by the program. In this simulation, as well as in the ones that follow, each beam has a power of 10 mW, a waist radius of 1 cm and a detuning of -21 MHz. The magnetic field in the x-direction is $\approx 40\,\mathrm{G/cm}$. The beams have directions $(\pm 1, 0, 0), (0, \pm 1/\sqrt{2}, \mp 1/\sqrt{2})$ and $(0, \pm 1/\sqrt{2}, \pm 1/\sqrt{2})$. The time resolution used in the simulation is $10\,\mu\mathrm{s}$. From the data it is possible to see that from this particular position the maximum speed that an atom can have and still be captured is 110 m/s. Those initial condition are similar to the ones used in others strontium experiments [78, Chapter 3.5][74, Chapter 6.5].

Figure 3.4 has been generated by simulating atoms moving in the direction of the centre of the MOT, approaching from different angles. For each position a series of atoms is tested. The first atom has a velocity of 10 m/s. If the first atom is captured[1], then the next atom with the same direction is tested, its initial speed is increased by 10 m/s. This is repeated until the atom is too fast to be captured. At this point, the final velocity is recorded. Then the initial position of the atom is changed, and the process is repeated until the whole image is formed.

For each direction, this geometry captures every atom with a speed lower than a certain value that we will call capture velocity. The maximum capture velocity is found to occur when the atoms enter the MOT with a direction that is close to the direction of one of the cooling beams. A possible explanation for this is that atoms that come from those directions will interact with the beams for a longer time.

The next step in the study of this cooling scheme was to find the best mix of power and detuning to reach the highest capture velocity. Although atoms that enter the MOT with a small angle (with respect to one of the cooling beams) have a higher capture velocity, this will require a custom-made vacuum chamber that is not easy to manufacture. A more convenient direction to introduce the atoms in the chamber is from a direction that is between two laser beams. In the next simulation the atomic beam will have starting position (0, 20 mm, 0). The capture velocity for this position as function of power and detuning of the cooling beam is shown in fig. 3.5. From the data it is possible to see that using 10 mW of power per beam[2], it should be possible to capture 98% of the atoms after they exit from Zeeman slower (see ch. 5.2).

[1] In this simulation an atom is considered captured if its distance from the equilibrium

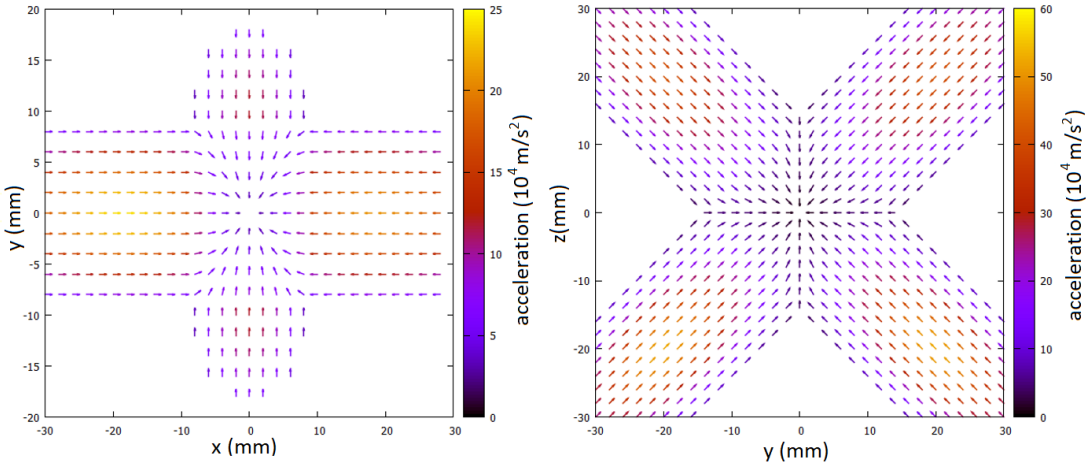

Figure 3.2: Acceleration of the atoms at rest for a six-beam MOT.

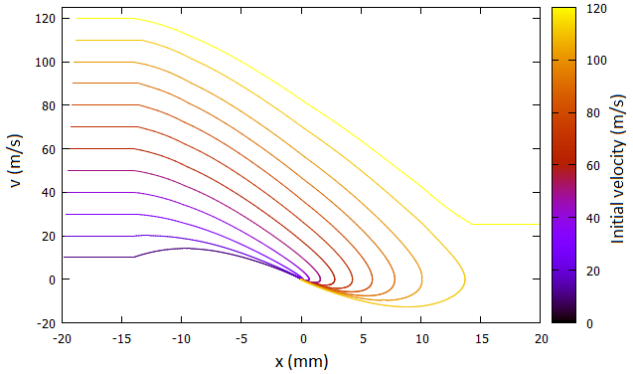

Figure 3.3: Trajectory of the atoms inside the MOT. This figure has been generated by starting the simulation with the atoms in the position $(0, 0, -20\,mm)$, and having starting velocity $(v_0, 0, 0)$. v_0 starts at 10 m/s and it is increased 10 m/s each time.

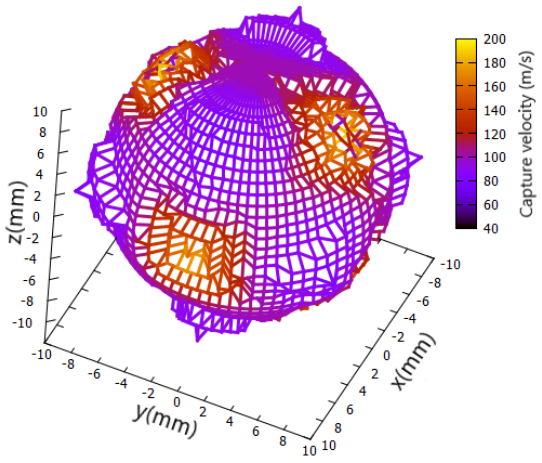

Figure 3.4: Dependency between the capture velocity and the direction of the atoms. The surface on the figure is defined by the region of space where all the beams overlap. This figure has been obtained in a similar way to fig. 3.3, but here the initial position has been varied in a sphere of 20 mm around the centre of the MOT.

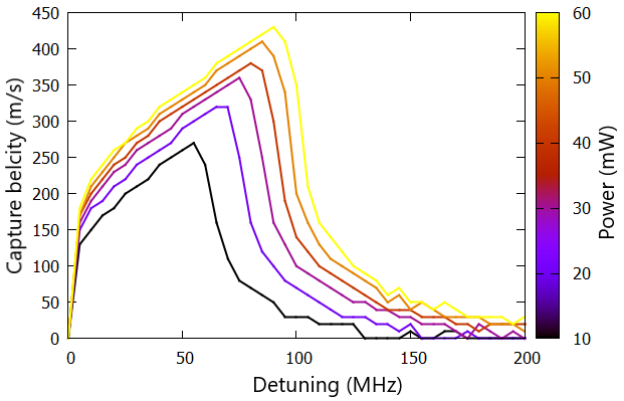

Figure 3.5: Dependency between the capture velocity, the power and detuning of the slowing beam. The simulation starts with atoms having the initial velocity $\vec{V_0} = (0, v, 0)$ where $v > 0$, and the starting point is (0, -20 mm, 0). The power in this graph is referring to a single beam. As expected, the capture velocity increases with the power with diminishing returns as it is approaching saturation.

point is less then 10 μm, and the module of its velocity is less than 1 m/s.

[2]For a total of 30 mW using three retro-reflected beams

3.2. Pyramidal MOT

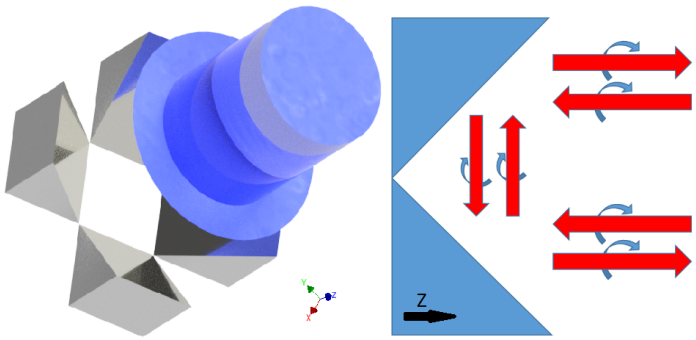

Figure 3.6: CAD model of a pyramidal MOT (left) and a schematic representation of the light path in it (right).

In a pyramidal MOT only one beam enters in the chamber, the cooling in the other directions is provided by the reflections of the beam by mirrors in a vacuum (see fig.3.6).

The advantages of the pyramid MOT are:

- small dimensions
- scalability
- only one beam needs to be aligned.

One of the main disadvantages of this scheme is the difficult access to the MOT and the reduced power efficiency compared to a six-beam MOT.

3.2.1. Simulation

For the pyramidal MOT, the same parameters for power, detuning and magnetic field as for the six-beam MOT are been used. The beams generated by the reflection of the mirrors are square in shape, with 12.5 mm sides. The main beam has direction (0, 0, -1), the reflected beams have directions $(\pm 1, 0, 0)$,$(0, \pm 1, 0)$ and $(0, 0, 1)$.

As for the six-beam MOT, the study of this configuration begins by checking the polarisation and the direction of the beams by calculating the acceleration for the atoms at rest.

In fig.3.8, it is possible to see that although the dimensions of the MOT are similar to the six-beam MOT, when using the same amount of power, the

capture velocity of the pyramidal MOT is around half the capture velocity of the six-beam MOT. Nevertheless, the study proceeded by finding the best direction from where to send the atoms in the chamber. It appears that in the pyramidal MOT that would be either from the top with a small angle from the vertical axis, or from the direction $(0, 1/\sqrt{2}, 1/\sqrt{2})$ with 90° symmetry in respect of the vertical axis (see fig.3.9). Sending atoms from the top is not a viable solution since we need to have a clear space from that direction to send the main beam. For this reason, the best balance of detuning an power for sending the atoms is been simulated with atoms starting from the direction $(0, 1/\sqrt{2}, 1/\sqrt{2})$.

The results of the simulation using different parameters of detuning and power are shown in fig. 3.10. Even when optimising power and detuning, using a pyramidal MOT we can at best hope to have a capture velocity of $\approx 50\%$ the one of a six-beam MOT.

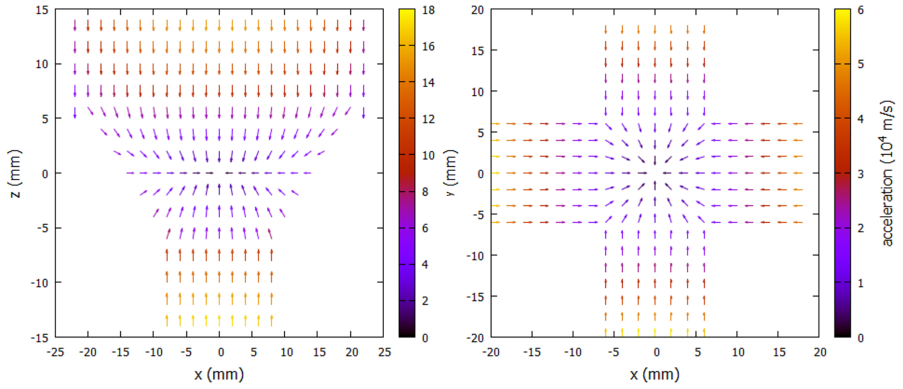

Figure 3.7: Acceleration of the atoms in rest calculated by the simulation for pyramidal MOT.

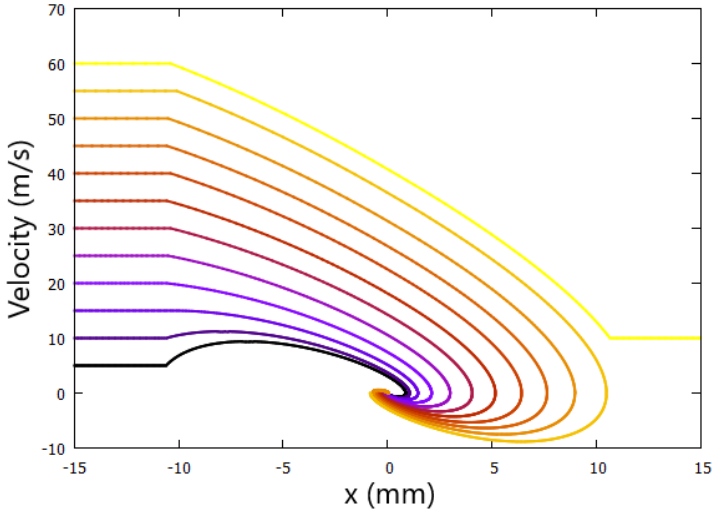

Figure 3.8: The trajectory of the atoms inside the pyramidal MOT. This figure has been generated similary to fig. 3.3, but in this case the atoms start in position (15 mm, 0,0). With these parameters we can achieve a capture velocity of 55 m/s.

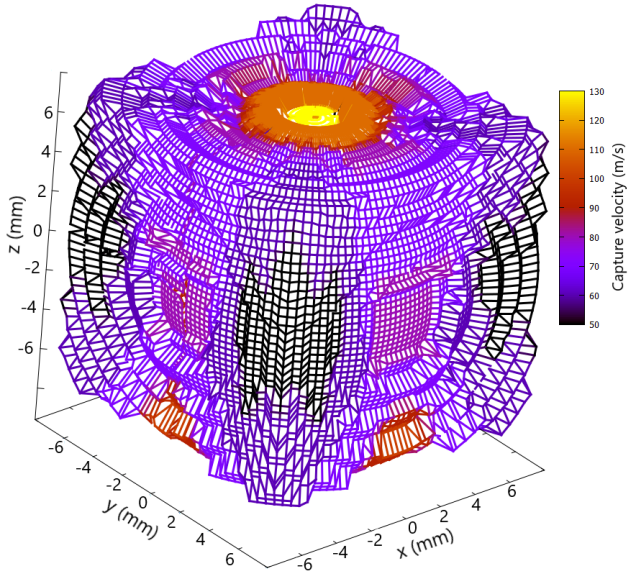

Figure 3.9: Dependency between the capture velocity and the direction of the atoms. The figure in the simulation is defined by the space where the six beams that form the pyramidal MOT overlap. In this simulation it is possible to see the best positions to place the source of atoms.

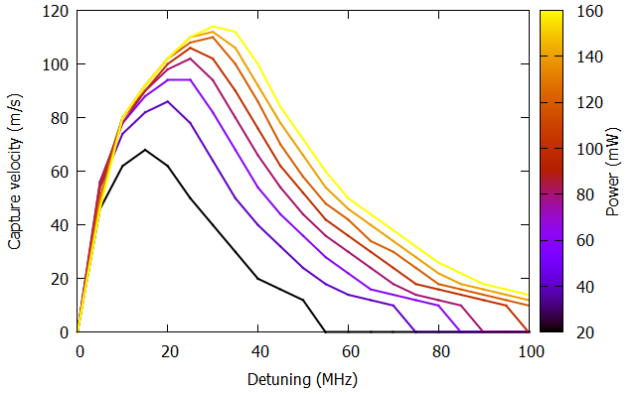

Figure 3.10: Dependency between the capture velocity, the power and the detuning of the slowing beam in a pyramidal MOT. Here the atoms have a starting velocity $\vec{V_0} = v(0, 1/\sqrt{2}, 1/\sqrt{2})$ where $v > 0$, and the starting position is (0, -20 mm, -20 mm).

3.3. Tetrahedral MOT

In a tetrahedral MOT, instead of using four or five mirrors as in pyramidal MOT, three mirrors are used. This solution, even though it is very similar to pyramidal MOT, has the advantage of forming the MOT outside of the region of the mirrors, enabling more optical access to the atoms. This makes a tetrahedral MOT more flexible than a pyramidal MOT.

For a beam with intensity I_0, the intensity of the light reflected in the radial direction is $I_\perp = RI_0 \sin(2\alpha)$ and in the vertical direction is $I_\parallel = 3RI_0 \cos(2\alpha)$ where R is the reflectivity of the mirrors (fig. 3.11). To balance the intensity in the vertical direction, we need to have $\alpha \approx 35.26°$ or use mirrors with reflectivity < 1.

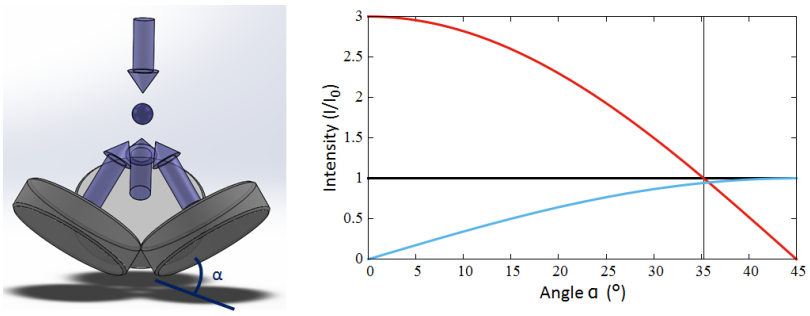

Figure 3.11: Schematic representation of the tetrahedral MOT (left). Intensity of the reflected light in the vertical (red) and radial (blue) direction, compared with the intensity of the beam sent (right).

3.3.1. Simulation

Unless specified differently, the parameters of the simulation are the same as described above for the simulation of the pyramidal MOT.

The study of the tetrahedral MOT starts by calculating the acceleration produced by the cooling beam on a static atom (fig. 3.12). However, in this case, it was not possible to find a configuration that would produce a stable MOT. The power at the centre of the main beam is higher than the power reflected by the mirror. This effect can be partially reduced by increasing the waist of the main beam. However, assuming that the total power stays the same, the acceleration is reduced due to the lower intensity of the beam. A solution can come in the form of engineered diffusers [3] that can produce top-hat

[3] like the engineered diffusers from thorlabs model ED1-C20

intensity profile eliminating this problem.

Another peculiarity of this MOT is that a large portion of space around the MOT is illuminated by a single beam, producing a region of space where the net force is not directed at the centre of the MOT. Those unbalanced forces have the result of deviating some atoms away from the MOT before they can reach the area where the forces are compensated. Because of this, there is a minimum capture[4] velocity. Atoms with a velocity lower than that are not captured by the MOT (see fig. 3.13).

The next phase was to find the best entering angle for the atomic beam. Since it is already being ascertained that a top hat beam gives a better result than a Gaussian one, the next simulations are being run only for flat beams. In fig. 3.14 it is possible to see the change in capture velocity with the angle of entrance of the beam in the MOT. Contrary to the previous scheme, for this simulation it was necessary to find also the dependency between the entering angle and the minimum capture velocity. The direction with the maximum capture spread ($V_{min} = 40\,\mathrm{m/s}$ $V_{max} = 160\,\mathrm{m/s}$) is at $\approx -29°$ in respect to the z-axis, $\approx \pm 60°$ and $\approx 180°$ in respect to the x-axis.

To conclude the study of this configuration the dependency of the capture velocity from the power and the detuning was calculated (see fig. 3.15). Surprisingly, the capture velocity of the tetrahedral MOT is higher than the one of the pyramid MOT, even if the actual number of atoms captured could be lower due to the presence of a minimum velocity needed to reach the centre.

[4]With minimum capture velocity, is intended the minimum velocity that the atom need to have to be catured by the MOT.

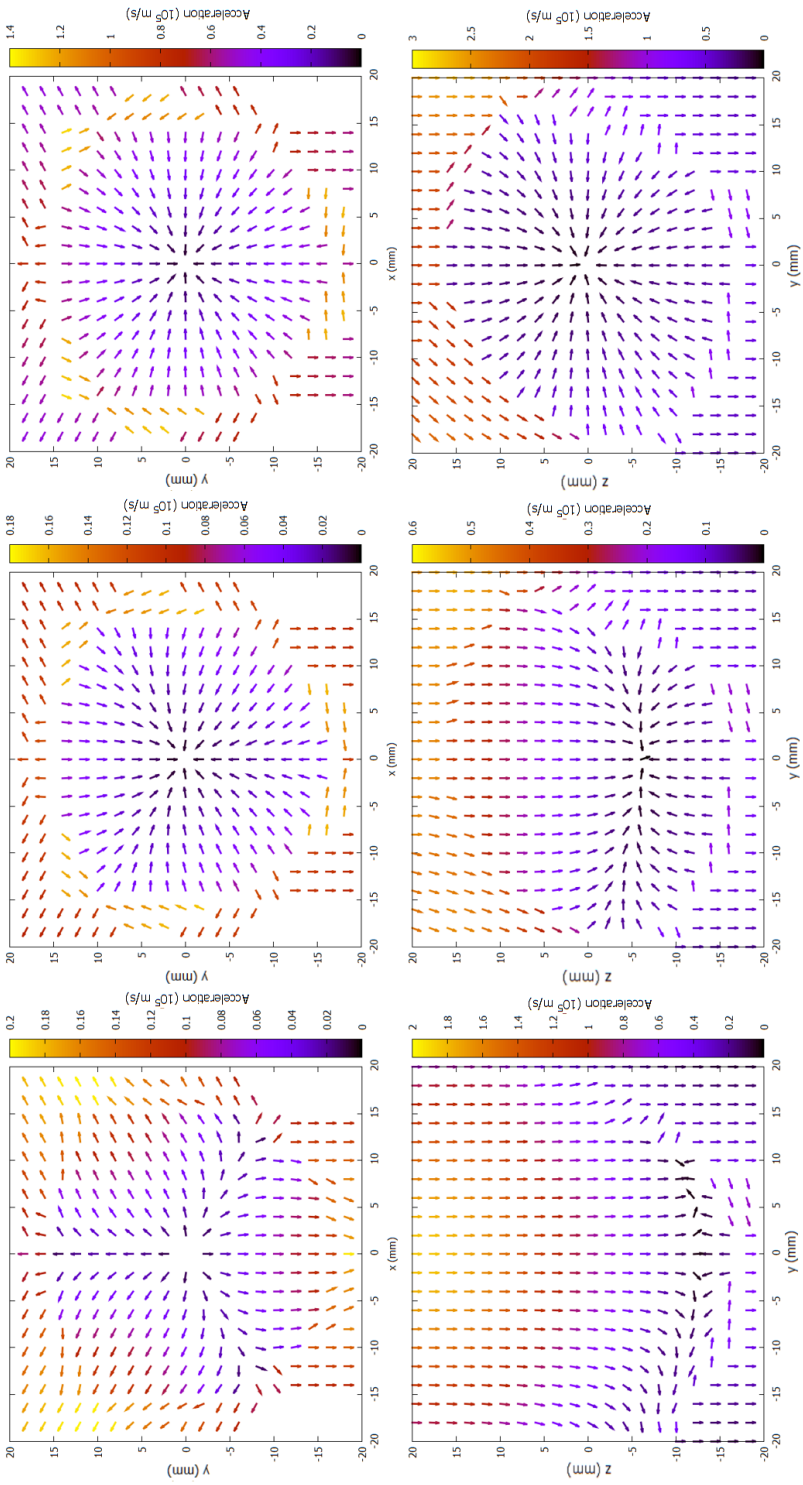

Figure 3.12: Acceleration of atoms in a tetrahedral MOT when the atoms are at rest. On the figures on the **left** the main beam has a waist of 25 mm, in the **central** figures the main beam has a waist of 50 mm, and in the figures on **right** the beam has a flat power profile.

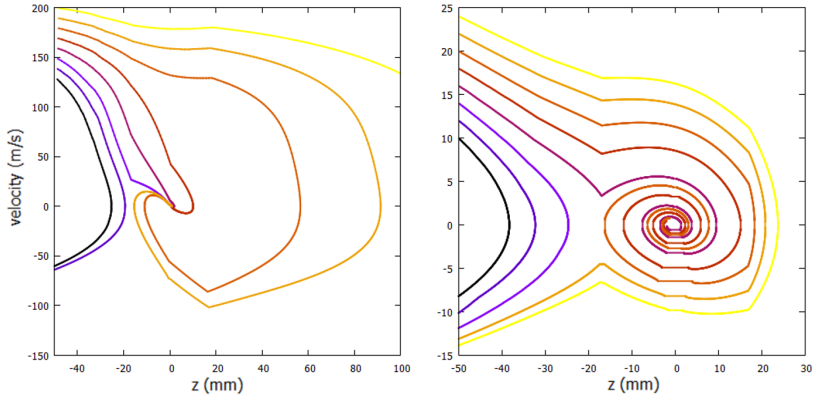

Figure 3.13: The trajectory of the atom in a tetrahedral MOT with a top hat beam (left) and Gaussian beam (right). Is important to notice the difference in scale and that in the simulation there is not an upper limit for the z-direction. In a real system some of the atoms could hit the windows used to deliver the light before being captured, so the chamber needs to be designed accordingly.

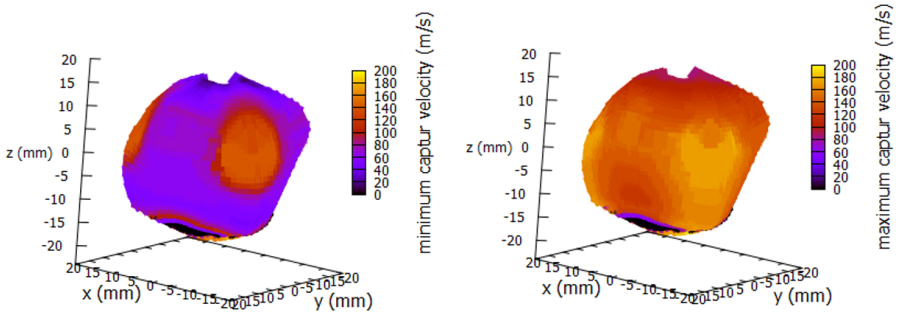

Figure 3.14: Simulation of the capture velocity of the trap from different angles. Minimum velocity required for the capture (left), maximum capture velocity (right). The trajectory is calculated starting from 10 mm from the centre of the MOT, and top heat profile is used for the beam. The beam used in this simulation has a flat power profile since a Gaussian beam would produce a narrow window of capturable velocity as shown in fig. 3.13.

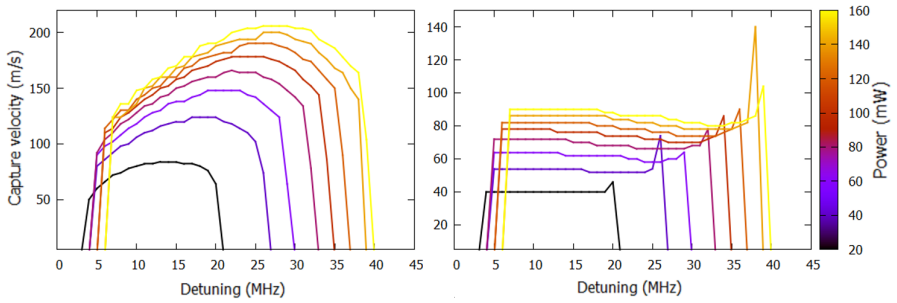

Figure 3.15: Effect of power and detuning on the minimum (left) and maximum (right) capture velocity. Here the atoms have a starting velocity $V_0 = v(0, 1/\sqrt{2}, 1/\sqrt{2})$ with $v > 0$ and the starting position is (0, -20 mm, -20 mm).

3.4. Conclusion

This chapter reports the results of the study of three different MOT schemes for strontium. For the study a numerical simulation is used to calculate the force acting on the atoms at any given moment when illuminated by the cooling beam.

These simulations allow us to determine the maximum speed that an atom can have to be captured, along with the best direction from where to send the atoms to be cooled.

This study was conducted to choose the best cooling scheme to use in the long-range interaction experiment.

This study also shows that although the pyramidal and the tetrahedral MOT represent compelling cases of study, between all the schemes considered, the six-beam MOT appears to be the most efficient to capture fast atoms.

The smaller footprint and the reduced sensitivity to misalignment do not justify the use of pyramidal or tetrahedral MOT for this experiment. However, these simulations also show that those other schemes can be used to cool and trap strontium 88. Worthy of notice is also the effect of a Gaussian beam on tetrahedral Sr MOT and the effect of the direction of the atoms on the capture of them.

CHAPTER 4

Experiment description

In this chapter the experiment built at the University of Birmingham to study the long-range interaction in strontium atoms is described in detail. The components that are described here are the direct results of my PhD, with the exception of the actual implementation of the self-assembled Zeeman slower, the coil for the MOT and the locking system for the 689 nm laser. The experiment can be subdivided in five main part:

- **Vacuum system**, this contains the atomic sample and creates a low pressure environment which avoids the interaction between the Sr atoms and the gas in the air.
- **Magnetic fields generation**, magnets and coils provide the magnetic fields needed to cool the atoms and define the atomic structure.
- **Lasers generation and control**, laser beams are used to cool, trap and probe the atoms. This system is the most complex part of the experiment and was the most difficult to realise.
- **Imaging and Detection**, it is required to extract information from the atomic sample.
- **Computer control** that is responsible for running the actions needed to perform the experiment with precise timing.

4.1. Vacuum system

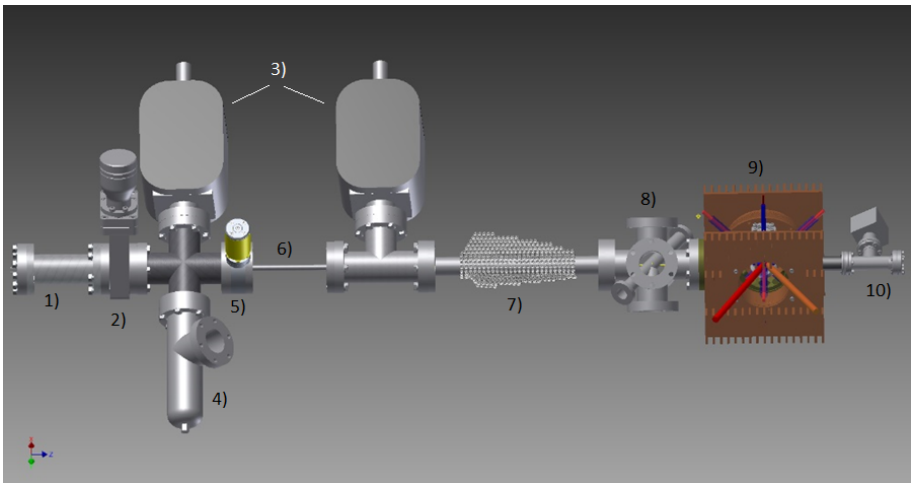

Figure 4.1: A 3D rendering of the vacuum system: 1) oven, 2) gate valve, 3) 25 l/s ion pump, 4) Angle valve, 5) atomic shutter, 6) differential pumping, 7) Zeeman slower, 8) 6+2 Way Crosses, 9) Science chamber, 10) 2.5 l/s ion pump and sapphire window.

The metal vacuum chamber is constructed mostly using stainless steel, unless otherwise stated. At the junctions between vacuum components, oxygen-free copper gaskets are used, the viewports are made from Kodial glass, and the connections are CF35. On fig. 4.1 starting from the left, there is the oven, where the atoms are heated and vaporised, forming the atomic source for the experiment. This oven is based on the design used in the SOC 2 apparatus [88]. It consists of a stainless steel chamber where the strontium is stored, the atoms can escape from an aperture filled with capillaries that ensure a tightly collimated beam. Around this strontium storage chamber there is a ceramic heater, which is surrounded by an aluminium heat shield that decreases the black body radiation emanated by the heating element. The whole assembly is kept in place by steal rods connected to a CF35 flange with electrical feedthroughs that connect to the heating element.

After the oven, a gate valve is installed, this valve is usually open to allow the stream of atoms to reach the chamber. When the valve is closed, it isolates the oven from the rest of the system. Allowing to recharge the oven without the need to break the vacuum in the rest of the system and to avoid oxidation of the strontium in case the rest of the system needs to be open.

Following the gate valve, there is a four-way cross. The cross connects an angle valve (used to create the initial vacuum with a turbo pump) and a 25 l ion pump to the rest of the system. Up to this point the pressure inside the system during the normal operation is around 5×10^{-8} mbar. The vacuum in this region is limited by the presence of the oven. When operated the oven reaches the temperatures of $< 800\,K$ relishing volatile elements. This is demonstrated by the drop in pressure when the oven is switched off, or if the gate valve is closed.

The four-way cross is followed by an atomic shutter. This allows the flux of atoms being delivered to the science chamber to be interrupted if required. Installed down-stream from the atomic shutter is a differential pumping tube that is formed from a 10 cm long pipe with 5 mm diameter. As the name suggests, the differential pumping creates a difference in pressure between two parts of the vacuum system. With these dimensions, a pressure of two-orders of magnitude lower is achieved in the section with the science chamber compared with the section with the oven.

Another 25 l ion pump is connected by a 'T' pipe to the differential pumping tube. This is followed by the Zeeman slower module. The Zeeman slower is formed from a 20 cm long nipple made of stainless steel, with an external diameter of 27 mm and internal of 21 mm. A series of magnets are attached to the outside of this section of the vacuum chamber to create the magnetic field required for a functioning Zeeman slower (see. 4.2.1).

After this is a 6+2 way cross with windows mounted on each side. This cross would allow the addition of a 2D MOT before the science chamber, however at this stage this has not yet been implemented.

Finally, furthest away from the atomic source, there is the science chamber. This is formed by a regular octagon constructed from titanium, its sides are of length 35 mm, and it is 36 mm deep. The science chamber is shown in fig. 4.2, this chamber is attached to the rest of the vacuum system via a CF35 flange. The following is in reference to fig. 4.2:

1). The opposite face of this CF16 flange connects the chamber to a 2.5 l/s ion pump and a Sapphire[1] windows via a 'T' pipe 2). On the top of the chamber a D50 CapaciTorr from Sales group and a window are present 3). On

[1]The Sapphire has been chosen due to its desirable properties, i.e. sustain structural integrity at high temperature and does not react with the Strontium atoms. Surrounding the sapphire window, a resistive coil is place to periodically provide Ohmic heating to the window and eliminate the deposits of strontium which are formed during the normal operation of the experiment.

the bottom, a CF16 window closes the chamber 4). On the remaining small side, the chamber is sealed using 30 mm windows attached with an indium seal 5-8). On the larger sides, 60 mm CaF2 windows are attached with indium to the chamber; these windows are made of CaF2 since this is transparent to the 2.6 μm laser.

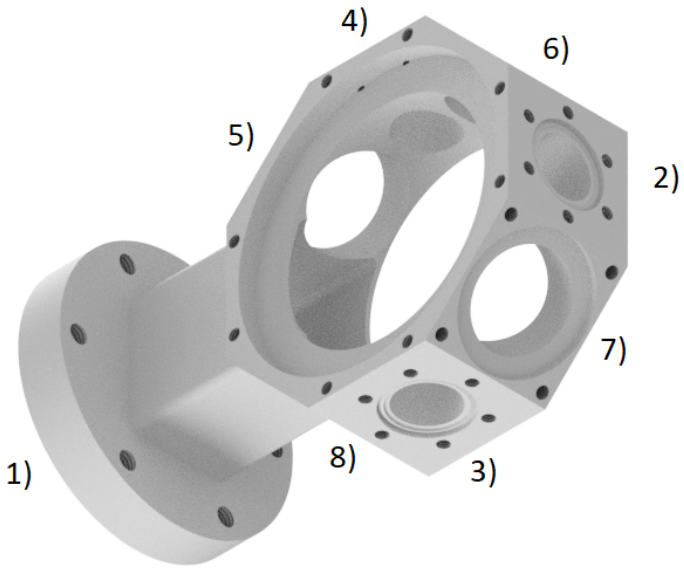

Figure 4.2: CAD rendering of the science chamber.

4.2. Coils and magnets

4.2.1. Zeeman slower

The magnetic field required for pre-cooling of the atoms (see ch.2.2.1) is generated by a series of NdFeB spherical magnets. The magnet configuration is produced by applying an initial "adhesive layer" of the spherical NdFeB magnets. This first layer is kept in position by the magnetic force generated by the magnets themselves. The magnets that compose the adhesive layer are arranged in a configuration so that the total magnetic field is zero along the central axis of the Zeeman slower, and the configuration is stable. After that, other layers of magnets are added to obtain the desired magnetic profile. The absence of

any external mechanical structure, other than the magnets themselves, makes this novel Zeeman slower easier to build and more flexible compared to other permanent magnet setups [64, 66].

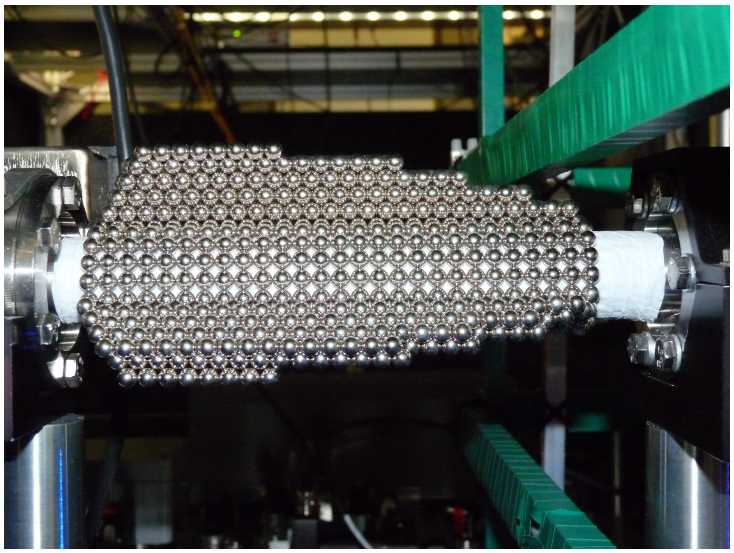

Figure 4.3: Self-assembled Zeeman slower.

4.2.2. MOT coils

The coils used to generate the magnetic field needed for the magneto-optical trap are made from 330 turns of 1 mm copper filament. The filament is wound around a copper core that has the role of keeping the coil in place and to transfer the heat generated by the coil out to the heat sink. The core has a 3 mm cut to limit the remaining of eddy current when the magnetic field is changed. The space between the turns in the core is filled with thermal paste to increase the heat transfer rate. The heat sink is made of copper as well and it is cooled by a constant stream of air generated by two 15 mm re-purposed computer fans.

The coils are connected to the chamber by screws, are separated by a 2 mm thick plastic sheet to avoid transferring the heat generated by the coil into the chamber.

The two coils are connected in series with an H-bridge electronic switching circuit between them. The H-bridge enables to change the direction of the current in the second coil. Using a TTL signal, is it possible to switch between

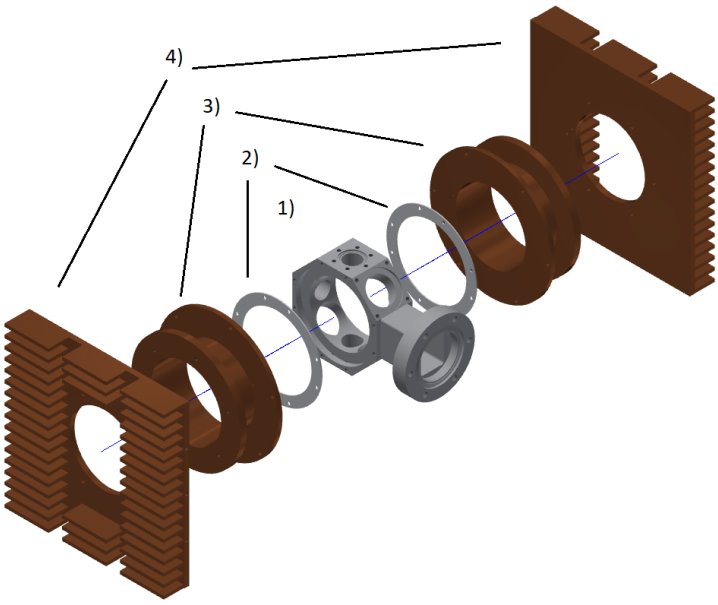

Figure 4.4: Render image of the science chamber. 1) Titanium science chamber, 2) thermal isolator, 3) copper support for coil, 4) heat sink

Helmholtz and anti-Helmholtz configuration in few ms.

During normal operation, the coils are in anti-Helmholtz configuration, generating $\approx 50\,\mathrm{G/cm}$ of magnetic field gradient near the centre. In this condition, the coil operates at 4.5 A, dissipates 127 W of power and it reaches thermal equilibrium at temperature of 48 C°.

4.2.3. Compensation coils

Parasitic contributions to the magnetic field in the chamber are always present and originate from the natural earth field and from the magnet assembly of the ion pump. Those parasitic contributions change the position of the atoms and affect the energy of the atomic transition due to the Zeeman effect.

The change in position of the atoms during the transfer of the atoms from blue to red MOT is particularly critical. In the red MOT phase the gradient of the magnetic field is ≈60% of the one used in the blue MOT. The efficiency of the transfer is limited by the change of the magnetic field minimum position[2] induced by parasitic fields.

[2]where the atoms are confined

To cancel those parasitic magnetic fields, three pairs of coils has been set in place. These coils have a square profile, they are formed of 90 turns of 1 mm copper wire, and are held in position by an aluminium frame. The size and position of the compensation coils have been chosen to allow easy access to the chamber and to compensate for a large area around the MOT.

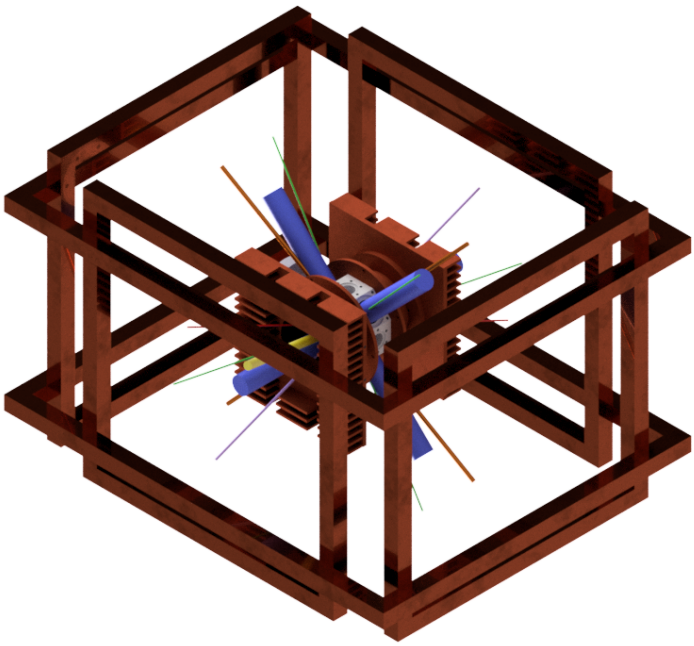

Figure 4.5: Science chamber with compensation coil around it.

4.3. Laser system

4.3.1. 461 nm laser

The light for the pre-cooling (Zeeman slower), blue MOT and detection are all generated by a commercial Ti:Sapphire laser emitting at 922 nm (SolsTiS produced by Msquare[3]) plus an external cavity doubler (SolsTiS ECD-X produced by Msquare[4]).

This system can generate up to 550 mW of light at 461 nm. This power is divided into four branches using polarising beam splitter (PBS) and half waveplate (HWP): 1) Zeeman slower, for the first stage cooling, 2) Probe beam

[3]http://www.m2lasers.com/solstis-ecd-x.html
[4]http://www.m2lasers.com/solstis-ecd-x.html

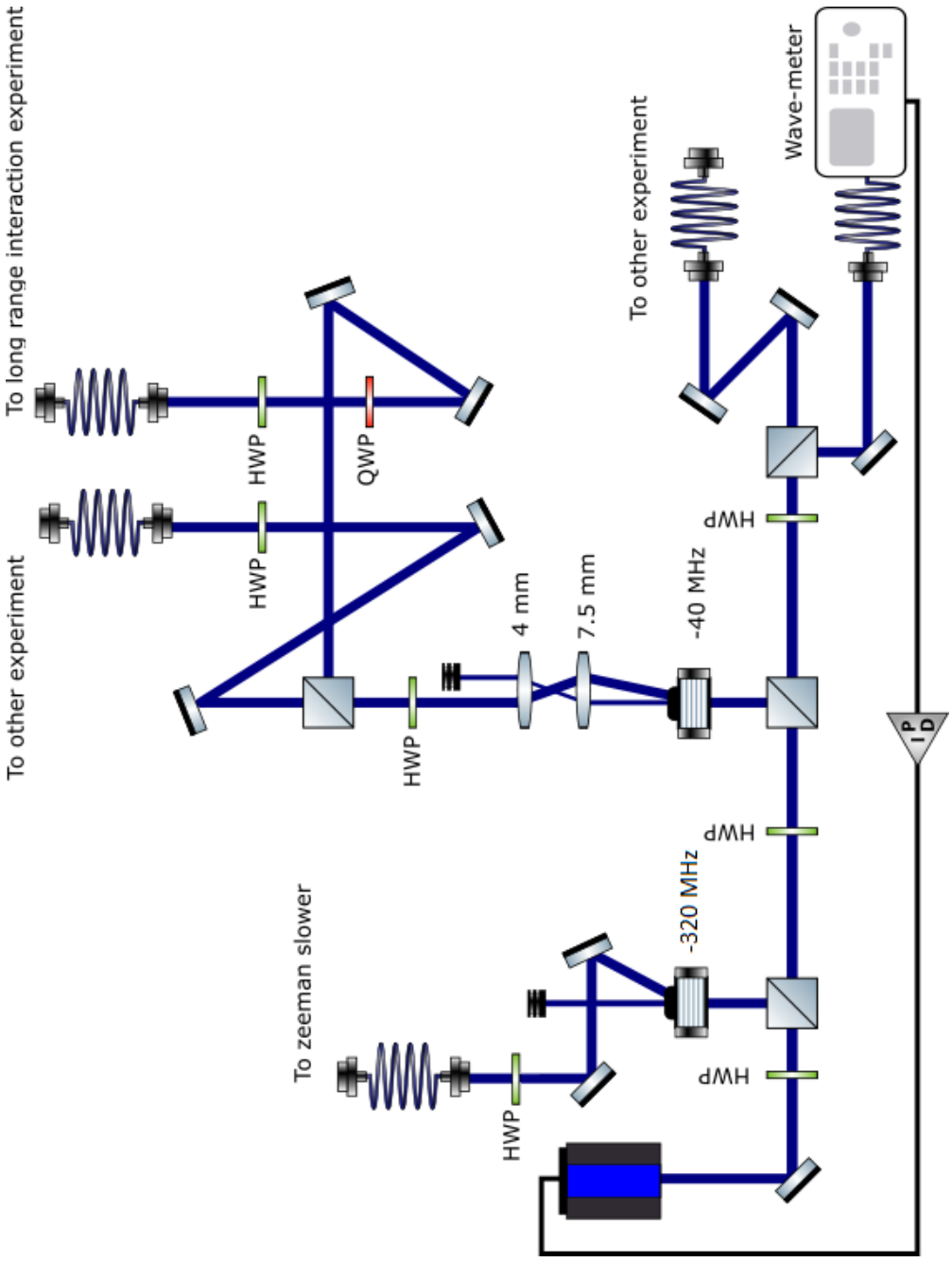

Figure 4.6: Set-up for the 461 nm laser

3) wave-meter monitoring 4) towards the experiment. The frequency of the laser is locked at +19 MHz from the transition by a PID loop that is controlled by the wavemeter. The wavemeter (WSU2 from highfinesse) has a resolution of 500 kHz and it is periodically calibrated using a SLR-780 rubidium reference laser.

Before impinging on the atoms, the light used by the Zeeman slower is shifted using an acousto optic modulator (AOM) driven by -320 MHz signal. The light is shifted by the AOM with 80% of efficiency. The signal to power the AOM is generated by a DDS (model EVAL-AD9959). This DDS generates the frequencies to control the AOMs in the cooling beam and 707 nm lasers branch. Before the fibre coupler (which delivered the Zeeman slower to the vacuum chamber via optical fibre), a laser shutter has been put in place to stop the light interacting with the atoms after the loading of the MOT is finished. The polarisation of the laser has been matched with the fast axis of the P.M. fibre using an HWP that is placed before the fibre coupler. This decreases the fluctuation in polarisation due to the mechanical and thermal stress on the fibre. At the fibre output, the light emitted has a power of 20 mW. The laser beam is then circularly polarised using a quarter wave-plate (QWP), expanded to 20 mm and then focused to a distance of 75 cm to have the maximum intensity at the region of the Zeeman slower and minimum at the MOT.

The frequency, as well as the power, of the cooling beams are controlled by a 40 MHz AOM. After the AOM, the beam passes through a telescope to decrease its size. This is done to increase the coupling efficiency into the fibre down the line. Another an HWP and a PBS combination is used to divide the beam between this experiment and other experiments performed by this group. Similarly to the case of the Zeeman slower beam, before entering the fibre, the polarisation of the beam is matched to the fast axis of the fibre using a QWP and an HWP. On the other side of the fibre, a PBS is used to increase the polarisation purity of the output light. The beam is then overlapped with the 689 nm laser beam, (required in the second stage cooling), using a long pass dichroic mirror (model DMLP567). The beam is then divided into three parts, each part is circularly polarised using achromatic QWP and expanded using a circle tophat engineered diffuser (model ED1-C20-MD from Thorlabs). This diffuser gives a constant intensity to the beam over its cross-section. The beams are also expanded to a dimension of 1 in. The beams then enter the science chamber as shown in fig. 4.7. On the opposite side of the chamber, mirrors together with QWPs reflect the beams into the chamber, reversing the

direction of their polarisation at the same time.

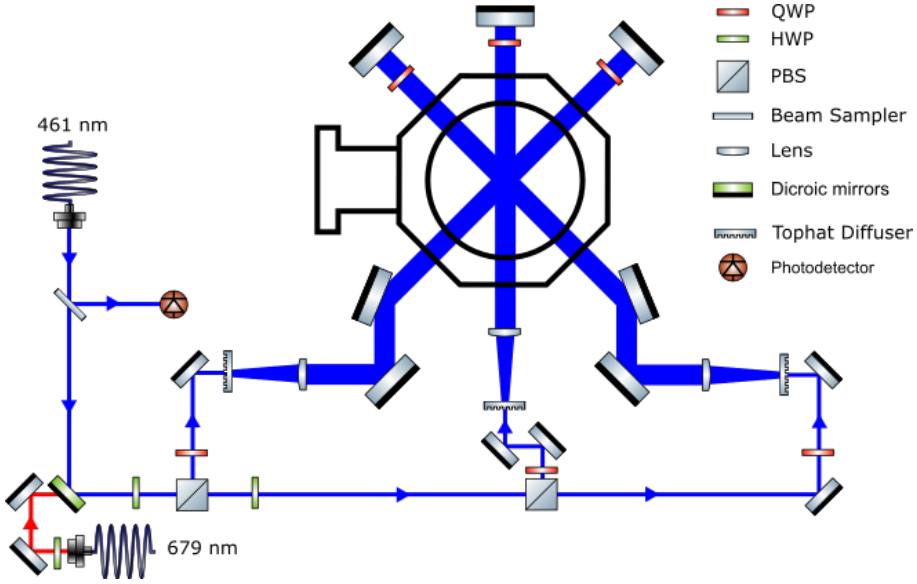

Figure 4.7: Delivery system to the science chamber of the MOT beams.

4.3.2. 707 nm laser

The light required to pump the atoms away from the $^3P_2$ state is generated using a home built IFECDL (see ch.4.3.7). The light of this laser is divided into four parts: 1) delivered to the science chamber, 2) wave-meter monitoring, 3) directed towards a transfer cavity for the stabilisation (see ch. 4.3.8), and 4) sent towards other experiments inside the cold atoms group. The light is delivered to the long-range interaction experimental chamber via optical fibre. The power of the laser reaching the atoms is 2.5 mW and the beam has a waist of 3 mm.

4.3.3. 2.6 μm laser

A beam at 2.603 μm is produced by a DFB laser diode from laser 2000. The laser has a power 7 mW. After exiting the laser, the beam is sent to an AOM. Varying the power sent to the AOM, it is possible to change the efficiency with which the beam is deflected. In this way, is possible to regulate the power of the 2.6 μm laser beam using a voltage signal.

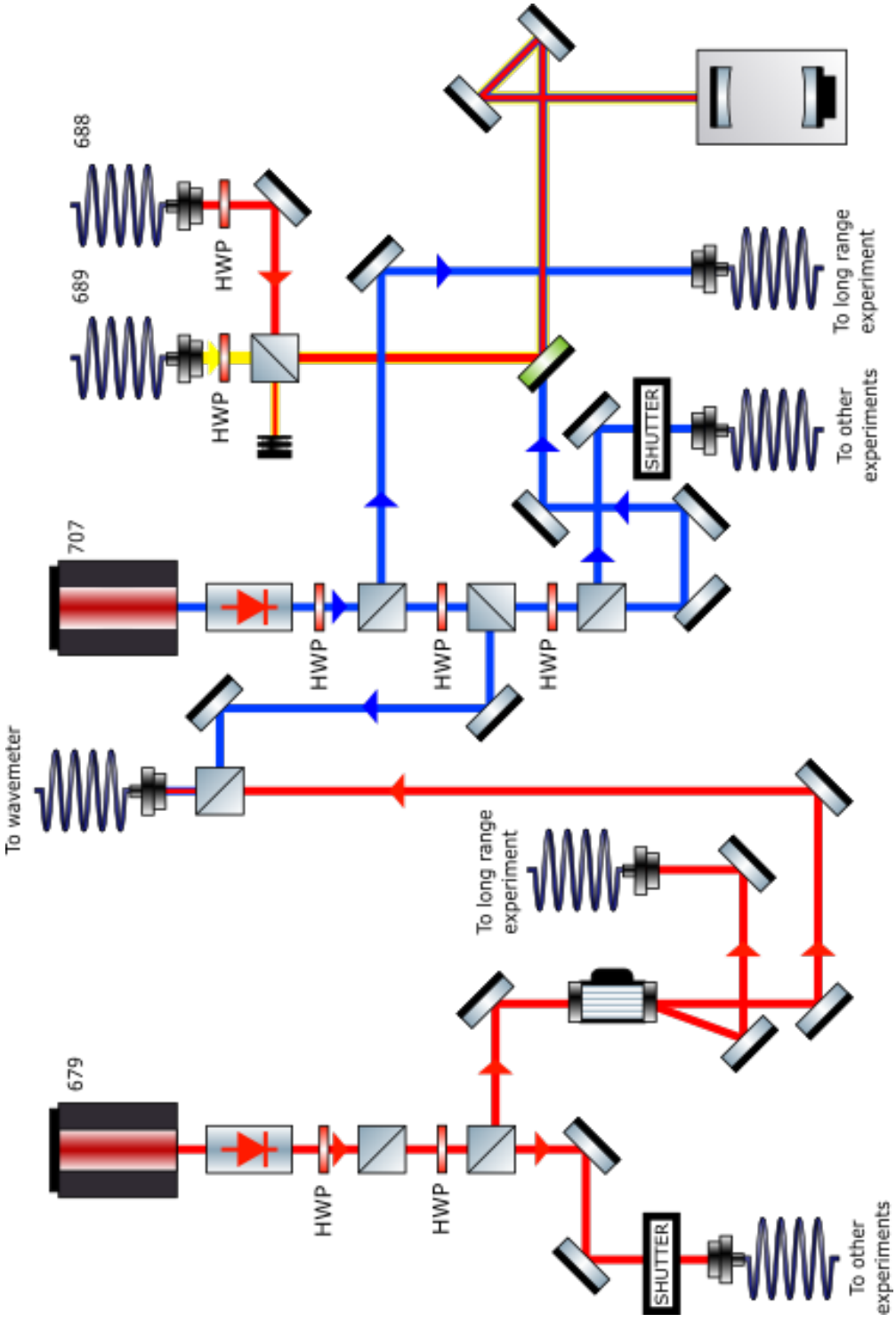

Figure 4.8: Set-up for the repumps lasers.

The 2.6 μm laser is in the short-wavelength infrared and hence entirely invisible to the human eye and most cameras. This makes the alignment of this laser extremely difficult. The only way to "see" the beam is by using a liquid crystal detector card. These cards change their colour in response to their temperature, in this way when the beam hits the card heating a certain spot, the colour of the card will change reviling the presence of the beam. This process can take up to several seconds. To overcome those difficulties in alignment, a 679 nm laser beam has been overlapped with the path of the 2.6 μm laser, using a flip mirror it is possible to switch between the two beams. The 679 nm laser also has the advantage of being in resonance with the ${}^3P_0 \leftarrow {}^3S_1$ transition. This makes it possible to see the effect the light directly using the MOT, i.e when the laser is aligned correctly and is passing through the MOT results in the number of atoms in the MOT being increased (see ch. 5.3.3).

The laser is then divided into three branches using beam sampler: 1) Enables external monitoring using a wavemeter, 2) photodiode for monitor the power 3) the bulk of the power is sent to the chamber.

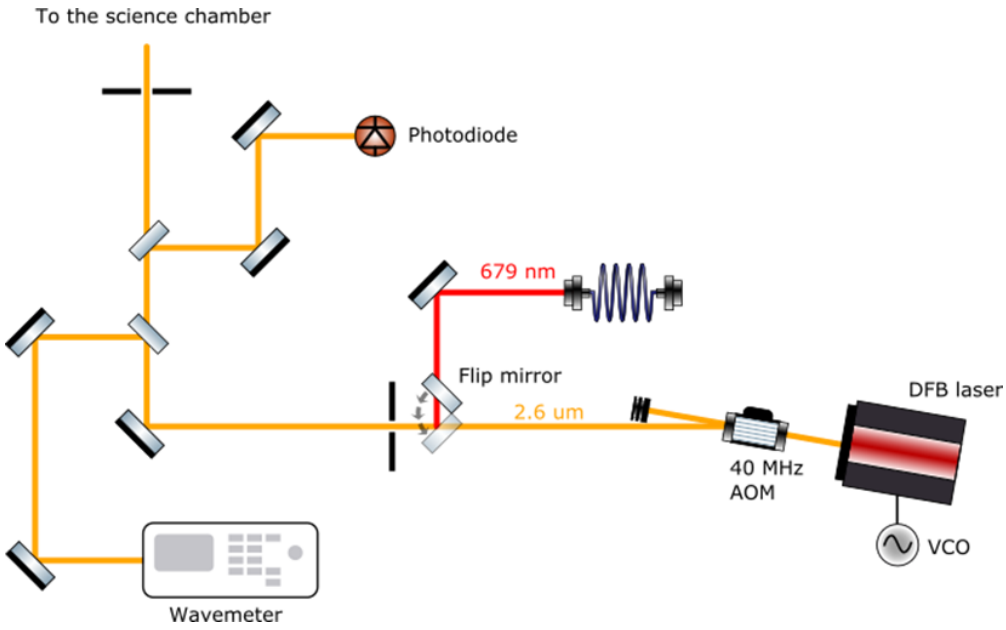

Figure 4.9: Set-up for the 2.6 μm laser.

Beam profile.

To create a coherent excitation of the $^3D_1$ state, precise control of the intensity of the beam is required. The intensity depends on the power and the dimensions of the laser beam. The power is easily measured using thermal power sensor, such as the S401C from Thorlabs. The dimensions of the beam are more difficult to measure. Since the beam is invisible, a direct measure of its waist is not possible. To measure its dimensions the knife-edge technique [89, 90] has been implemented .

Figure 4.10: Schematic representation of a knife-edge method used for beam-waist measurements.

The knife-edge technique, measures the variation in the intensity across a beam, as the portion of a barrier is interposed between the beam and the detector (fig. 4.10). Assuming a Gaussian beam, the resulting signal as a function of the position of the barrier is:

$$I = \frac{1}{2}\left[1 + erf\left(\frac{x - x_0}{\sigma\sqrt{2}}\right)\right], \tag{4.1}$$

where erf is the error function, x_0 the position of the centre of the beam, and σ is the beam waist. To obtain the profile of the beam, it is sufficient to differentiate eq. 4.1. Alternatively, in the case of discrete measure, calculate the difference in intensity between two measurements:

$$I = \frac{V_n - V_{n-1}}{x_n - x_{n-1}}, \tag{4.2}$$

with V_n the intensity of the beam reaching the detector during the n-th measure, and x_n the position of the barrier during that measure.

The result of these measurements is shown in fig. 4.12. The data shows that the 2.6 μm laser beam has a periodic structure in the horizontal direction, the cause of this structure is not clear however likely due to the DFB structure. A four-peak Gaussian distribution was fit with the horizontal data, this shows

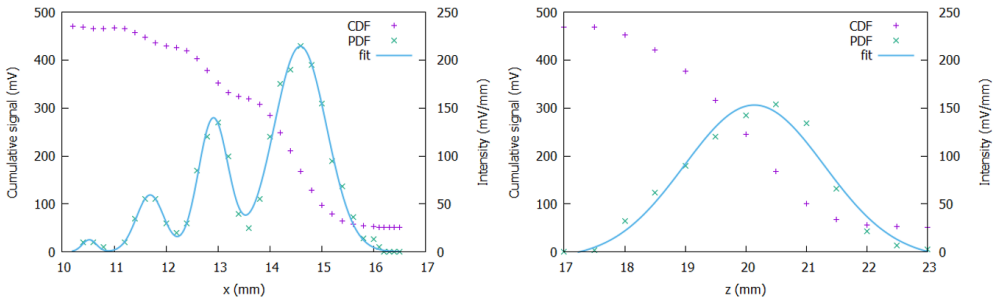

Figure 4.11: Measure of the profile of the 2.6 µm beam using the knife edge technique in the horizontal(left) and vertical direction (right).

that the highest peak has 50.3% of the power and its dimensions are $\sigma_x = 1\,\text{mm}$ and $\sigma_z = 2.3\,\text{mm}$.

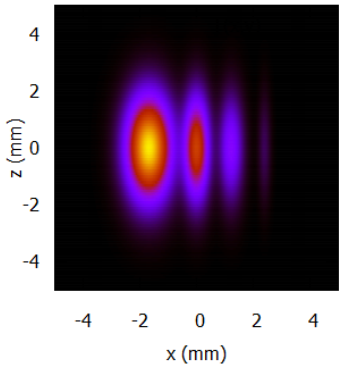

Figure 4.12: Reconstruction of the beam intensity using the knife-edge technique.

Stability of the wavemeter

While using the 2.6 µm laser as repump, it was observed that the frequency of the laser as measured by the wavemeter was shown to change by several tens of MHz, although the fluorescence of the MOT was stable. This has been taken as a sign that the stability of the wavemeter was lower of the stability of the laser in free run. To ensure that, the 2.6 μm laser was side locked to the transition using the fluorescence of the MOT as signal and the frequency of the laser recorded with the wavemeter. The result of that measurement is shown

in 4.13.

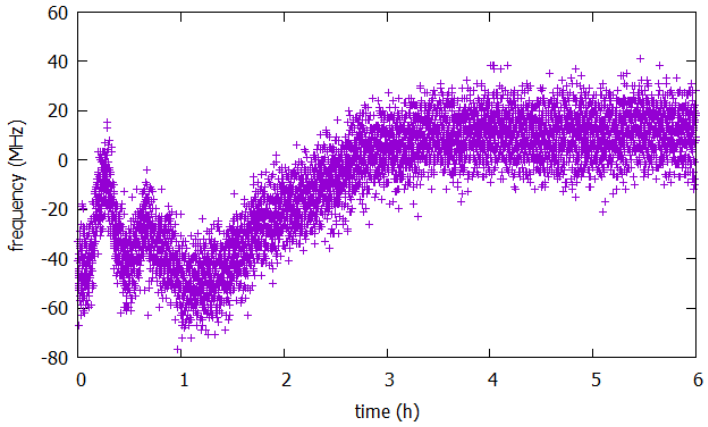

Figure 4.13: Measure of the 2.6 μm laser as recorded by the wavemeter while the laser was lock to the transition.

This measure has been taken during the night to minimise drifts caused by the environment and is possible to see how after an initial period, the wavemeter remain stable with an oscillation of $\pm$ 25 MHz (see fig. 4.14).

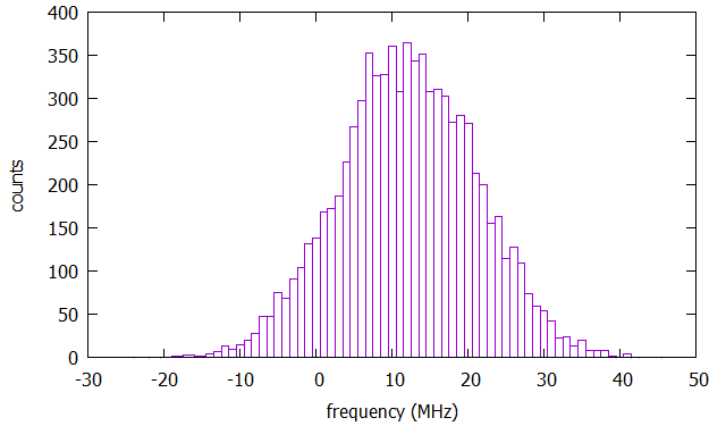

Figure 4.14: Occurrence of the measure of frequency in function of the frequency (same data of fig. 4.13), in this graph are reported only the measure took after the initial stabilisation of the laser ($t > 3h$).

4.3.4. 689 nm laser

For the second stage cooling, a commercial ECDL laser coupled with a Tapered Amplifier (TA) from Toptica [5] is used. In order to increase the stability, the laser and all the optics are mounted on a breadboard that is isolated from the rest of the lab using isolating sorbothane feet and enclose in a hardboard enclosure.

The laser has two outputs: the main beam (the one after the TA) has a power of 120 mW, the other one (before the TA) has a power of 1.2 mW.

The main beam is divided using a polarising beam splitter and it is sent to the wave-meter using a fibre. The rest goes through a $\approx +80$ MHz AOM that is used to set the beam to the right frequency and to apply a 1.6 MHz modulation during the broad-band cooling phase. The beam is then injected into a polarisation maintaining (PM) fibre that delivers the light to the science chamber (see fig. 4.7).

The secondary beam is sent to a double pass $\approx$ -100 MHZ AOM and then injected in a PM fibre to be sent to a cavity, where using the PDH technique [91] it is locked to the frequency of the cavity (see fig. 4.15). The sidebands needed for the PHD are generated by modulating the current of the laser at 5.6 MHz.

The cavity consists of two high reflecting mirrors separated by double cone-shaped spacer that is made of ULE and it is 77.5 mm long [92]. The cavity has a finesse of $< 3 \times 10^5$ and a free spectral range of 1.5 GHz, resulting in a resolution of $\approx 4KHz$. The cavity is maintained under vacuum at a pressure of 9×10^{-8} mbar and has three heat shields (2 aluminium and one of steel) keep the temperature constant. Unfortunately the TEC element inside the cavity that was used to stabilise the temperature ceased to work and so an active temperature stabilisation has not been possible. The cavity is mounted on a minus-k platform on top of a 500 Kg marble table in order to minimise the vibration. The PID function is provided by a FALC from Toptica[6]. As result of the lack of temperature stabilisation of the cavity and of the absence of an absolute reference, the frequency of the 689 nm laser needs to be frequently adjusted. This is done by running the sequence for single frequency red MOT (see ch. 5.4) and optimising the transfer efficiency of the atoms in the single frequency red MOT by changing the frequency sent to the 100 MHz AOM. In

[5] https://www.toptica.com/products/tunable-diode-lasers/amplified-lasers/ta-pro

[6] `https://www.toptica.com/products/tunable-diode-lasers/laser-locking-electronics/falc-110-mfalc-110-fast-pid/`

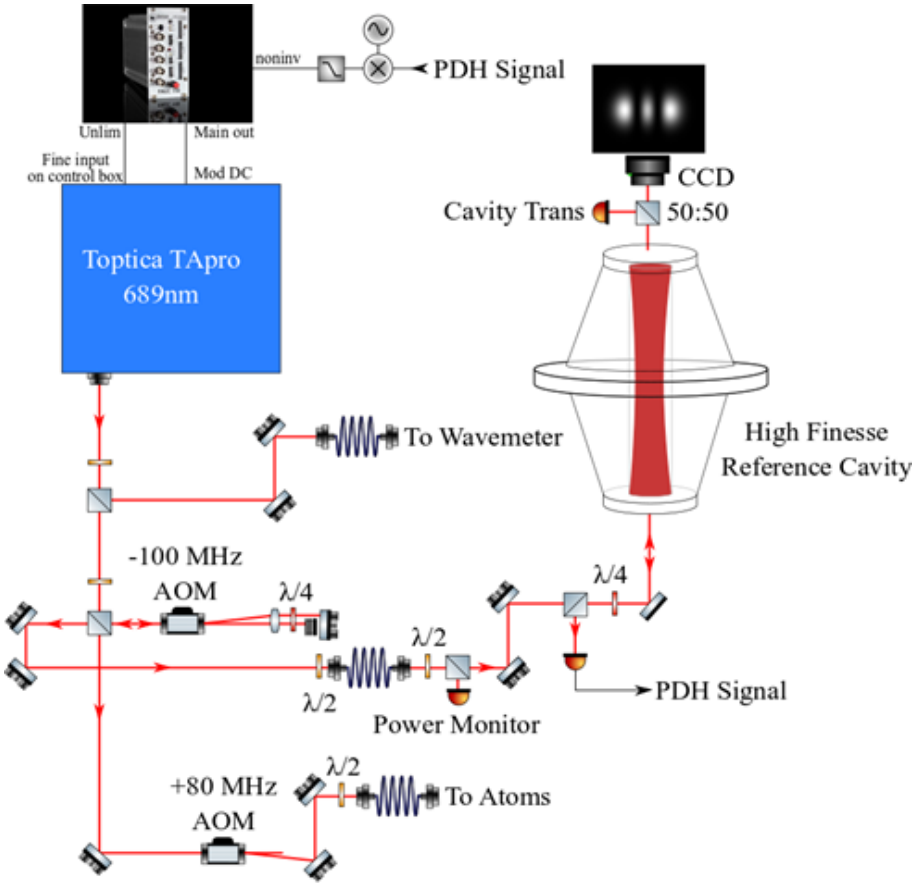

Figure 4.15: Schematic of the optical system used to lock the 689nm laser to the ${}^1S_0 \rightarrow {}^3P_1$ transition.

the future the construction of a new cavity and the realisation of fluorescence spectroscopy for the ${}^1S_0 \rightarrow {}^3P_1$ transition will solve this problem.

The frequency modulation of the cooling beam is obtained by modulating the frequency sent to the +80 MHz AOM. This frequency is generated by an arbitrary frequency generator that is set to a frequency modulation depth of 1 MHz and has an external input. The external input is connected to a RedPitaya. The RedPitaya is set to output a sine waveform, the frequency of this waveform will dictate the distance between the comb line of the laser modulation. The amplitude is responsible for the depth and the DC offset for the central frequency. Those parameters are controlled by the internal CPU of the RedPitaya, running a C program structured as a state machine. This machine has three states. The first, is for the broadband red MOT, the second is a transition from broadband and single frequency red MOT, and the last one is for the single frequency (see fig.4.16). These states are controlled by a digital signal sent by the main computer control to the RedPitaya.

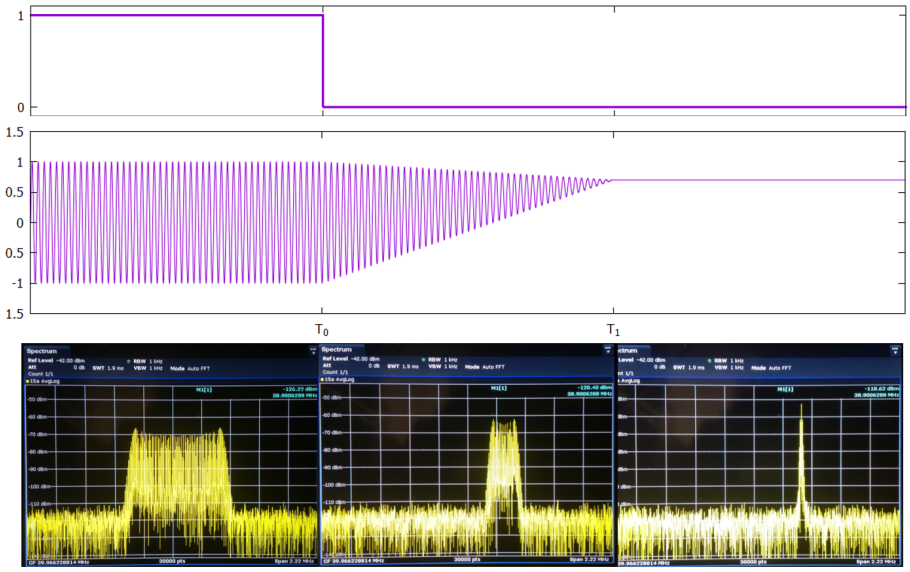

Figure 4.16: Transfer sequence from broadband to single frequency red MOT. On top, TTL signal sent to the RedPitaya by the computer control. On the centre, signal generated by the RedPitaya. On the bottom, FFT of the signal sent to the AOM.

4.3.5. 688 nm laser

The laser used for producing 688 nm light is a commercial ECDL from Laser2000 (model TEC 150-690). The output of this laser is coupled in a three-way fibre splitter. One of the branches sends the light to the scientific chamber, one to the wave-meter and the last to a scanning cavity for stabilisation (see chapter 4.3.7).

4.3.6. 813 nm laser

This laser is used for the optical lattice and is generated using a Ti:Sapphire laser emitting at 813.4 nm (SolsTiS produced by M square[7]). This laser emits up to 3 W of power at 813 nm, 10 mW of this power is sent to the wave-meter to monitor the wavelength, the remaining power is injected into a high power PM fibre. At the output remains 1 W of power, this light is then collimated by a 20 mm lens and then focused again by a 200 mm lens, resulting in a beam waist $w_0 = 50\,\mu$m. On the opposite side of the chamber, a 75 mm lens collimates the beam again, so that it is retro-reflected by a hot mirror (from Thorlabs model FM01). This 75 mm lens is also responsible for collecting the fluorescence of the atomic cloud for the spectroscopy (see fig.4.17).

4.3.7. Interference Filter External Cavity Diode Laser (IFECDL)

The majority of the lasers currently used in cold atoms labs are based on semiconductors. Typically laser diodes do not have a narrow enough linewidth to be used directly ($\Delta\nu_d \approx 40$ MHz) in a cold atoms experiment; therefore it is necessary to provide optical feedback to the diode to achieve the required performance. This feedback is produced by an external cavity [93].

The most common scheme called Littrow (fig. 4.18)[94] uses a diffraction grating to provide frequency selection back into the cavity. This configuration is sensitive to ambient pressure and optical misalignment [95]. By using an interference filter instead of the diffraction grating, the laser becomes less sensitive to these disturbances. In addition, this apparatus is extremely compact and robust [96] (fig. 4.19).

[7] `http://www.m2lasers.com/solstis-ecd-x.html`

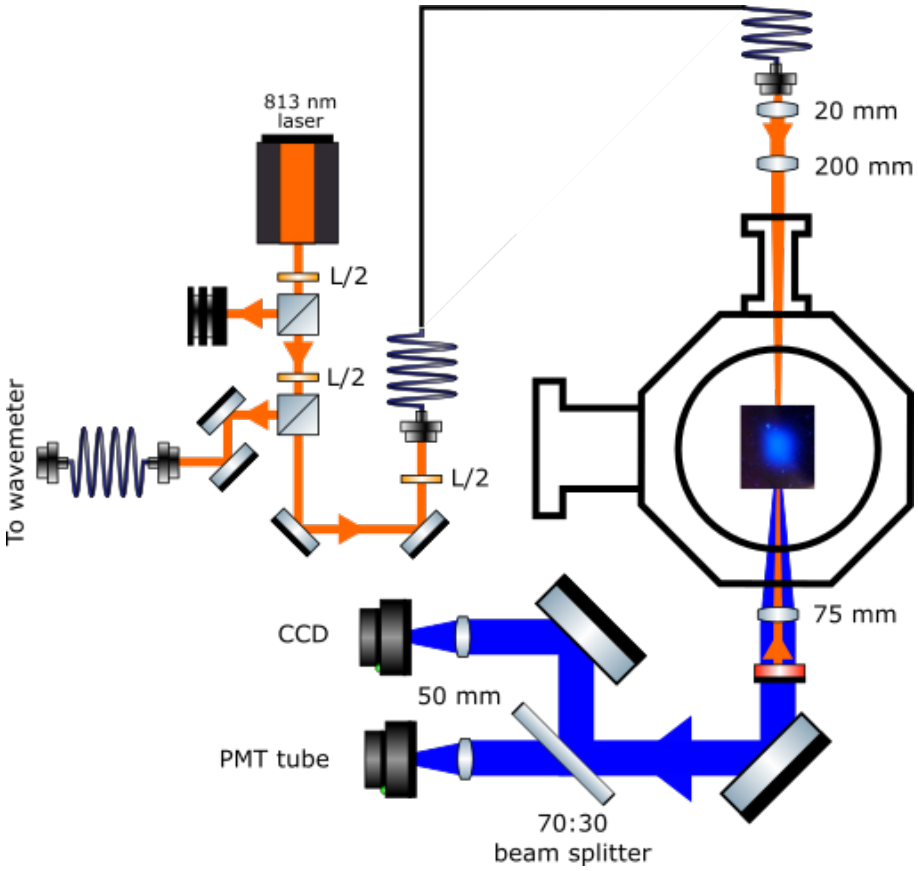

Figure 4.17: Delivery system for the lattice laser and detection setup.

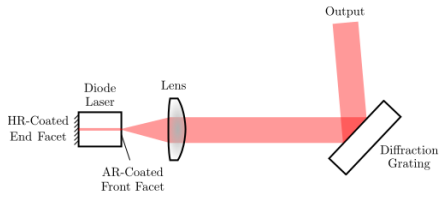

Figure 4.18: Littrow ECDL configuration.

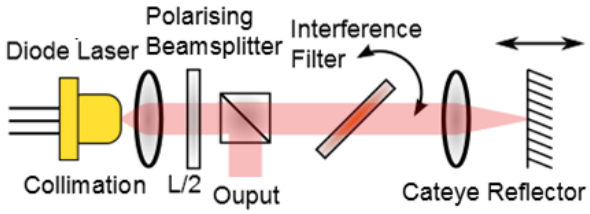

Figure 4.19: Filter ECDL configuration.

Monolithic IFECDL

The body, the filter support and the piezo support of the laser have been printed in brass by Shapeways. The diode model used is a VPSL-0690-035-x-5-A with an output power of 35 mW. The filter is a custom-made interference filter made by LASEROPTIK (fig. 4.20 and 4.21).

The wavelength of this laser can be changed from 680 nm up to 690 nm by turning the interference filter. The presence of the HWP and PBS permits to change the injection of the diode and maximise the output power. The cat-eye lens ensures the stability of the laser frequency and helps to avoid misalignment. The temperature is kept constant by a Peltier that is placed under the laser cavity, powered by a home-made PID. This unit is inserted in an enclosure made by a brass base and a plastic lid, to provide a secure connection with the electronics and to make the vacuum around the cavity to ensure stability.

The particular design of this laser permits this to be also used as a slave for another laser[8].

Characterisation IFECDL

By changing the voltage applied on the piezo it is possible to obtain mode-hop free range of 2 GHz. This measurement has been taken by measuring the wavelength of the laser using the same wavemeter as for the lock of the 461 nm laser. The laser presents a drift of $\approx 30kHz/s$, see fig. 4.22.

To measure the linewidth of the laser, the wavelength was tuned to 689 nm and the beat note between this laser and the laser used for the second stage MOT[9] has been recorded. This measure shows that the linewidth of this laser is 774 kHz (see fig. 4.23).

[8]In this configuration the filter and the cat eye mirror are not required.
[9]During this measure the laser was locked to the cavity

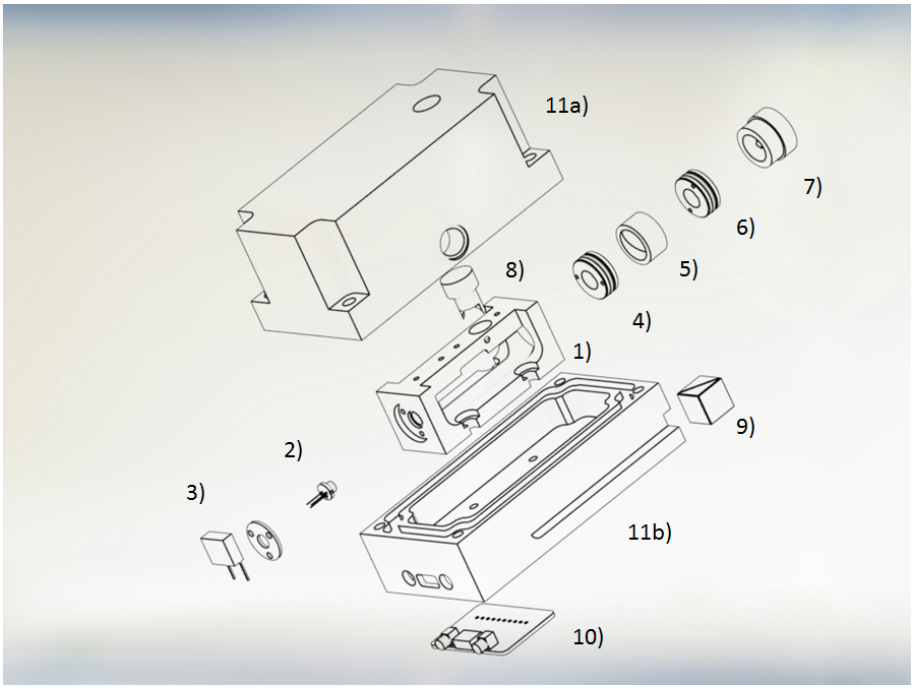

Figure 4.20: Drawing of the IFECDL. 1) Cavity, 2) laser diode, 3) diode protection, 4) collimation lens, 5) $\frac{\lambda}{2}$ waveplate, 6) cat-eye lens, 7) mirror with piezo and support, 8) filter support, 9) beam splitter cube, 10) PCB for connections, 11a) and 11b) box for the protection.

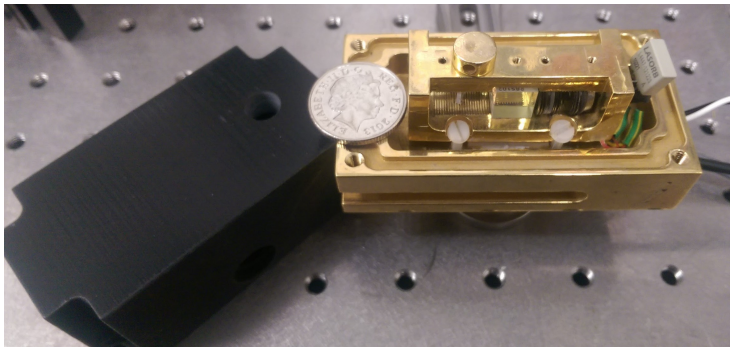

Figure 4.21: Picture of the monolithic IFECDL.

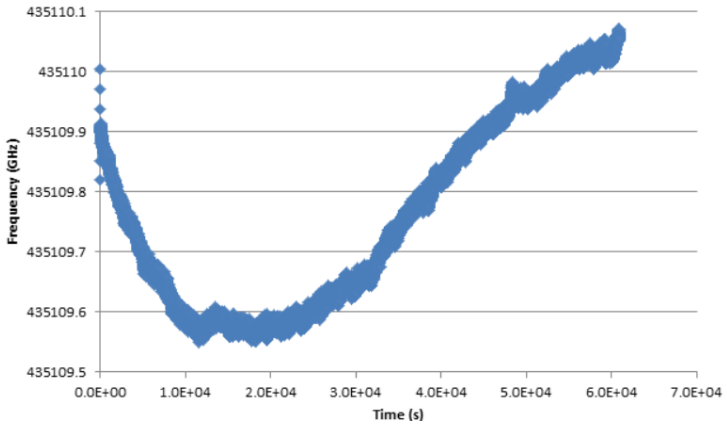

Figure 4.22: Wavelength of the IFECDL over a period of 16 hrs and 40 mins.

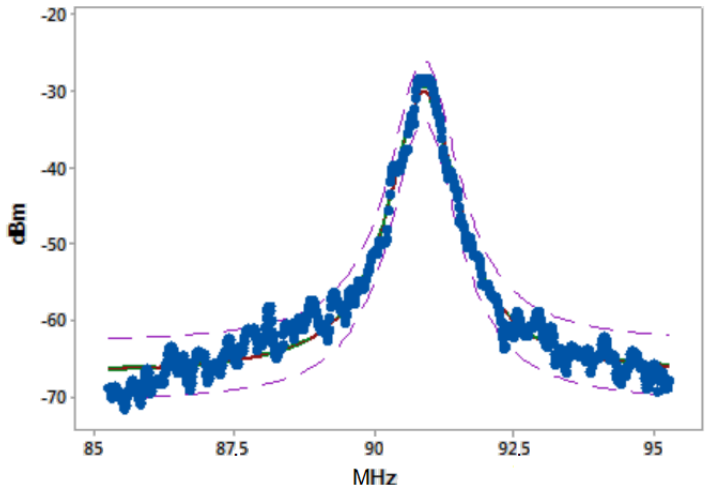

Figure 4.23: Beat note between the IFECDL end a 689 nm commercial laser locked to the cavity. This measurement has been recorded using a spectrum analyser with 100 kHz resolution and 300 µs sweep time.

4.3.8. Scanning cavity

The 707, the 688 and the 813 nm lasers require long-term stability on the order of a couple of MHz. Those lasers could be locked using the wavemeter, as for the case of the 461, but those require additional ports that are not available at this time. To solve this problem, a fast scanning cavity offset lock [97] has been set in place. This locking system is composed of a scanning cavity (the FPI-100-0750-1 from Toptica in the case of this experiment) and a stable laser. By injecting the stable laser and the laser(s) that need stabilisation into the cavity, and performing a scan of the length of the cavity using the piezo actuator, a transmission spectrum as shown in fig. 4.25 is obtained. T_1, the relative frequency spacing between a) the peak of the reference laser and b) the peak a of the laser which requires frequency locking, depends on the relative frequency of the lasers and the free spectral range of the cavity. Since the frequency of the reference laser is constant and the free spectral range is measured at each scan as T_0, keeping the ratio between the T_1 and T_0 constant, the frequency of the laser will be locked.

The "brain" of the system is a RedPitaya, in this case FPGA is used as ADC to record the signal from the cavity, and its DAC to send the signal to the lasers and cavity to keep them locked. The program running in the CPU reads 5 times per second the transmission signal from the FPGA, finds the peaks of the transmission, calculates the relative distance between them, and also generates the error signal by comparing the positions found with the ones set as the target. At this point, the program calculates the correction needed using a Proportional Integral Derivative loop to keep the lasers locked. Another signal is sent to the signal generator that controls the scan of the cavity. This signal changes the DC component of the signal which is sent to the cavity. This is done to keep the position of the first peak constant. Without this correction, the order of the peak will change over time due to drift of the cavity, resulting in a failure of the frequency lock.

Performance of the cavity

The IFECDL was not available at the time that the characterisation of the cavity was performed. The behaviour of the cavity has been tested using two ECDLs that have remained in the lab from previous experiments. Those lasers have wavelengths 707 and 679 nm. The reference laser is provided by the 689 nm laser that is locked to the high finesse cavity.

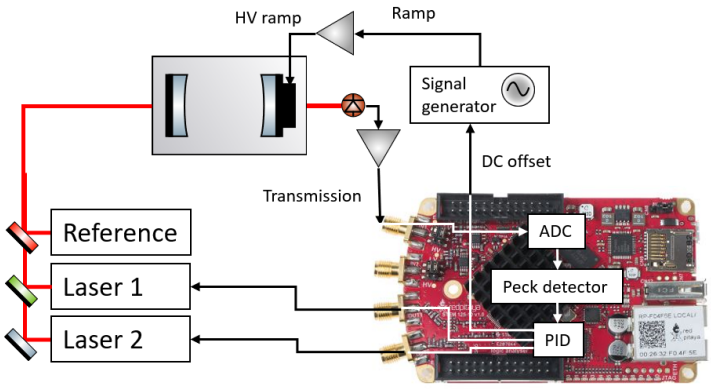

Figure 4.24: Set-up of the fast scanning cavity offset lock.

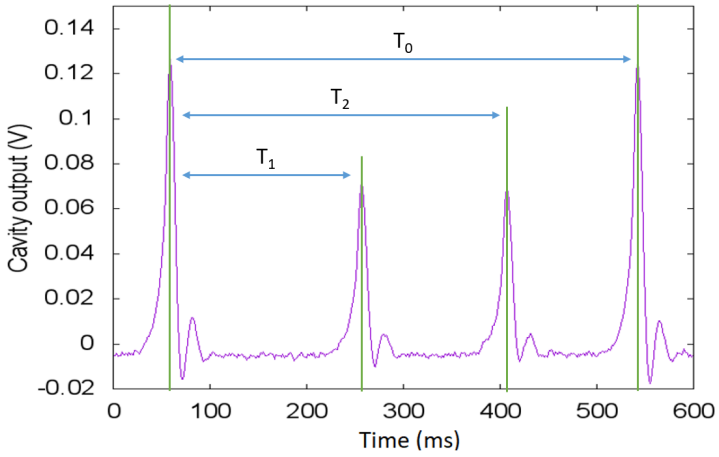

Figure 4.25: Transmission signal over the cavity, the two big peak are generated by the reference laser, the smalls peaks are generated by the lasers which are being locked to the reference laser.

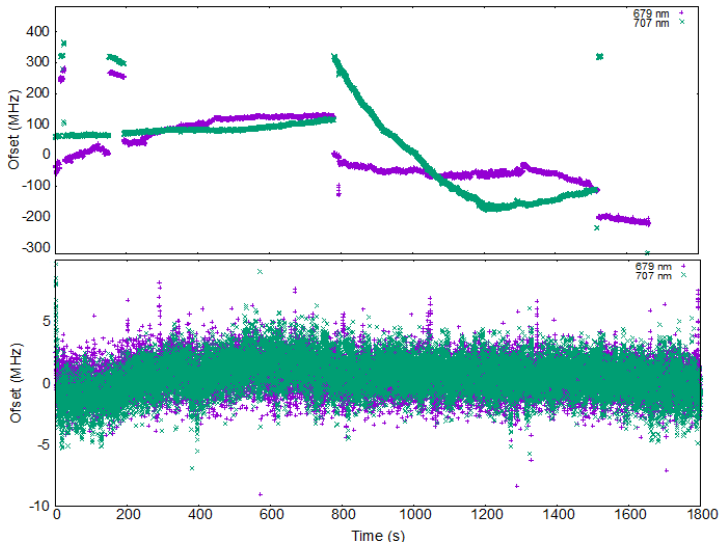

Figure 4.26: Frequency of the lasers when free running (top), and when locked using the scanning cavity (bottom).

In fig. 4.26, the frequency of the two lasers when free-running is recorded by the wavemeter. During free-running, these lasers drift in frequency by hundreds MHz over the time of a few minutes. When the lock is engaged, their frequency will not drift more than 5 MHz from the set frequency lock, making the setup suitable for the use in this experiment.

4.4. Imaging and timing

4.4.1. Camera and PMT tube

In this experiment, the atoms are revealed by the application of the 461 nm cooling beams. The fluorescence of the atoms is collimated by a 1-inch diameter lens with a 75 mm focus, positioned under the chamber. After 50 cm the light is reconstructed on the sensor of a camera (Zyla 5.5 from Andor [10]) using a 50 mm f=1 in lens. Between the two lenses, is placed a hot mirror (model FM01 from Thorlabs) and a 70:30 beam splitter. The mirror is used to create the lattice and to filter the unwanted light from reaching the camera. The beam splitter is used to divert part of the light to a PMT tube. Comparing with the camera, the PMT tube has better sensitivity, faster response and it is easier to

[10] `https://andor.oxinst.com/products/scmos-camera-series/zyla-5-5-scmos?gclid=EAIaIQobChMIveOwp-3-3QIVSPhRCh16egpuEAAYASAAEgKfBvD_BwE`

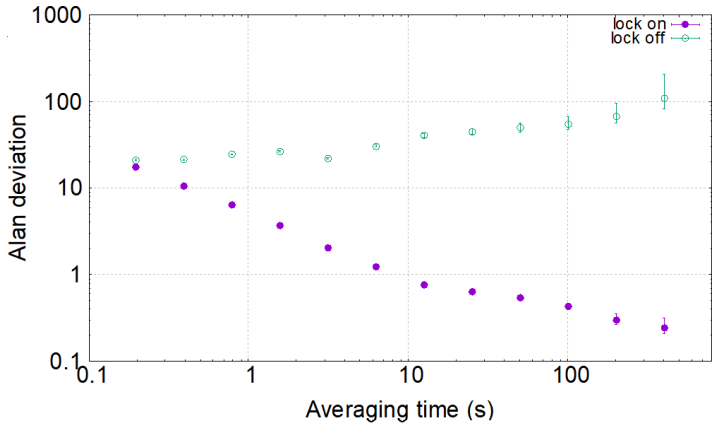

Figure 4.27: Comparison of the Alan deviation of the 707 nm laser in free running and when locked.

operate. However, it does not give any information about the distribution of the atoms (see fig.4.17).

4.4.2. Computer control

The time of each phase of the experiment is given by a field-programmable gate array (FPGA) model sbRIO 9632. The FPGA is programmed with a Python script developed here in University of Birmingham. The FPGA has 8 analogue channels with output ±10 V and 16 digital TTL outputs.

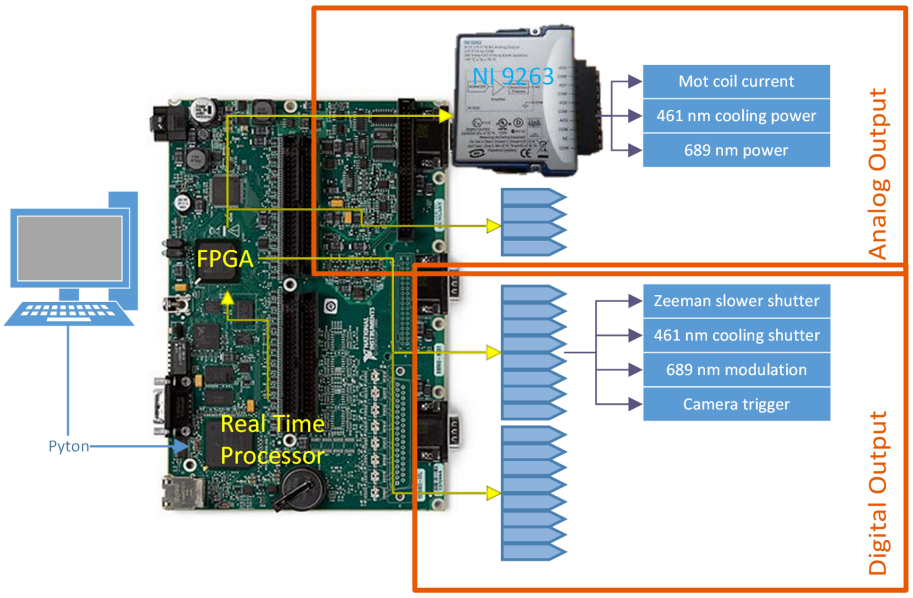

Figure 4.28: Schematic representation of the computer control.

CHAPTER 5

Result and discussion

In this chapter are reported the measurements made to characterise the cooling phases, the preliminary analysis made on the preparation of the atoms in the $^3P_0$ state, and the measurement performed on the $^3P_0 \rightarrow {}^3D_1$ transition with reference to their importance to the long-range interaction measurement.

5.1. Oven characterisation

5.1.1. Atomic flux

The atomic flux is the number of atoms per second that are sent to the science chamber at any given moment. The flux is correlated to the number of atoms captured in the MOT, and the time that is required to reach this number (see chapter 5.3.2). Absorption spectroscopy was used to measure the total flux of the atoms on the atomic beam when the oven was set at 2.48 A, and the signal was at its maximum. This absorption signal has been used to calibrate the fluorescence signal received by a Photomultiplier (PMT) set to collect the light emitted by the atoms. The fluorescence signal is then used to measure the atomic flux at lower current values, where the signal to noise ratio is too small to measure it using absorption spectroscopy (see fig.5.1).

The amount of light reaching the photo-detector follows the Beer-Lambert

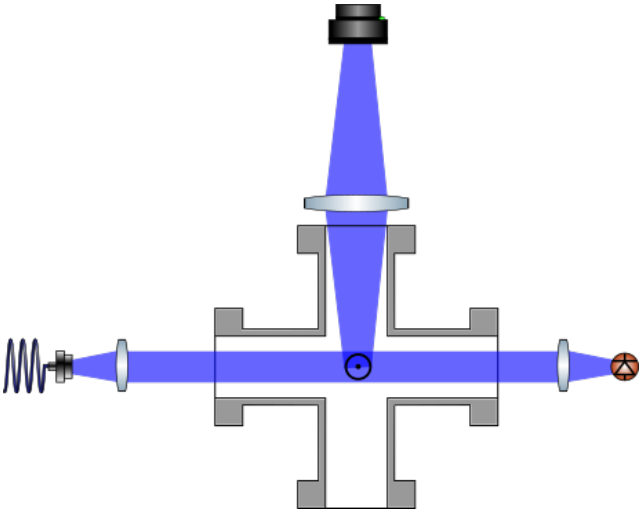

Figure 5.1: Set-up for the measuring of the atomic flux: at the centre of the six-way cross, with direction exiting the page, is the atomic beam that is crossed by the light coming from the fibre on the left. On the right, a photodiode collects the light after it has been absorbed by the atoms. On the top is the PMT that collects the light emitted by the atoms.

law:

$$P(x) = P_0 \exp(-\sigma n x), \tag{5.1}$$

where

$$\sigma = \frac{3\lambda^2}{2\pi} \frac{1}{1+s}, \tag{5.2}$$

and $s = I/I_s$. In this experiment a beam with $s = 0.06$ is used. The flux can be now calculated as:

$$\varphi = n\langle v \rangle \pi r^2, \tag{5.3}$$

where $\langle v \rangle$ is the average velocity and r is the atomic beam radius.

5.1.2. Velocity distribution

Together with the atomic flux, to assess the performance of the oven, is important to know the velocity distribution of the atoms. The atoms exiting the oven have a distribution of velocity well described by the Maxwell–Boltzmann equation [98]:

$$P(v) = 4\pi v^2 \left(\frac{m}{2\pi k_b T}\right)^{\frac{3}{2}} \exp\left(-\frac{mv^2}{2k_b T}\right) \tag{5.4}$$

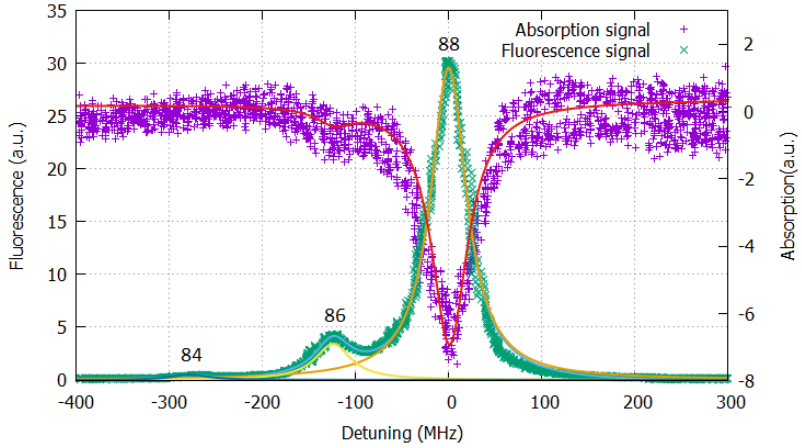

Figure 5.2: Absorption and fluorescence spectroscopy of the atomic beam in the direction perpendicular to the direction of the atomic beam. The fit is a sum of three Lorentzian distributions corresponding to the 88, 86 and 84 isotopes of the strontium. The peaks of ^{87}Sr are not visible since they are covered by the ^{88}Sr peak.

To measure this distribution, fluorescence spectroscopy on the atomic beam exiting the oven was performed. The spectroscopy was executed on the $^1S_0 \rightarrow {}^1P_1$ transition using the 461 nm laser.

The velocity of the atoms can be calculated by measuring the variation in the resonance frequency as it is shifted by the Doppler effect:

$$\Delta f(v) = \frac{v}{c} f_0. \tag{5.5}$$

The probe beam is generated by using a Ti:Sapphire laser which is frequency doubled by a (PPLN) waveguide module. By injecting 100 mW of infra-red light, 20 mW of light at 461 nm is obtained. After filtering the infra-red light the blue light is injected into a PM fibre to be used as a probe. The probe beam reaches the atoms by the same optical distribution that was used to realise the 3D MOT (see fig. 4.7). However, for this measurement, two of the beams entering the chamber and the retro-reflecting mirror were covered. The beam has a power of 1 mW, a diameter of 2 cm and a top hat profile, resulting in an intensity of 0.3 mW/cm^2, well below the saturation to avoid broadening due to intensity. Before the telescope that enlarges the beam, some of this light is sent to a photodiode to monitor the variation in intensity. The light enters the chamber with an angle of 45° in respect to the direction of the atomic beam.

The frequency of the laser is then changed using a linear scan throughout 100 s. The frequency is monitored continuously by the wave-meter.The fluorescence is measured using the PMT, with the optics set-up described in ch. 4.4.1.

Since the probe beam as at an angle of $\theta = 45°$ in respect to the atomic beam, the measured velocity is:

$$v_{measured} = v_{\perp} \sin(\theta) + v_{\parallel} \cos(\theta), \tag{5.6}$$

with $v_{\perp}$ being the velocity of the atoms perpendicular to the atomic beam, $v_{\parallel}$ the velocity parallel to the atomic beam and θ the angle between the probe beam and the atomic beam. Since $v_{\perp} \ll v_{\parallel}$ than $v_{\parallel} \approx \sqrt{2} v_{measured}$.

The result of the measurements made at different oven currents is shown in fig. 5.3. The measured velocity distribution is in good agreement with the expected result. Furthermore, using those measurements it has been possible to estimate the temperature of the oven at different currents applied.

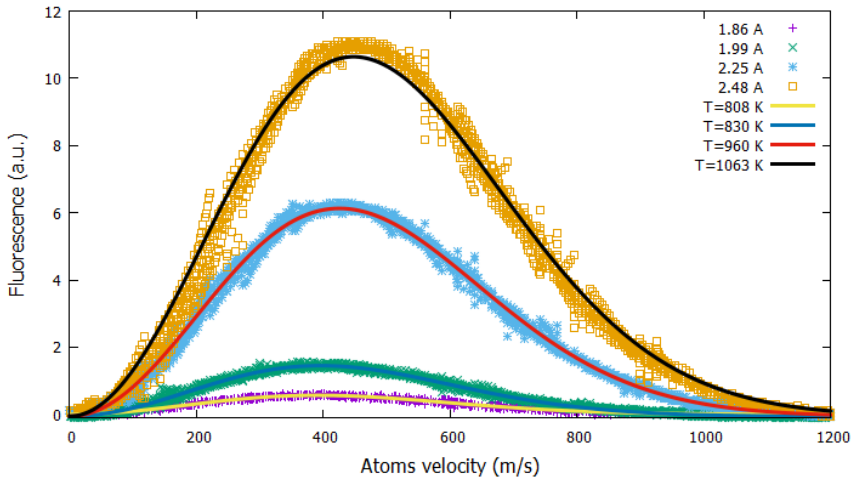

Figure 5.3: Velocity distribution on the direction of the flux and relative fit of a Maxwell-Boltzmann distribution for the different currents of the oven.

[1]The signal was too small to be measured.

Current (A)	T (K)	Flux (10^9 atoms/s)
1.71	NA[1]	44
1.86	808	140
1.99	830	277
2.25	960	1493
2.48	1063	3300

Table 5.1: Summary of the characterisation of the oven.

5.2. Precooling

5.2.1. Effect of the Zeeman slower on the velocity distribution

Once the velocity distribution of the atoms which are emitted by the atomic oven is known, it is useful to see the effect that the Zeeman slower has on the atoms. Performing the measurement of the velocity distribution again, as in the previous section (fig. 5.3) but with the Zeeman slower in operation, is clear that there is an effect from the Zeeman slower on the distribution of the velocity (see fig.5.4). The peak at the beginning of the distribution is well described by a Lorentzian distribution with centre at 94 m/s and a full width at half maximum of 26 m/s.

5.3. 1st stage cooling

5.3.1. Zeeman slower optimisation

Once the blue MOT was found, the next step was to find which combination of power and detuning of the Zeeman slower laser result in the maximum number of atoms in the MOT. As shown in fig. 5.5, the number of atoms increases with the power until it reaches a maximum, and then starts to decrease. The presence of the maximum can be explained by the fact that even if the slowing beam is several Γ away from the transition, with enough power the probability for the Zeeman slower beam to interact with the atoms in the MOT is not negligible. This is confirmed by the fact that the position of the cloud changes when the slowing beam is off or on. Based on this test, the Zeeman slower beam is set to have a power of 20 mW and a detuning of 320 MHz.

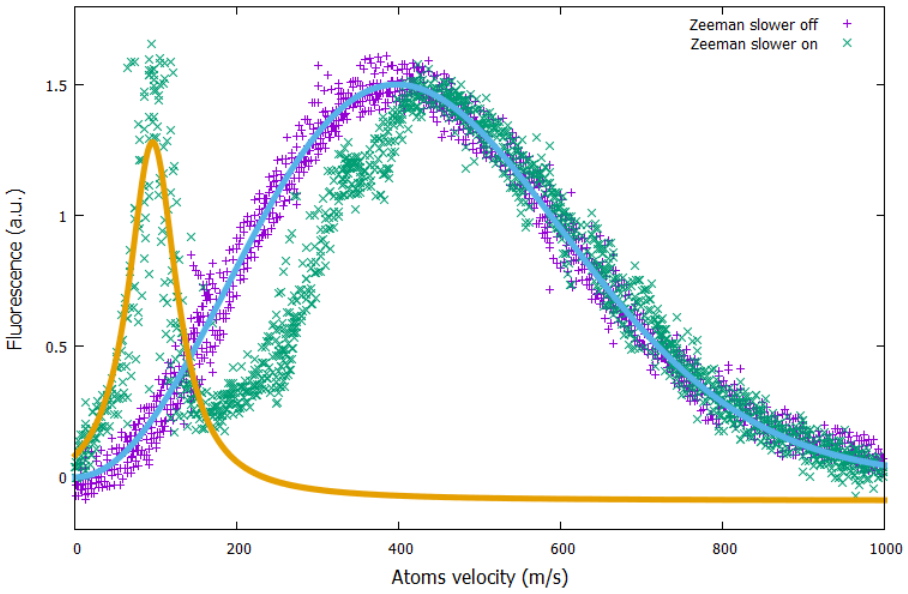

Figure 5.4: Velocity distribution of the atoms along the direction of the atomic beam with the Zeeman slower active, these data are taken with the oven at 1.99 A.

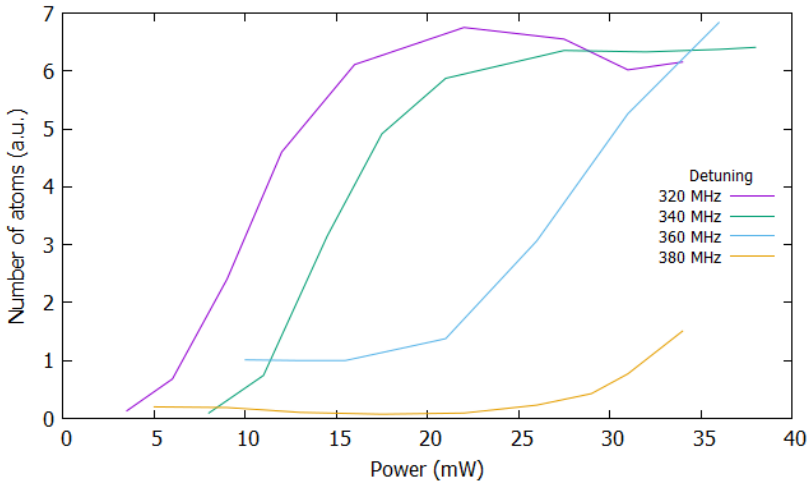

Figure 5.5: Relation between number of atoms, power and detuning of the Zeeman slower beam.

5.3.2. Background pressure and loading time

The formation of the MOT is a dynamic process. Once trapped, the atoms can escape if they collide with the thermal atoms present in the chamber, or if they collide with each other and form molecules. The loading time of a MOT is driven by the charging rate R, the collision rate with the gases in the chamber γ and from the probability of the atoms to form molecules β. In formulas:

$$\frac{dN}{dt} = R - \gamma N - \beta \int n^2 dV, \tag{5.7}$$

that results in :

$$N(t) = \frac{R}{\Gamma}(1 - e^{-\Gamma t}), \tag{5.8}$$

where

$$\Gamma = \gamma + \beta \int n^2 dV. \tag{5.9}$$

Assuming that the predominant contribution to the loss comes from collisions with the background, it is possible to estimate the pressure inside the chamber by the lifetime of the MOT [99].

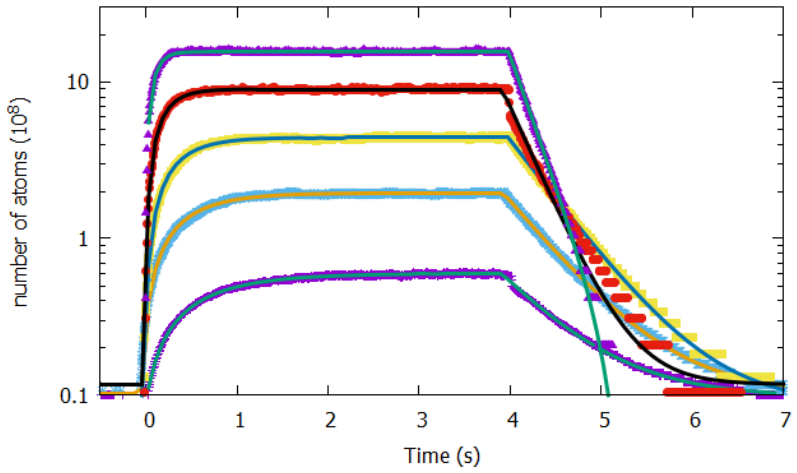

Figure 5.6: Number of atoms vs time at different currents of the oven, after 3 s the Zeeman slower is turned off and the atoms start to escape the MOT.

Current (A)	n atoms in MOT (10^8)	Loading time (s)	Life time (s)	Pressure (10^{-10} mbar)
1.71	0.5	0.64	0.67	5.5
1.86	1.9	0.45	0.62	6.1
1.99	4.3	0.32	0.57	6.8
2.25	8.8	0.19	0.33	13.2
2.48	15.7	0.09	0.27	16.5

Table 5.2: Summary of the characterisation of the first cooling stage, at different currents of the oven.

5.3.3. Repumps

To prove that is possible to use the 2.6 µm laser as repump, a comparison between the number of atoms in the blue MOT with different repumps configuration was performed. In this comparison the 679 laser has $I \approx I_{sat}$ and for the 2.6 µm $I \approx 3 \times 10^4 I_{sat}$. The results of these measurements are shown in fig. 5.7.

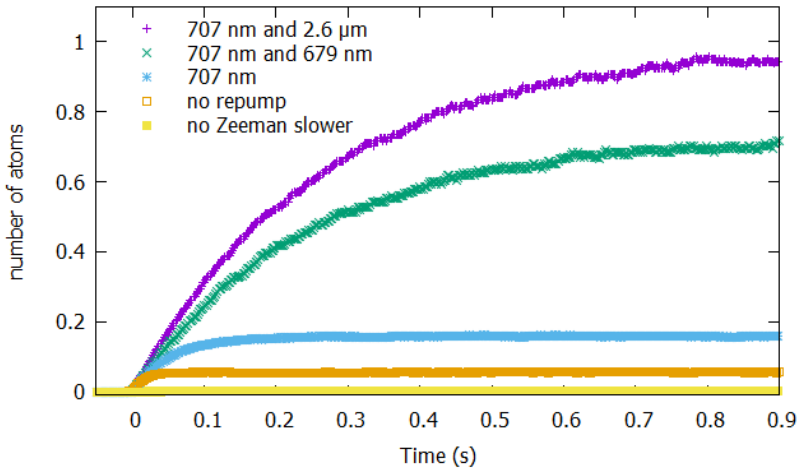

Figure 5.7: Relative number of atoms vs time with different repumps configuration.

These data do not only show that the 2.6 µm laser can be used as the repump to remove the atoms from the $^3P_0$ state, but also that using this laser $\approx$ 35% more atoms are trapped compared with the atoms trapped using the 679 nm laser as the repump. This increased number of atoms is probably due

to the power of the 2.6 µm laser. Since $I \ll I_s$ the stimulated emission of the atoms in the $^3D_1$ state reduces the lifetime of that state making the repumping more efficient. This result is particularly important for this experiment because it not only removes the need for the 679 nm laser, but also offers a simple clear method to tune the 2.6 µm laser to the transition frequency with higher accuracy than the one offered by a wavemeter.

5.4. 2ND STAGE COOLING

After the number of atoms in the MOT has reached its maximum (in around 2 s) the 461 nm laser is slowly switched off and the magnetic field reduced. At this point, the atoms are trapped by the 689 nm laser that cools them down below the temperature reachable with the 461 nm laser, due to the relative Doppler cooling limits for these wavelengths.

At the beginning of the 2^{nd} cooling phase, the laser is modulated with a deviation of 1.6 MHz, modulation frequency of 10 kHz, and it has intensity of 300 I_s. After 20 ms the modulation is ramped down and the intensity is reduced to 100 I_s (see fig. 5.8).

With this sequence, it was possible to transfer 1.4×10^8 atoms (25% of the atoms present in the blue MOT) into the broadband red MOT and 6×10^7 atoms (15% of the atoms present in the blue MOT) in the single frequency red MOT. Although there is room for improvement, those numbers are in line with what has been obtained by other cold atoms groups that use strontium [75, 88, 100, 101].

5.4.1. Temperature of the final cooling stage

To trap a significant number of atoms in the optical lattice, the temperature of the atoms needs to be lower than the equivalent[2] energy depth of the trap. Furthermore, the temperature of the atoms will affect their distribution in the lattice and accordingly the linewidth of the transition. To ensure that the atoms are cold enough for this experiment, a time of flight (TOF) [102] measurement has been performed. The TOF method measures the variation in the size of the atomic cloud over time, after all the forces that are applied to the atoms in the MOT are being removed[3]. Due to the velocity of the atoms that form

[2] $E = \frac{3}{2}kT$
[3] except for the gravity

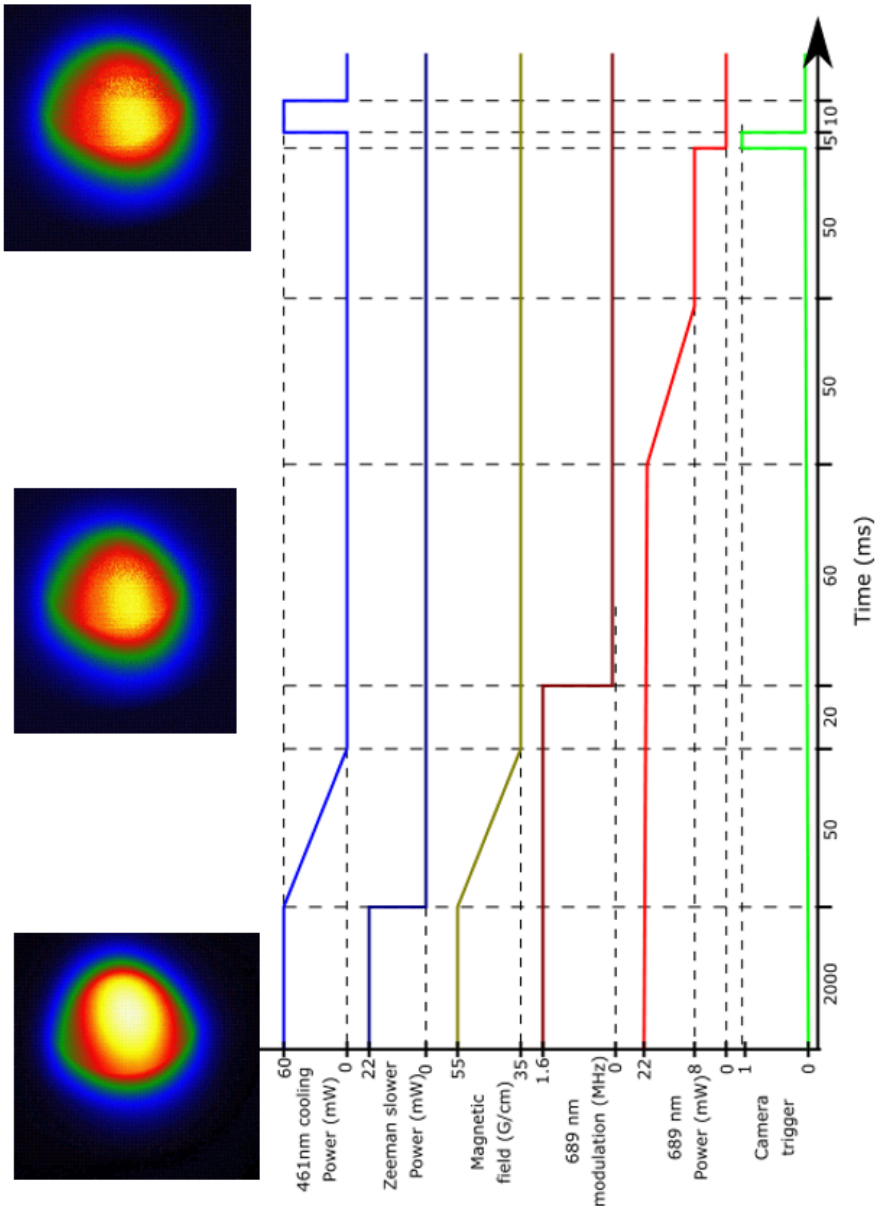

Figure 5.8: Experimental timing sequence used to achieve red MOT.

the cloud, the average size will increase:

$$\sigma(t) = \sqrt{\sigma_0^2 + \frac{k_b T}{m} t^2}, \tag{5.10}$$

where $\sigma(t)$ is the waist of the cloud at the time t assuming a 3D Gaussian distribution, σ_0 is the waist at the time $t = 0$, k_b is the Boltzmann constant, m is the atomic mass, and T the temperature in K.

This measure was taken with a camera positioned above the chamber, and the image was calibrated by taking a picture of an object with known length (a section of a rule) and measuring the length of that object in pixels.

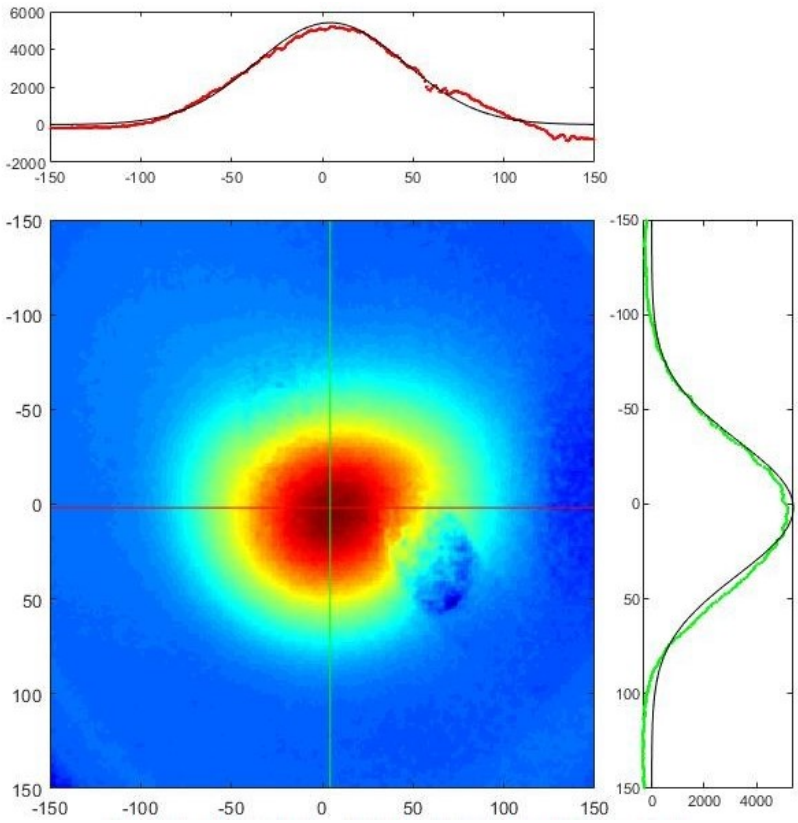

Figure 5.9: Picture of the atomic cloud as seen from the camera and relative fit using 2D Gaussian function [103].

The pictures were taken at the end of the sequence shown in fig. 5.8, but changing the time the camera and the blue light was triggered. In fig. 5.10 are the dimensions of the clouds at different TOF.

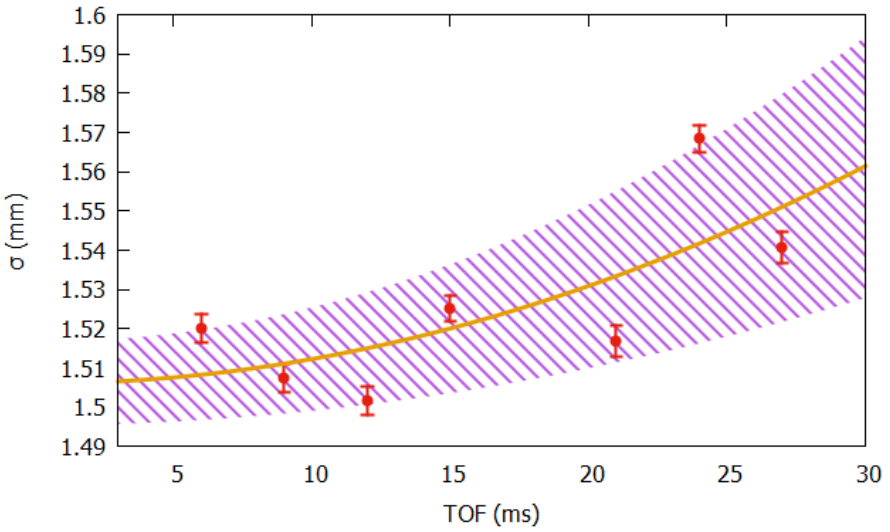

Figure 5.10: Dimensions of the atomic cloud at different TOF and fit of eq. 5.10.

The fit of eq. 5.10 with the data results in a temperature of $19 \pm 8\,\mu$K. Although the lattice that has been put in place to capture the atoms (1 W of power for 50 µm of waist) is deep enough to contain those atoms, the broadening due to inhomogeneous AC Stark effect (see ch. 2.5.5) is greater than the transition linewidth, so that it could mask long-range interaction effects. Higher control of the frequency of the 689 nm laser and a reduction of the power used in the single frequency could solve the problem.

5.5. Transfer of atoms in the $^3P_0$ state

To induce the long-range interaction in strontium, the atoms need to start from the $^3P_0$ state. This is a metastable state and it has a lifetime of several minutes. As a consequence, the linewidth of the transition between the $^3P_0$ and the $^1S_0$ state is extremely narrow. Therefore a very narrow and stable laser (clock laser) is required to transfer the atoms consistently into the $^3P_0$ state from the ground state and this makes this route impractical.

However the atoms in the $5s6s^3S_1$ decay into the $^3P_0$ with a probability of 12%[4]. This changes the problem from moving the atoms to the $^3P_0$ to moving

[4]Calculated as $\frac{\Gamma_{^3P_0}}{\Gamma_{^3P_0}+\Gamma_{^3P_1}+\Gamma_{^3P_2}}$

them to the $^3S_1$ state. Fortunately, this state is the same that is used to repump the atoms into the ground state during the first stage of cooling. It is possible to use 688 nm and 707 nm lasers during the second stage of cooling to transfer atoms from the $^3P_1$ state to the $^3P_0$. Since at this point the atoms are cold enough to be captured by the lattice they will be trapped.

To test the 688 nm laser, the blue MOT has been illuminated with the laser and the frequency of the laser is scanned over 3 GHz. At the transition frequency, the fluorescence of the MOT decreases, a sign that the atoms are moved to the $^3P_0$ state by the laser with a reduction in fluorescence of 84%. As further evidence, the loss of fluorescence was reduced to 74% when the 2.6 μm laser was turned on.

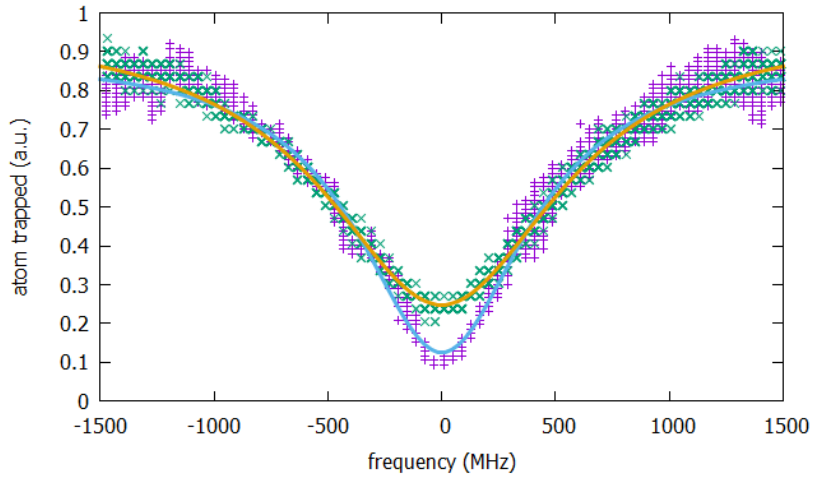

Figure 5.11: Fluorescence of the blue MOT at the change of the 688 nm laser frequency.

5.6. Preliminary measurement on the 2.6 μm transition

A crucial part of this experiment is to create a coherent excitation in the $^3D_1$ state using a 2.6 µm laser. However, this transition has not been extensively studied, and the data about it comes from theoretical calculation [79, 104] or indirect measurements [54]. Moreover, a characterisation of the linewidth of the laser is required to check its usability in this experiment.

The study of the transition starts by looking at the effect that the 2.6 μm laser has on the number of atoms in the blue MOT. In particular, the depen-

dency of the fluorescence of the MOT with the frequency of the 2.6 μm laser.

Since the MOT is a dynamic process, it requires time to find the equilibrium. Thus the change in frequency of the laser needs to be slower than the time that takes the MOT to reach equilibrium. It has been observed empirically that a change of less than 5 MHz/s does not distort the shape of the fluorescence peak.

To be able to change the frequency of the light sent to the atoms of a known amount, a modulation has been applied to the current of the laser. This modulation produces sidebands on the laser with distance from the carrier equal to the frequency of the modulation. Therefore scanning the frequency modulation, the sideband will be moved the same amount.

Fig. 5.12 has been taken by scanning the modulation frequency from 100 to 180 MHz and by recording the fluorescence of the blue MOT with a PMT.

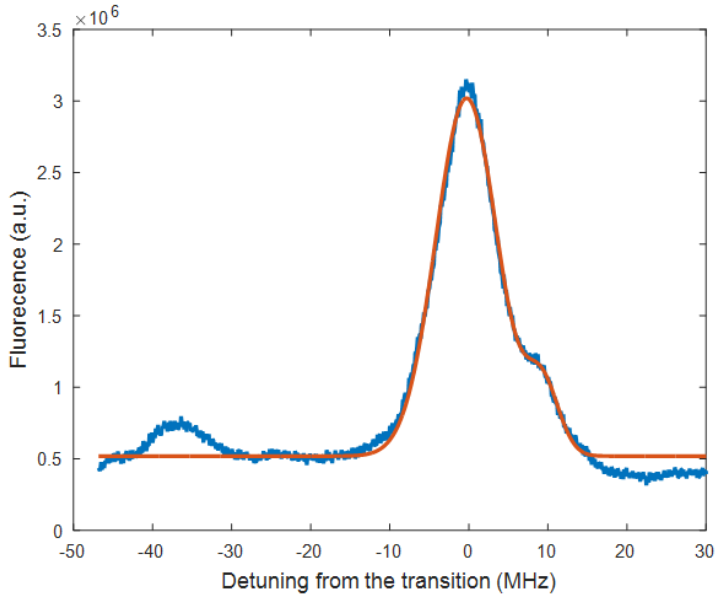

Figure 5.12: Fluorescence of the blue MOT at the change of the 2.6 µm sidebands.

The resulting peak has a linewidth of 4 MHz. This broadening of the transition is to be expected during the blue MOT phase, Doppler ($\Delta f = k \cdot \Delta v$), Zeeman ($\Delta f = \mu/\hbar \Delta B$) and power ($\Delta f = \Gamma\sqrt{1+s}$) are all contributing to the broadening of transition. Nevertheless, this measure puts an upper limit to the linewidth of the 2.6 µm laser to 4 MHz.

CHAPTER 6

Conclusions and outlook

In this thesis the progress that I made on the long range interaction experiment at the University of Birmingham, as of September 2018, has been presented. Key milestones achieved:

- Conducted the numerical study of several MOT geometries to cool Sr^{88}.
- Carried out the characterisation of a self-assembled Zeeman slower.
- Reviewed the theoretical framework for the realisation of the 1D optical lattice and set up the optics required to realise the 1D optical lattice.
- Cooled down 6×10^7 atoms of ^{88}Sr to a temperature of 19 µK.
- Proved that the 2.6 µm laser can indeed excite the atoms into the $^3D_1$ state and can be used as repump for the blue MOT.
- Showed that it is possible to pump the atoms into the $^3P_0$ state using the 688 nm laser.
- Presented a monolithic design for a IFECDL and measured its performance.

This thesis represents the starting point for the study of long-range interaction between Sr atoms with lower perturbation from external electric field and lower radiative decay compared with Rydberg atoms. The use of 2.6 µm laser

as repump for the first stage of cooling and the use of the $^3P_1 \rightarrow^3 S_1$ transition to load the atoms in the $^3P_0$ state will simplify the implementation of similar studies in the future, avoiding the need of an additional 679 nm laser and of an ultra-stable 698 nm one. The characterisation of the self-assembled Zeeman slower shows the effectiveness of the concept, making it a viable alternative to the more expensive options.

6.1. What next?

The next challenge for this experiment is to show the effect of the long-range interaction when the atoms are trapped in the 1D lattice. If the density is high enough it should be possible to measure the change in the Rabi frequency and transition frequency of the $^3P_0 \rightarrow {}^3D_1$ state. To perform these measurements, a better stabilisation of the 2.6 µm laser is required. The drift and linewidth of the laser need to be well below the linewidth of the transition. To reach this level of stability, the laser needs to be locked to a cavity. The cavity for this laser needs to have a frequency resolution in the order of 100 kHz and it has to be possible to tune the cavity length to bring the laser to the right frequency when locked. A cavity of this type is under construction at the time that this thesis is written. This cavity is based on a low drift etalon developed by the National Physical Laboratory[1]. With a drift lower than 500 kHz/hour, it will be possible to perform the experiment for several minutes before a recalibration using the atoms as a reference is required. The calibration can be performed by scanning the frequency of the laser using an AOM and monitor the atoms transferred into the upper state after a π-pulse. The schematic for the realisation of the locking system for the 2.6 µlaser is illustrated in fig. 6.1.

Once the measurements in the 1D lattice are completed, the realisation of a Mott insulator[28] will be attempted. This can be done by cooling the atoms further down using evaporative cooling, until the atoms reach the BEC state. Unfortunately, due to its negative elastic cross section, to make a BEC out of pure ^{88}Sr is not possible. Thus, instead of using the ^{88}Sr isotope, the ^{84}Sr isotope can be used in the experiment [105]. Alternatively, a sympathetic cooling of ^{88}Sr with ^{87}Sr is also a promising method to achieve BEC [106]. The trapping force for the evaporation will be provided by a 1064 nm fibre laser. Once the BEC is formed, the atoms will be trapped in a 3D blue detuned

[1] `http://www.npl.co.uk/science-technology/time-frequency/products-and-services/products-and-services/low-drift-etalons`

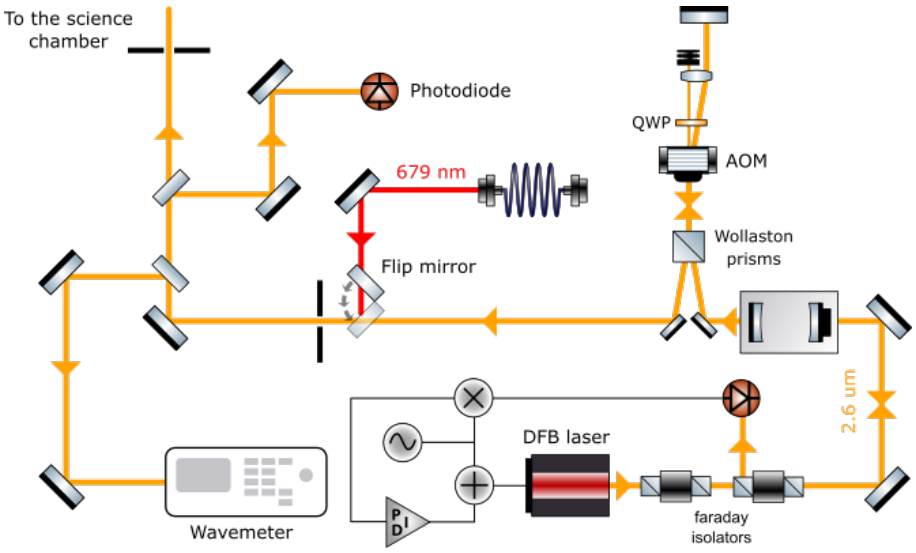

Figure 6.1: Schematic of the optical system to lock the 2.6 µm laser to the cavity.

optical lattice at 430 nm. At this point, the system will be used for the study of collective states with lifetime several order of magnitude longer than the one studied using to Rydberg atoms [107, 108] which has exciting applications in quantum information and photon storage.

APPENDIX A

MOT SIMULATION

In this chapter, the program which was developed to simulate the behaviour of atoms inside a MOT is represented.

The program is written in the C++ programming language. The simulation starts by reading the initial position and velocity of an atom given by the user. The program then calculates the forces that are acting on this atom, and use this information to calculate the new position and velocity of the atom.

The main flow of the program and how the each section of the program operates are described in section A.1 and, for reference, the complete code can be seen in section A.2. Through out this chapter, the notation (**L a:b**) is used to indicate lines numbers from point a to point b in the program as seen in section A.2.

A.1. INT MAIN

The workflow of the program is shown in fig. A.1 and below is the description of each workflow component.

A.1.1. Initialization of the environment

(**L 653:745**) The program starts by loading into memory the value of the complete elliptical integral of the first and second kind that are used in the

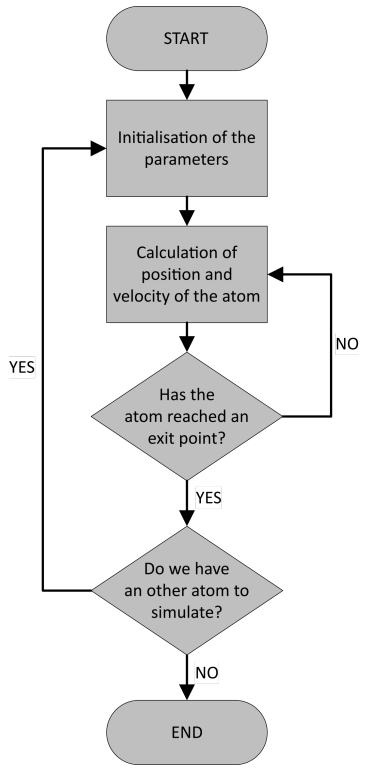

Figure A.1: Workflow of the simulation program.

calculation of the magnetic field. As well as initialising the input and output file used in the program to read and store data respectively.

(**L 747:749**) The program continues by setting relevant value of the transition, in the specific: $\alpha = h\pi\Gamma/\lambda$, Γ, μ, I_sat and $k_g = \lambda^{-1}\gamma^{-1}$ as defined in eq. 2.12. These parameter need to be defined by the user in the `enviroment.txt` file. At this moment the number of atoms simulated is defined as well.

(**L 750:826**) It proceeds by setting the number of laser beams and the relative P, w_0, f, Δ along with the direction vector, focusing point, direction, number of points used to determine the shape and the polarisation of the beam. For ring beam (number of points = 2) is sufficient to define its external and internal radius (set the internal radius to 0 for circular beam). For more complex geometry, further information is required: a list of points that define the vertices of the shape produced by the beam when projected on a plane, this plane will also determine the region of space where the beam starts (**L 190:315**). At the same moment, the program also generated a 'System Of Reference' (SOR) where the beam propagates along the z-axis. Then the program will generate the ending plane of the beam. For example, the sequence:

20 0.025 6.503e+14 -21e6 -1 0 0 0 0 -15 1 4 1
22.5 -7.5 7.5
7.5 -7.5 -7.5
7.5 7.5 -7.5
22.5 7.5 7.5
1 0 1
-15 0 0

will generate a square beam with side of 15 mm, with 20 mW of power, 25 mm beam waist, a frequency of 650.3 THz, detuning equal to 21 MHz, with $\vec{k} = (-1, 0, 0)$, focused on the point (0,0,-15) mm, with positive direction, it is formed by 4 points and with positive circular polarisation, the vertices of its shape are (22.5,-7.5,7.5),(7.5, -7.5, -7.5), (7.5, 7.5, -7.5) and (22.5, 7.5, 7.5) this beam will propagate until it meets the plane defined by the vector (1,0,1) and the point (-15,0,0). This example beam characterisation can be seen in fig.A.2.

(**L 750:826**) At this point, the program initialises the magnet and the coil along with their SOR, and an example initialisation sequence is shown below:

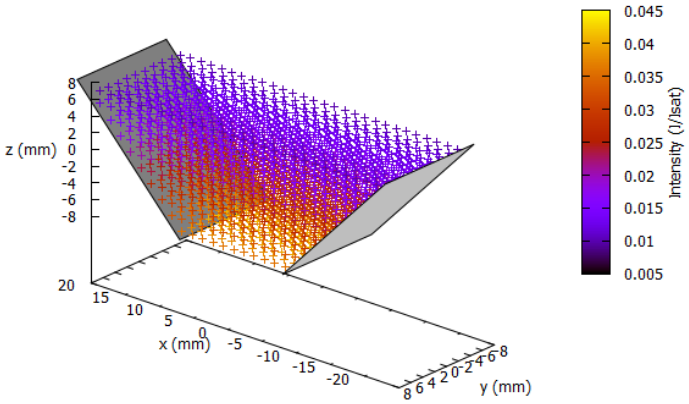

Figure A.2: Beam generate by the program.

2
0 0 1 0 0 0.015 330 0.030
0 0 1 0 0 -0.015 -330 0.030

This sequence will generate two coils that sit on xy plane at z=15 and z=-15 mm, they have $I * number\ of\ turns = \pm 330A$ and their radius is 30 mm (see figA.3).

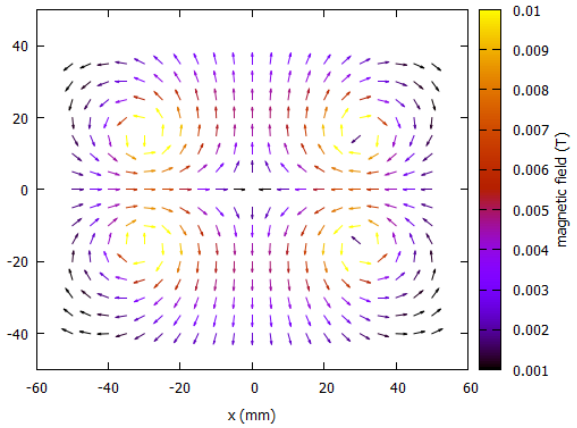

Figure A.3: Magnetic field calculated by the program.

A.1.2. Calculation of the trajectory

(**L 847:877**) In this section, the program initialises the variables needed for the simulation and reads from the file the number of atoms to simulate, their initial position, velocity and the probability to be found at that particular velocity and position.

(**L 880:906**) Now starting from $t = 0$ the forces acting on the atom are calculated. The position and velocity of the atom are updated assuming constant acceleration for $t = t_{res}$. This is repeated until any of the following conditions are met: the atom is captured by the MOT, the atom escape from the MOT completely or if $t > t_{end}$.

When the previous loop is complete, the program will check if other atoms are required to be simulated. If the response is positive, it will repeat the calculation with the new atom, otherwise, it will close the program.

In detail, to calculate the acceleration imposed by the laser on the atoms, the program will start by calculating the magnetic field present at the position where the atom is. It will do that considering each magnet and each coil separately and summing all the effects together. The first step to calculate the magnetic field generated by the magnet (**L 533:548**), this is transferred into the calculation in the SOR where the polarisation of the magnet corresponds to the z-axis, and then uses the equations:

$$
\begin{aligned}
B_x &= \frac{\mu m}{4\pi} 3 \frac{xz}{r^5}, \\
B_y &= \frac{\mu m}{4\pi} 3 \frac{yz}{r^5}, \\
B_z &= \frac{\mu m}{4\pi} 2 \frac{z^2 - y^2 - x^2}{r^5},
\end{aligned}
$$

to calculate the component of the magnetic field in the SOR of the magnet. It finishes translating this component in the SOR of the atom.

To calculate the magnetic field generated by the coil (**L 479:517**), we start as before by finding the position of the atom in the SOR of the coil; then it uses equation 2.15 and 2.16 to determine the components of the magnetic field. It ends transposing those components in the SOR of the atom.

Next the program will check which beams are hitting the atom being investigated. This is done by first making sure that the atom is in the region

of space defined by the plane of the mirror and the mirror end[1] (**L 355:362**). Using a ray cast algorithm the program checks if the projection of the position of the atom is along the direction of the beam and sits inside the region defined by the shape of the beam (**L 325:353**) (see fig. A.4).

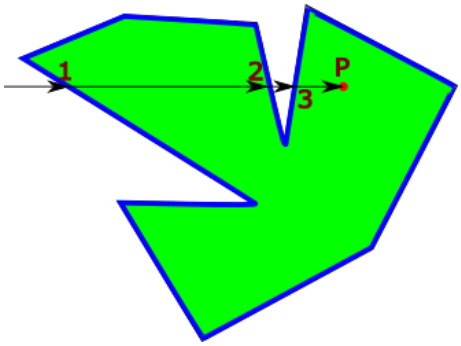

Figure A.4: To determine if a point P is or not inside a polygon, is sufficient to count the number of time a segment starting from outside the figure and ending on the point, cross the segment of the figure. If the count is odd, the point is inside the figure. If the count is even the point is outside it.

If the atom is inside the beam, the program will calculate the intensity (corrected for the detuning) of that beam at that point in space, and the total intensity seen by the atom (**L 443:459**).

At this point eq 2.12 is used to determine the acceleration imposed on the atom by each beam. With this information, the position and velocity are now changed by the following:

$$\vec{P} = \vec{P}_0 + \frac{1}{2}\vec{a}t^2, \tag{A.1}$$

$$\vec{V} = \vec{V}_0 + \vec{a}t. \tag{A.2}$$

Next, the program checks if the atom is exiting from the MOT region, this is determined by the exit option (**L 631:637**), or if it is captured by the MOT ($\vec{V} \approx 0$ and $\vec{P} \approx 0$). If neither of the previous condition are met, the program will calculate the acceleration at the new point and so on. If the cycle ends with the atom being captured, its initial velocity and position are saved, this can be used to calculate the capture velocity of the MOT, or the loading rate if the flux is known. Every 100 iteration the position and velocity of the atom is recorded in the file and can be used to plot the trajectory of the atom in the

[1] mirror end is the name of the plane where the beam end

MOT.

A.2. Full program

```
// Projection.cpp : simulation of a MOT
//

#include "stdafx.h"
#include <algorithm>
#include <cmath>
#include <iostream>
#include <fstream>
#include <vector>
#include <math.h>
#include <string>
#include <iomanip>
#include <chrono>
#include <ctime>
#include <thread>
#include <windows.h>
#include "MOTsim.h"


#define M_PI 3.14159265358979323846
#define H_plank 6.62606876e-34
#define MU_0 12.566370614e-7
#define M_0 1.66053873e-27
#define Ek sqrt(1-k*sin(pi)*sin(pi))
#define Kk 1.0/sqrt(1-k*sin(pi)*sin(pi))
#define STEP 0.001 //Step in the integration
#define C_l 299792458 //speed of light
double IKk[10001], IEk[10001];

using namespace std;
double p_pro[3];
double A[] = { 0,0,0 };
double B[] = { 0,0,0 };

//add tab as a command for iostream
namespace std {
 template <typename _CharT, typename _Traits>
 inline basic_ostream<_CharT, _Traits> &
  tab(basic_ostream<_CharT, _Traits> &__os) {
  return __os.put(__os.widen('\t'));
 }
```

```
42 }
43
44 //return in a,b and c the inverse of the matrix formed by AA, BB
       and CC
45 void inverse_matrix(double AA[3], double BB[3], double CC[3],
       double a[3], double b[3], double c[3])
46 {
47  double k[3][3];
48  double det;
49  det = AA[0] * BB[1] * CC[2] + AA[1] * BB[2] * CC[0] + AA[2] *
        BB[0] * CC[1] - CC[0] * BB[1] * AA[2] - CC[1] * BB[2] *
        AA[0] - CC[2] * BB[0] * AA[1];
50  a[0] = (BB[1] * CC[2] - BB[2] * CC[1]) / det;
51  a[1] = (AA[1] * CC[2] - AA[2] * CC[1]) / det;
52  a[2] = (AA[1] * BB[2] - AA[2] * BB[1]) / det;
53  b[0] = (BB[0] * CC[2] - BB[2] * CC[0]) / det;
54  b[1] = (AA[0] * CC[2] - AA[2] * CC[0]) / det;
55  b[2] = (AA[0] * BB[2] - AA[2] * BB[0]) / det;
56  c[0] = (BB[0] * CC[1] - BB[1] * CC[0]) / det;
57  c[1] = (AA[0] * CC[1] - AA[1] * CC[0]) / det;
58  c[2] = (AA[0] * BB[1] - AA[1] * BB[0]) / det;
59
60 }
61 //Calculate the Complete elliptic integral of the second kind for
       the calculation of the magnetic field
62 double Int_e(double k)
63 {
64  double sum = 0, pi, x;
65  for (pi = 0; pi <= M_PI / 2.0;)
66  {
67   x = Ek;
68   pi += STEP;
69   x += Ek;
70   sum += x*STEP / 2.0;
71  }
72  return sum;
73 }
74 //Calculate the Complete elliptic integral of the first kind for
       the calculation of the magnetic field
75 double Int_k(double k)
76 {
77  double sum = 0, pi, x;
78  for (pi = 0; pi <= M_PI / 2.0;)
79  {
80   x = Kk;
81   pi += STEP;
82   x += Kk;
```

```
83   sum += x*STEP / 2.0;
84  }
85  return sum;
86 }
87 //calculate the module of a 3D vector
88 double mod(double p[3])
89 {
90  double m = sqrt(p[0] * p[0] + p[1] * p[1] + p[2] * p[2]);
91  return m;
92 }
93 //Each atoms belongs to this class
94 class particle
95 {
96 public:
97  double p[3], v[3];
98  //initialisation options
99  particle() {};
100  void set_v(double a[3])
101  {
102   v[0] = a[0];
103   v[1] = a[1];
104   v[2] = a[2];
105  }
106  void set_p(double a[3])
107  {
108   p[0] = a[0];
109   p[1] = a[1];
110   p[2] = a[2];
111  }
112  //calculate the new position of an atom given a constant
       acceleration 'a' is applied for a time 't'
113  void upgrade(double a[3], double t)
114  {
115   p[0] += v[0] * t + 0.5*a[0] * t*t;
116   p[1] += v[1] * t + 0.5*a[1] * t*t;
117   p[2] += v[2] * t + 0.5*a[2] * t*t;
118   v[0] += a[0] * t;
119   v[1] += a[1] * t;
120   v[2] += a[2] * t;
121  }
122  //print in "output" position, velocity and acceleration of the
       atom
123  void print_pos(ofstream &output)
124  {
125   output << p[0] * 1000 << " " << p[1] * 1000 << " " << p[2] *
        1000 << " " << v[0] << " " << v[1] << " " << v[2] << " " <<
        A[0] << " " << A[1] << " " << A[2] << " " << mod(v) << endl;
```

```
126  }
127 };
128 //just used to keep some parameter
129 class transition
130 {
131 public:
132
133  double gamma;//decay rate [1/s]
134  double mu;//magnetic moment
135  double I_sat;//saturation intensity
136  double alpha;//h*pi*gamma/(m*wave_lenght)
137  double k_g;//wave_lenght^-1 gamma^-1
138
139  transition() {};
140
141 };
142 //scalar product of the vector p and q
143 double dot(double p[3], double q[3])
144 {
145  double m = p[0] * q[0] + p[1] * q[1] + p[2] * q[2];
146  return m;
147 }
148 //polygon class: used to define the boundary of a figure
149 class polygon {
150 public:
151  vector<double> Point[2];
152  double minx, miny, maxx, maxy;
153  int n_points;
154  polygon() {};
155
156  polygon(vector<double> k[2])
157  {
158   initio(k);
159  }
160  void initio(vector<double> k[2])
161  {
162   for (int i = 0; i < k[0].size(); i++)
163   {
164    Point[0].push_back(k[0][i]);
165    Point[1].push_back(k[1][i]);
166   }
167   minx = *std::min_element(Point[0].begin(), Point[0].end());
168   miny = *std::min_element(Point[1].begin(), Point[1].end());
169   maxx = *std::max_element(Point[0].begin(), Point[0].end());
170   maxy = *std::max_element(Point[1].begin(), Point[1].end());
171   n_points = k[0].size();
172  }
```

```
173  ~polygon() {  }
174  bool inside(double x[2]);
175 };
176 class Plane
177 {
178 public:
179  Plane() {};
180  double kx[3], ky[3], kz[3], o[3], Vec[4];
181  int side = 1;
182  Plane(double *v1, double p[3], int s)
183  {
184   initiov(v1, p, s);//initialization by vector, one point in the
          plane and one side
185  }
186  Plane(vector<double> p1[3], int s)
187  {
188   initiop(p1, s);//initialization by three point and one side
189  }
190  void initiov(double v1[3], double p[3], int s)
191  {
192   //build the system of reference of the plane
193   kz[0] = v1[0];
194   kz[1] = v1[1];
195   kz[2] = v1[2];
196
197   if (kz[2])
198   {
199    ky[0] = 0;
200    ky[1] = 1;
201    ky[2] = -(kz[1] / kz[2]);
202   }
203   else {
204    if (kz[1])
205    {
206     ky[0] = 1;
207     ky[1] = -(kz[0] / kz[1]);
208     ky[2] = 0;
209    }
210
211    else {
212     ky[0] = 0;
213     ky[1] = 1;
214     ky[2] = 0;
215    }
216   }
217   if (sqrt(dot(kz, ky)*dot(kz, ky)) > 1e-15)cout << "zy";
218
```

```
219   kx[0] = kz[1] * ky[2] - kz[2] * ky[1];
220   kx[1] = kz[2] * ky[0] - kz[0] * ky[2];
221   kx[2] = kz[0] * ky[1] - kz[1] * ky[0];
222
223   //normalize
224   double MOD = mod(kz);
225   if (MOD == 0)MOD = 1;
226   kz[0] = kz[0] / MOD;
227   kz[1] = kz[1] / MOD;
228   kz[2] = kz[2] / MOD;
229   MOD = mod(ky);
230   if (MOD == 0)MOD = 1;
231   ky[0] = ky[0] / MOD;
232   ky[1] = ky[1] / MOD;
233   ky[2] = ky[2] / MOD;
234   MOD = mod(kx);
235   if (MOD == 0)MOD = 1;
236   kx[0] = kx[0] / MOD;
237   kx[1] = kx[1] / MOD;
238   kx[2] = kx[2] / MOD;
239
240   o[0] = p[0];
241   o[1] = p[1];
242   o[2] = p[2];
243
244   side = s;
245
246   Vec[0] = v1[0];
247   Vec[1] = v1[1];
248   Vec[2] = v1[2];
249   Vec[3] = -(Vec[0] * p[0] + Vec[1] * p[1] + Vec[2] * p[2]);
250
251 }
252 void initiop(vector<double> p1[3], int s)
253 {
254  double u[3], v[3];
255
256   v[0] = p1[0][0] - p1[0][1];
257   v[1] = p1[1][0] - p1[1][1];
258   v[2] = p1[2][0] - p1[2][1];
259   u[0] = p1[0][0] - p1[0][2];
260   u[1] = p1[1][0] - p1[1][2];
261   u[2] = p1[2][0] - p1[2][2];
262   Vec[0] = v[1] * u[2] - v[2] * u[1];
263   Vec[1] = v[2] * u[0] - v[0] * u[2];
264   Vec[2] = v[0] * u[1] - v[1] * u[0];
265   Vec[3] = -(Vec[0] * p1[0][0] + Vec[1] * p1[1][0] + Vec[2] *
```

```
        p1[2][0]);
266   side = s;
267   //build the system of reference of the plane
268   kz[0] = Vec[0];
269   kz[1] = Vec[1];
270   kz[2] = Vec[2];
271   if (kz[2])
272   {
273    ky[0] = 0;
274    ky[1] = 1;
275    ky[2] = -(kz[1] / kz[2]);
276   }
277   else {
278    if (kz[1])
279    {
280     ky[0] = 1;
281     ky[1] = -(kz[0] / kz[1]);
282     ky[2] = 0;
283    }
284
285    else {
286     ky[0] = 0;
287     ky[1] = 1;
288     ky[2] = 0;
289    }
290   }
291   kx[0] = ky[1] * kz[2] - ky[2] * kz[1];
292   kx[1] = ky[2] * kz[0] - ky[0] * kz[2];
293   kx[2] = ky[0] * kz[1] - ky[1] * kz[0];
294   //normalize
295   double MOD = mod(kz);
296   kz[0] = kz[0] / MOD;
297   kz[1] = kz[1] / MOD;
298   kz[2] = kz[2] / MOD;
299   MOD = mod(ky);
300   ky[0] = ky[0] / MOD;
301   ky[1] = ky[1] / MOD;
302   ky[2] = ky[2] / MOD;
303   MOD = mod(kx);
304   kx[0] = kx[0] / MOD;
305   kx[1] = kx[1] / MOD;
306   kx[2] = kx[2] / MOD;
307
308
309   o[0] = p1[0][0];
310   o[1] = p1[1][0];
311   o[2] = p1[2][0];
```

```
312  }
313  bool Side(double x[3]);
314  ~Plane() {}
315 };
316 //project a point on the plane A
317 void projection(double p[3], Plane A)
318 {
319  double diff[]{ p[0] - A.o[0], p[1] - A.o[1], p[2] - A.o[2] };
320  p_pro[0] = dot(A.kx, diff);
321  p_pro[1] = dot(A.ky, diff);
322  p_pro[2] = dot(A.kz, diff);
323
324 }
325 //determine if a point on the plain is inside a polygon or not
        using the Ray casting algorithm
326 bool polygon::inside(double p[2])
327 {
328
329  int   i, j = n_points - 1;
330  bool  oddNodes = 0;
331  double x = p[0], y = p[1];
332
333  if (n_points<3)
334  {
335   double rag = sqrt((p[0] - Point[0][1]) * (p[0] - Point[0][1]) +
          (p[1] - Point[1][1]) * (p[1] - Point[1][1]));
336   if (rag >= Point[1][0] && rag <= Point[0][0])oddNodes = 1;
337  }
338  else
339  {
340   for (i = 0; i < n_points; i++)
341   {
342    if ((Point[1][i] < y && Point[1][j] >= y
343     || Point[1][j] < y && Point[1][i] >= y)
344     && (Point[0][i] <= x || Point[0][j] <= x))
345    {
346     oddNodes ^= (Point[0][i] + (y - Point[1][i]) / (Point[1][j] -
           Point[1][i])*(Point[0][j] - Point[0][i]) < x);
347    }
348    j = i;
349   }
350  }
351  return oddNodes;
352
353 }
354 //determine if a point is in the positive or negative side of a
        plane
```

```
355 bool Plane::Side(double x[3])
356 {
357  bool gg = 0;
358  float f = x[0] * Vec[0] + x[1] * Vec[1] + x[2] * Vec[2] + Vec[3];
359  f *= side;
360  if (f >= 0)gg = 1;
361  return gg;
362 }
363 /*this class contain the information about the laser beam:
364 shape: (as the name suggest) contain the information about the
        shape of the beam, is defined by the radius for circular beam
        or by the vertex position for other shape of beam
365 mirror: define the plane where the beam start
366 mirror_end: define the plane where the beam start
367 normal: define the plane normal to the direction of the beam
368 */
369 class Beam {
370 public:
371  polygon shape;//define the point then give the shape of the
         beam, is defined by the radius for circular beam or by the
         vertex position for other shape of beam
372  Plane mirror;//define the plane where the beam start
373  Plane mirror_end;//define the plane where the beam end
374  Plane normal;//plane normal at the k vector and system of
         reference
375  double P;//power of the beam
376  double z_r; // Rayleigh distance
377  double w_0; // waist size
378  double det_0; //detuning length respect the transition
379  double wavelenght;
380  int s; //polarization
381  double det[3], ki[3];
382
383  Beam() {}
384  void set_gaussan_parameter(double a, double b, double c, double
         d, int e)
385  {
386   P = a;
387   wavelenght = b;
388   w_0 = c;
389   det_0 = d;
390   s = e;
391
392   z_r = M_PI*w_0*wavelenght*1e-9;
393  }
394  //set the shape of the mirror using the point on the edge
395  void set_poly(vector<double> k[2])
```

```
396 {
397  shape.initio(k);
398 }
399 //set the plane normal to beam direction
400 void set_norm(double *v1, double p[3], int s)
401 {
402  normal.initiov(v1, p, s);
403 }
404 //set the plane from where the beam start using point or
        euclidean vector
405 void set_mirror(vector<double> p1[3], int s)
406 {
407  mirror.initiop(p1, s);
408 }
409 void set_mirror(double *v1, double p[3], int s)
410 {
411  mirror.initiov(v1, p, s);
412 }
413 //set the plane from where the beam end using euclidean vector
414 void set_mirror_end(double *v1, double p[3], int s)
415 {
416  mirror_end.initiov(v1, p, s);
417 }
418 //calculate effective detuning of the beam
419 void set_det(double V[3], transition tr, int n)
420 {
421  det[n + 1] = det_0 - dot(V, normal.kz)*tr.k_g - tr.mu*n*mod(B);
422 }
423 void set_ki(double ci)
424 {
425  ki[0] = pow(1 + s*ci, 2) / 4;
426  ki[1] = (1 - ci*ci) / 2;
427  ki[2] = pow(1 - s*ci, 2) / 4;
428 }
429 bool in_beam(double x[3]);//determine if a point is inside or
        not the beam
430 double intensity(double x[3]);//determine the intensity of the
        beam
431 double intensity_eff(double x[3], int n);//determine the
        effective intensity of the beam (used for the calculation of
        Itot)
432
433 };
434 //determine if the a point is inside the beam by projecting the
       point on the plan where the shape of the beam is
435 bool Beam::in_beam(double p[3])
436 {
```

```
437  projection(p, normal);
438  double x[] = { p_pro[0], p_pro[1] };
439
440  return (mirror.Side(p) && mirror_end.Side(p) && shape.inside(x));
441 }
442 //calculate the intensity of the beam at the point p
443 double Beam::intensity(double p[3])
444 {
445  double i, I_0, w, r, d;
446  d = sqrt((p[0] - normal.o[0])*(p[0] - normal.o[0]) + (p[1] -
        normal.o[1])*(p[1] - normal.o[1]) + (p[2] -
        normal.o[2])*(p[2] - normal.o[2]));
447  w = -tan(z_r / 2)*d + w_0;
448  projection(p, normal);
449  r = sqrt(p_pro[0] * p_pro[0] + p_pro[1] * p_pro[1]);
450  I_0 = P*2.0 / (M_PI*w*w);
451  i = I_0 *(w*w / w_0 / w_0)* exp(-2 * r*r / (w*w));
452  return i;
453 }
454 //correct the intensity considering the detuning
455 double Beam::intensity_eff(double p[3], int n)
456 {
457  double I_eff = intensity(p) * 1 / (1 + det[n + 1] * det[n + 1]);
458  return I_eff;
459 }
460 //in this class are defined the coils used the produce the
       magnetic field
461 class coil
462 {
463 public:
464  Plane norm;
465  double I, R;
466  double B_f[3];
467
468  coil() {};
469
470  void set_parameter(double v[3], double o[3], double i, double r)
471  {
472   norm.initiov(v, o, 1);
473   I = i;
474   R = r;
475  }
476  void fied_calculation(double x[3]);
477 };
478 //calculate the magnetic field using eq. 2.15 and 2.16.
479 void coil::fied_calculation(double x[3])
480 {
```

```
481  double b[3], br, ro, S1, S2, k, e_k, k_k;
482
483  projection(x, norm);
484  ro = sqrt(p_pro[0] * p_pro[0] + p_pro[1] * p_pro[1]);
485  S1 = (R + ro)*(R + ro) + p_pro[2] * p_pro[2];
486  S2 = (R - ro)*(R - ro) + p_pro[2] * p_pro[2];
487
488  if (ro <= 0.002)
489  {
490   k = (4.0*R * ro / S1);
491   k_k = Int_k(k);
492   e_k = Int_e(k);
493  }
494  else
495  {
496   k = floor(4 * R * ro / S1 * 10000);
497   k_k = IKk[(int)k];
498   e_k = IEk[(int)k];
499  }
500
501  b[2] = MU_0 * I / (2 * M_PI * sqrt(S1))*(k_k + (R*R - ro*ro -
         p_pro[2] * p_pro[2]) / S2*e_k);
502  if (ro == 0)
503  {
504   br = b[0] = b[1] = 0;
505  }
506  else
507  {
508   br = MU_0 * I * p_pro[2] / (2 * M_PI * sqrt(S1) * ro) * (-k_k +
          (R*R + ro*ro + p_pro[2] * p_pro[2]) / S2*e_k);
509   b[0] = br*p_pro[0] / ro;
510   b[1] = br*p_pro[1] / ro;
511  }
512
513  B_f[0] = b[0] * norm.kx[0] + b[1] * norm.ky[0] + b[2] *
         norm.kz[0];
514  B_f[1] = b[0] * norm.kx[1] + b[1] * norm.ky[1] + b[2] *
         norm.kz[1];
515  B_f[2] = b[0] * norm.kx[2] + b[1] * norm.ky[2] + b[2] *
         norm.kz[2];
516
517 }
518 //in this class are defined the magnets used the produce the
        magnetic field in the Zeeman slower
519 class magnet
520 {
521 public:
```

```
522  Plane norm;
523  double m;
524  double B_f[3];
525  magnet() {};
526  void set_parameter(double v[3], double o[3], double i)
527  {
528   norm.initiov(v, o, 1);
529   m = i;
530  }
531  void fied_calculation(double x[3]);
532 };
533 void magnet::fied_calculation(double x[3])
534 {
535  double b[3];
536
537  projection(x, norm);
538
539  //calculation of the magnetic field in system of reference of
         the magnet
540  b[0] = MU_0*m / (4 * M_PI)*(3 * p_pro[0] * p_pro[2]) /
         pow(mod(p_pro), 5);
541  b[1] = MU_0*m / (4 * M_PI)*(3 * p_pro[1] * p_pro[2]) /
         pow(mod(p_pro), 5);
542  b[2] = MU_0*m / (4 * M_PI)*(2 * p_pro[2] * p_pro[2] - p_pro[0] *
         p_pro[0] - p_pro[1] * p_pro[1]) / pow(mod(p_pro), 5);
543  //translation in the real SOR
544  B_f[0] = b[0] * norm.kx[0] + b[1] * norm.ky[0] + b[2] *
         norm.kz[0];
545  B_f[1] = b[0] * norm.kx[1] + b[1] * norm.ky[1] + b[2] *
         norm.kz[1];
546  B_f[2] = b[0] * norm.kx[2] + b[1] * norm.ky[2] + b[2] *
         norm.kz[2];
547
548 }
549 //go through all the coil and all the magnet to calculate the
       magnetic field
550 void magnetic_field_calculation(double p[3], magnet *m, int n_m,
       coil *c, int n_c)
551 {
552  B[0] = B[1] = B[2] = 0;
553  int i;
554
555  for (i = 0; i < n_m; i++)
556  {
557   m[i].fied_calculation(p);
558   B[0] += m[i].B_f[0];
559   B[1] += m[i].B_f[1];
```

```
560   B[2] += m[i].B_f[2];
561  }
562
563  for (i = 0; i < n_c; i++)
564  {
565   c[i].fied_calculation(p);
566   B[0] += c[i].B_f[0];
567   B[1] += c[i].B_f[1];
568   B[2] += c[i].B_f[2];
569  }
570 }
571 //calculate the acceleration caused by the light using eq. 2.12
572 void Acceleration(double p[3], double V[3], Beam *beam, int
        n_beams, transition tr, magnet *m, int n_m, coil *c, int n_c)
573 {
574  double I_total[] = { 0,0,0 };
575  double ci = 0, a = 0;
576  int n;
577  double I_TOTAL = 0;
578  A[0] = A[1] = A[2] = 0;
579  magnetic_field_calculation(p, m, n_m, c, n_c);
580  int i;
581  for (i = 0; i < n_beams; i++)
582   //i = 4;
583
584  {
585
586   if (!beam[i].in_beam(p))continue;
587   if (mod(B) < 1e-15) ci = 0;
588   else
589    ci = dot(beam[i].normal.kz, B) / mod(B);
590
591   beam[i].set_ki(ci);
592   for (n = -1; n <= 1; n++)
593   {
594    beam[i].set_det(V, tr, n);
595    I_total[n + 1] += beam[i].intensity_eff(p, n) / tr.I_sat;
596
597   }
598   I_TOTAL += I_total[0] * beam[i].ki[0] + I_total[1] *
          beam[i].ki[0] + I_total[2] * beam[i].ki[0];
599  }
600
601  for (int i = 0; i < n_beams; i++)
602  {
603   double bla;
604   if (!beam[i].in_beam(p))continue;
```

```
605   for (n = -1; n <= 1; n++)
606   {
607
608    a += tr.alpha*beam[i].intensity(p) / tr.I_sat * beam[i].ki[n +
          1] / (1.0 + I_TOTAL + 4.0 * beam[i].det[n + 1] *
          beam[i].det[n + 1]);
609    bla = beam[i].intensity(p);
610   }
611   A[0] += a*beam[i].normal.kz[0];
612   A[1] += a*beam[i].normal.kz[1];
613   A[2] += a*beam[i].normal.kz[2];
614   a = 0;
615  }
616 }
617
618 //check if the atom "isbeind" the mirror
619 bool insidemirror(double p[3], Beam *beam, int n)
620 {
621  bool gg;
622  for (int i = 0; i < n; i++)
623  {
624   projection(p, beam[i].normal);
625   double x[] = { p_pro[0], p_pro[1] };
626   return (!beam[i].mirror.Side(p) && beam[i].shape.inside(x));
627
628  }
629 }
630 //determine when the simulation end
631 bool brake_option(double p[3], Beam *beams, int n, int o)
632 {
633  bool gg = 0;
634  if (mod(p)>0.05) gg = 1, o = 1;
635  //if (inside mirror(p, beams, n)) gg = 1, o = 2;
636  return gg;
637 }
638 //display error message
639 int DisplayResourceNAMessageBox(LPCWSTR a, LPCWSTR b)
640 {
641  MessageBox(
642   NULL,
643   a,
644   b,
645   MB_ICONWARNING
646  );
647
648  return 0;
649 }
```

```
650
651
652 int main()
653 {
654
655  const clock_t begin_time = clock();
656
657  //input file
658  ifstream input("beamFile.txt");//This file contain the
        information about the beam
659  if (!input.is_open())
660  {
661   DisplayResourceNAMessageBox((LPCWSTR)L"beamFile.txt not found
         \n The program will be terminate", (LPCWSTR)L"File not
         found");
662   return 1;
663  }
664  ifstream env("enviroment.txt");//This file contain the
        information about the transition and the starting position
        of the atoms
665  if (!env.is_open())
666  {
667   DisplayResourceNAMessageBox((LPCWSTR)L"enviroment.txt not found
         \n The program will be terminate", (LPCWSTR)L"File not
         found");
668   return 1;
669  }
670  ifstream coil_file("coil.txt");//information about the coil
671  if (!coil_file.is_open())
672  {
673   DisplayResourceNAMessageBox((LPCWSTR)L"coil_file.txt not found
         \n The program will be terminate", (LPCWSTR)L"File not
         found");
674   return 1;
675  }
676  ifstream magnet_file("magnet.txt");//information about the magnet
677  if (!magnet_file.is_open())
678  {
679   DisplayResourceNAMessageBox((LPCWSTR)L"magnet_file.txt not
         found \n The program will be terminate", (LPCWSTR)L"File
         not found");
680   return 1;
681  }
682  ifstream intege("ek_integral.bin", ios::in |
        ios::binary);//table with the value of the complete
        elliptical integral of second kind for the calculation of
        the magnetic field. If the file doesn't not exist, the
```

```
        program will crate it
683  if (!intege.is_open())
684  {
685   ofstream integE("ek_integral.bin", ios::out | ios::binary);
686   for (float i = 0; i <= 1; i += 1.0 / 10000)
687   {
688    double s = Int_e(i);
689    integE.write((char*)&s,sizeof(double));
690   }
691   intege.open("ek_integral.bin", ios::in | ios::binary);
692  }
693  ifstream integk("kk_integral.bin", ios::in | ios::binary);//as
        previews one but for the complete elliptical integral of the
        first type
694  if (!integk.is_open())
695  {
696   ofstream integK("kk_integral.bin", ios::out | ios::binary);
697   for (float i = 0; i <= 1; i += 1.0 / 10000)
698   {
699    double s = Int_k(i);
700    integK.write((char*)&s, sizeof(double));
701   }
702   integk.open("kk_integral.bin", ios::in | ios::binary);
703
704  }
705
706  //load in memory the complete elliptical integral value for fast
        access
707
708  for (int i = 0; i <= 10000; i++)
709  {
710   intege.read((char*)&IEk[i], sizeof(double));
711   integk.read((char*)&IKk[i], sizeof(double));
712  }
713  intege.close();
714  integk.close();
715
716  double point[]{ 1,1,1 }, k[]{ 0,0,1 }, o[]{ 0,0,0 }, p[3],
        xxx[2], p2[] = { 0,0,0 };
717  int n_beams, n_magnets, n_coils;
718  double t_res, t_end;//time resolution and ending time [s]
719  string trajectory_file;
720  vector<double> Point2D[2];
721  vector<double> Point3D[3];
722  Beam *beam;
723  coil *Coil;
724  magnet *Magnet;
```

```
725  particle atom;
726  transition tr;
727  int ddd, n_point, direction, polarization;
728  double power, q_parameter, waiste, frequency;
729  int exit_state = 0;
730  int n_part;
731
732  //environment setup and output file
733
734  ofstream output("zero_v.txt");
735  ofstream output2("magnetic.txt");
736  ofstream gnup("mirror_shape.txt");
737  getline(env, trajectory_file);
738  ofstream trajectory(trajectory_file/*, ios::app*/);
739  getline(env, trajectory_file);
740  ofstream synthesis(trajectory_file/* , ios::app*/);
741  env >> t_res >> t_end;
742  ofstream omin("trajectory3.txt" /*,  ios::app*/);
743  ofstream diff("diff.txt" /*,  ios::app*/);
744  ofstream avr("average.txt" /*,  ios::app*/);
745  //transition setup
746
747  env >> tr.alpha >> tr.gamma >> tr.mu >> tr.I_sat >> tr.k_g;
748
749  env >> n_part;
750  //start to set up all the beam defined in "beamFile.txt"
751  input >> n_beams;
752  beam = new Beam[n_beams];
753
754  for (int i = 0; i < n_beams; i++)
755  {
756   double detu;
757   input >> power >> waiste >> frequency >> detu >> k[0] >> k[1]
         >> k[2] >> o[0] >> o[1] >> o[2] >> direction >> n_point >>
         polarization;
758   double lamb = frequency / C_l;
759
760   detu = detu / tr.gamma;
761
762   //convert mm in m
763   o[0] *= 0.001;
764   o[1] *= 0.001;
765   o[2] *= 0.001;
766   beam[i].set_gaussan_parameter(power, lamb, waiste, detu,
         polarization);
767   beam[i].set_norm(k, o, direction);
768   //start to build the contour of the beam
```

```
769   gnup << "set object " << i + 1 << " polygon from ";
770   if (n_point <= 2)//circular beam
771   {
772    input >> point[0] >> point[1];
773    Point2D[0].push_back(point[0] / 1000);
774    Point2D[1].push_back(point[1] / 1000);
775    input >> point[0] >> point[1] >> point[2];
776    projection(point, beam[i].normal);
777    Point2D[0].push_back(p_pro[0] / 1000);
778    Point2D[1].push_back(p_pro[1] / 1000);
779   }
780   else
781   {
782    for (ddd = 0; ddd < n_point; ddd++)
783    {
784     input >> point[0] >> point[1] >> point[2];
785     point[0] *= 0.001;
786     point[1] *= 0.001;
787     point[2] *= 0.001;
788     gnup << point[0]*1000 << ", " << point[1]*1000 << ", " <<
          point[2]*1000 << " to ";
789     Point3D[0].push_back(point[0]);
790     Point3D[1].push_back(point[1]);
791     Point3D[2].push_back(point[2]);
792
793     projection(point, beam[i].normal);
794     Point2D[0].push_back(p_pro[0]);
795     Point2D[1].push_back(p_pro[1]);
796
797    }
798    gnup << Point3D[0][0] * 1000 << ", " << Point3D[1][0] * 1000
         << ", " << Point3D[2][0] * 1000 << endl;
799    gnup << "set object " << i + 1 << " fillstyle transparent
         solid 0.5 splot 1 / 0 notitle " << endl;
800   }
801
802   beam[i].set_poly(Point2D);
803   if (n_point <= 2)
804   {
805    input >> o[0] >> o[1] >> o[2];
806    beam[i].set_mirror(o, point, -direction);
807   }
808   else
809   {
810    beam[i].set_mirror(Point3D, -direction);
811    input >> o[0] >> o[1] >> o[2];
812   }
```

```
813
814   input >> point[0] >> point[1] >> point[2];
815   point[0] *= 0.001;
816   point[1] *= 0.001;
817   point[2] *= 0.001;
818   beam[i].set_mirror_end(o, point, direction);
819
820   //erase the vector
821   Point2D[0].erase(Point2D[0].begin(), Point2D[0].end());
822   Point2D[1].erase(Point2D[1].begin(), Point2D[1].end());
823   Point3D[0].erase(Point3D[0].begin(), Point3D[0].end());
824   Point3D[1].erase(Point3D[1].begin(), Point3D[1].end());
825   Point3D[2].erase(Point3D[2].begin(), Point3D[2].end());
826  }
827
828  //magnetic field setup
829  double m, current, radius;
830
831  magnet_file >> n_magnets;
832  Magnet = new magnet[n_magnets];
833  for (int i = 0; i < n_magnets; i++)
834  {
835   magnet_file >> k[0] >> k[1] >> k[2] >> o[0] >> o[1] >> o[2] >>
          m;
836   Magnet[i].set_parameter(k, o, m);
837  }
838
839  coil_file >> n_coils;
840  Coil = new coil[n_coils];
841  for (int i = 0; i < n_coils; i++)
842  {
843   coil_file >> k[0] >> k[1] >> k[2] >> o[0] >> o[1] >> o[2] >>
          current >> radius;
844   Coil[i].set_parameter(k, o, current, radius);
845  }
846
847  //trajectory calculation
848  int t;
849  int dummy;
850  double fi = 0 * 3.14159265358979323846 / -6.0, theta = 0, v;
851  int in;
852  double v_max = 0;
853  double v_min = 0;
854  double n_pass = 289;
855  bool inside = 0;
856  double probability;
857  double count = 0;
```

```
858 //take one particle at the time and calculate the trajectory for
        each of them
859
860 for (int ss = 0; ss < n_part; ss++)
861 {
862  int ccc = 0;
863  if (!(ss % 10))cout << "\r" << double(ss) / double(n_part) *
         100;
864
865  env >> atom.p[0] >> atom.p[1] >> atom.p[2] >> atom.v[0] >>
         atom.v[1] >> atom.v[2] >> probability;
866  double P_0[] = { atom.p[0] , atom.p[1] , atom.p[2] };
867  double V_0[] = { atom.v[0],atom.v[1],atom.v[2] };
868
869
870
871  v_max = 0;
872  v_min = 0;
873
874  A[0] = A[1] = A[2] = 0;
875  in = 0;
876  exit_state = 0;
877  inside = false;
878
879
880  for (t = 0; t <= (t_end / t_res); t++)
881  {
882   //calculate the value of the acceleration and store the value
         in the global variable A
883   Acceleration(atom.p, atom.v, beam, n_beams, tr, Magnet,
         n_magnets, Coil, n_coils);
884
885   atom.upgrade(A, t_res);
886
887   //write the actual position and velocity of the atom in the
         file define in "enviroment.txt"
888   if (!(t % 10)) trajectory << atom.p[0]*1000 << " " <<
         atom.p[1]*1000 << " " << atom.p[2]*1000 << " " <<
         atom.v[0] << " " << atom.v[1] << " " << atom.v[2] << tab
         << mod(atom.v) << endl;
889
890   if (brake_option(atom.p, beam, n_beams, exit_state))
891   {
892    break;
893   }
894
895   //interrupt the calculation if the atom is captured
```

```
896     if (floor(atom.p[0]) < 0.003 && floor(atom.p[1]) < 0.003 &&
            floor(atom.p[2] - 0.01) < 0.003 && (mod(atom.v) < 0.1))
897     {
898      exit_state = 1;
899      count += probability;
900      break;
901     }
902
903    }
904    if(exit_state)
905
906  }
907
908  env.close();
909  trajectory.close();
910  synthesis.close();
911  input.close();
912  output.close();
913  output2.close();
914  omin.close();
915  coil_file.close();
916  magnet_file.close();
917  avr.close();
918  diff.close();
919  delete[] beam;
920  cout << '\a';
921
922  return 0;}
```

Bibliography

[1] I. Bloch, J. Dalibard, and W. Zwerger, "Many-body physics with ultracold gases," *Rev. Mod. Phys.*, vol. 80, pp. 885–964, 3 Jul. 2008. [Online]. Available: https://link.aps.org/doi/10.1103/RevModPhys.80.885.

[2] M. Lewenstein, A. Sanpera, V. Ahufinger, B. Damski, A. Sen(De), and U. Sen, "Ultracold atomic gases in optical lattices: Mimicking condensed matter physics and beyond," *Advances in Physics*, vol. 56, no. 2, pp. 243–379, 2007. eprint: https://doi.org/10.1080/00018730701223200. [Online]. Available: https://doi.org/10.1080/00018730701223200.

[3] L. Isenhower, E. Urban, X. L. Zhang, A. T. Gill, T. Henage, T. A. Johnson, T. G. Walker, and M. Saffman, "Demonstration of a neutral atom controlled-not quantum gate," *Phys. Rev. Lett.*, vol. 104, p. 010 503, 1 2010. [Online]. Available: https://link.aps.org/doi/10.1103/PhysRevLett.104.010503.

[4] E. Urban, T. A. Johnson, T. Henage, L. Isenhower, D. D. Yavuz, T. G. Walker, and M. Saffman, "Observation of rydberg blockade between two atoms," *Nature Physics*, vol. 5, 110—114, 2009. [Online]. Available: https://www.nature.com/articles/nphys1178.

[5] A. Gaëtan, Y. Miroshnychenko, T. Wilk, A. Chotia, M. Viteau, D. Comparat, P. Pillet, A. Browaeys, and P. Grangier, "Observation of collective excitation of two individual atoms in the rydberg blockade regime," *Nature Physics*, vol. 5, 115—118, 2009. [Online]. Available: https://www.nature.com/articles/nphys1183#article-info.

[6] A. Griesmaier, J. Werner, S. Hensler, J. Stuhler, and T. Pfau, "Bose-einstein condensation of chromium," *Phys. Rev. Lett.*, vol. 94, p. 160 401, 16 Apr. 2005. [Online]. Available: https://link.aps.org/doi/10.1103/PhysRevLett.94.160401.

[7] J. L. Bohn, A. M. Rey, and J. Ye, "Cold molecules: Progress in quantum engineering of chemistry and quantum matter," *Science*, vol. 357, no. 6355, pp. 1002–1010, 2017, ISSN: 0036-8075. eprint: http://science.sciencemag.org/content/357/6355/1002.full.pdf. [Online]. Available: http://science.sciencemag.org/content/357/6355/1002.

[8] D. Comparat and P. Pillet, "Dipole blockade in a cold rydberg atomic sample," *J. Opt. Soc. Am. B*, vol. 27, no. 6, A208–A232, 2010. [Online]. Available: http://josab.osa.org/abstract.cfm?URI=josab-27-6-A208.

[9] M. Marinescu and L. You, "Controlling atom-atom interaction at ultralow temperatures by dc electric fields," *Phys. Rev. Lett.*, vol. 81, pp. 4596–4599, 21 1998. [Online]. Available: https://link.aps.org/doi/10.1103/PhysRevLett.81.4596.

[10] S. Yi and L. You, "Trapped condensates of atoms with dipole interactions," *Phys. Rev. A*, vol. 63, p. 053 607, 5 2001. [Online]. Available: https://link.aps.org/doi/10.1103/PhysRevA.63.053607.

[11] R. Löw, R. Gati, J. Stuhler, and T. Pfau, "Probing the light-induced dipole-dipole interaction in momentum space," *EPL (Europhysics Letters)*, vol. 71, no. 2, p. 214, 2005. [Online]. Available: http://stacks.iop.org/0295-5075/71/i=2/a=214.

[12] B. Olmos, D. Yu, Y. Singh, F. Schreck, K. Bongs, and I. Lesanovsky, "Long-range interacting many-body systems with alkaline-earth-metal atoms," *Phys. Rev. Lett.*, vol. 110, p. 143 602, 14 2013. [Online]. Available: https://link.aps.org/doi/10.1103/PhysRevLett.110.143602.

[13] T. Hänsch and A. Schawlow, "Cooling of gases by laser radiation," *Optics Communications*, vol. 13, no. 1, pp. 68 –69, 1975, ISSN: 0030-4018. [Online]. Available: http://www.sciencedirect.com/science/article/pii/0030401875901595.

[14] D. J. Wineland, R. E. Drullinger, and F. L. Walls, "Radiation-pressure cooling of bound resonant absorbers," *Phys. Rev. Lett.*, vol. 40, pp. 1639–1642, 25 1978. [Online]. Available: https://link.aps.org/doi/10.1103/PhysRevLett.40.1639.

[15] W. D. Phillips and H. Metcalf, "Laser deceleration of an atomic beam," *Phys. Rev. Lett.*, vol. 48, pp. 596–599, 9 Mar. 1982. [Online]. Available: https://link.aps.org/doi/10.1103/PhysRevLett.48.596.

[16] S. Chu, J. E. Bjorkholm, A. Ashkin, and A. Cable, "Experimental observation of optically trapped atoms," *Phys. Rev. Lett.*, vol. 57, pp. 314–317, 3 Jul. 1986. [Online]. Available: https://link.aps.org/doi/10.1103/PhysRevLett.57.314.

[17] E. L. Raab, M. Prentiss, A. Cable, S. Chu, and D. E. Pritchard, "Trapping of neutral sodium atoms with radiation pressure," *Phys. Rev. Lett.*, vol. 59, pp. 2631–2634, 23 Dec. 1987. [Online]. Available: https://link.aps.org/doi/10.1103/PhysRevLett.59.2631.

[18] The Royal Swedish Academy of Sciences, *1997 nobel prize in physics*, URL: https://www.nobelprize.org/prizes/physics/1997/press-release/, 1997.

[19] T. F. Gallagher, *Rydberg Atoms*, ser. Cambridge Monographs on Atomic, Molecular and Chemical Physics. Cambridge University Press, 1994.

[20] M. H. Anderson, J. R. Ensher, M. R. Matthews, C. E. Wieman, and E. A. Cornell, "Observation of bose-einstein condensation in a dilute atomic vapor," *Science*, vol. 269, no. 5221, pp. 198–201, 1995, ISSN: 0036-8075. eprint: `http://science.sciencemag.org/content/269/5221/198.full.pdf`. [Online]. Available: `http://science.sciencemag.org/content/269/5221/198`.

[21] T. Lahaye, C. Menotti, L. Santos, M. Lewenstein, and T. Pfau, "The physics of dipolar bosonic quantum gases," *Reports on Progress in Physics*, vol. 72, no. 12, p. 126 401, 2009. [Online]. Available: `http://stacks.iop.org/0034-4885/72/i=12/a=126401`.

[22] J. D. Weinstein, R. deCarvalho, T. Guillet, B. Friedrich, and J. M. Doyle, "Magnetic trapping of calcium monohydride molecules at millikelvin temperatures," *Nature*, vol. 395, pp. 148–150, Dec. 1998.

[23] W. R. Anderson, J. R. Veale, and T. F. Gallagher, "Resonant dipole-dipole energy transfer in a nearly frozen rydberg gas," *Phys. Rev. Lett.*, vol. 80, pp. 249–252, 2 1998. [Online]. Available: `https://link.aps.org/doi/10.1103/PhysRevLett.80.249`.

[24] I. Mourachko, D. Comparat, F. de Tomasi, A. Fioretti, P. Nosbaum, V. M. Akulin, and P. Pillet, "Many-body effects in a frozen rydberg gas," *Phys. Rev. Lett.*, vol. 80, pp. 253–256, 2 1998. [Online]. Available: `https://link.aps.org/doi/10.1103/PhysRevLett.80.253`.

[25] B. DeMarco and D. S. Jin, "Onset of fermi degeneracy in a trapped atomic gas," *Science*, vol. 285, no. 5434, pp. 1703–1706, 1999, ISSN: 0036-8075. eprint: `http://science.sciencemag.org/content/285/5434/1703.full.pdf`. [Online]. Available: `http://science.sciencemag.org/content/285/5434/1703`.

[26] M. D. Lukin, M. Fleischhauer, R. Cote, L. M. Duan, D. Jaksch, J. I. Cirac, and P. Zoller, "Dipole blockade and quantum information processing in mesoscopic atomic ensembles," *Phys. Rev. Lett.*, vol. 87, p. 037 901, 3 2001. [Online]. Available: `https://link.aps.org/doi/10.1103/PhysRevLett.87.037901`.

[27] A. Gaëtan, Y. Miroshnychenko, T. Wilk, A. Chotia, M. Viteau, D. Comparat, P. Pillet, A. Browaeys, and P. Grangier, "Observation of collective excitation of two individual atoms in the rydberg blockade regime," *Nature Physics*, vol. 5, pp. 115–118, 2009.

[28] M. Greiner, O. Mandel, T. Esslinger, T. W. Hänsch, and I. Bloch, "Quantum phase transition from a superfluid to a mott insulator in a gas of ultracold atoms," *Nature*, vol. 395, pp. 148–150, Dec. 1998.

[29] S. Inouye, J. Goldwin, M. L. Olsen, C. Ticknor, J. L. Bohn, and D. S. Jin, "Observation of heteronuclear feshbach resonances in a mixture of bosons and fermions," *Phys. Rev. Lett.*, vol. 93, p. 183 201, 18 2004. [Online]. Available: `https://link.aps.org/doi/10.1103/PhysRevLett.93.183201`.

[30] D. Wang, J. Qi, M. F. Stone, O. Nikolayeva, H. Wang, B. Hattaway, S. D. Gensemer, P. L. Gould, E. E. Eyler, and W. C. Stwalley, "Photoassociative production and trapping of ultracold KRb molecules," *Phys. Rev. Lett.*, vol. 93, p. 243 005, 24 2004. [Online]. Available: `https://link.aps.org/doi/10.1103/PhysRevLett.93.243005`.

[31] K. R. Overstreet, A. Schwettmann, J. Tallant, D. Booth, and J. P. Shaffer, "Observation of electric-field-induced Cs rydberg atom macrodimers," *Nature Physics*, vol. 5, pp. 581–585, 2009.

[32] H. Saßmannshausen and J. Deiglmayr, "Observation of rydberg-atom macrodimers: Micrometer-sized diatomic molecules," *Phys. Rev. Lett.*, vol. 117, p. 083 401, 8 2016. [Online]. Available: `https://link.aps.org/doi/10.1103/PhysRevLett.117.083401`.

[33] J. F. Sherson, C. Weitenberg, M. Endres, M. Cheneau, I. Bloch, and S. Kuhr, "Single-atom-resolved fluorescence imaging of an atomic mott insulator," *Nature*, vol. 467, pp. 68–70, 2010.

[34] J. Struck, C. Ölschläger, R. Le Targat, P. Soltan-Panahi, A. Eckardt, M. Lewenstein, P. Windpassinger, and K. Sengstock, "Quantum simulation of frustrated classical magnetism in triangular optical lattices," *Science*, vol. 333, no. 6045, pp. 996–999, 2011, ISSN: 0036-8075. eprint: `http://science.sciencemag.org/content/333/6045/996.full.pdf`. [Online]. Available: `http://science.sciencemag.org/content/333/6045/996`.

[35] J. S. Douglas, H. Habibian, C.-L. Hung, A. V. Gorshkov, H. J. Kimble, and D. E. Chang, "Quantum many-body models with cold atoms coupled to photonic crystals," *Nature photonics*, vol. 9, pp. 326–331, 2015.

[36] A. González-Tudela, C.-L. Hung, D. E. Chang, J. I. Cirac, and H. J. Kimble, "Subwavelength vacuum lattices and atom–atom interactions in two-dimensional photonic crystals," *Nature photonics*, vol. 9, pp. 320–325, 2015.

[37] M. Bellouvet, C. Busquet, J. Zhang, P. Lalanne, P. Bouyer, and S. Bernon, "Doubly dressed states for near-field trapping and subwavelength lattice structuring," *Phys. Rev. A*, vol. 98, p. 023 429, 2 2018. [Online]. Available: `https://link.aps.org/doi/10.1103/PhysRevA.98.023429`.

[38] W. Guerin, M. O. Araújo, and R. Kaiser, "Subradiance in a large cloud of cold atoms," *Phys. Rev. Lett.*, vol. 116, p. 083 601, 8 2016. [Online]. Available: `https://link.aps.org/doi/10.1103/PhysRevLett.116.083601`.

[39] T. L. Nguyen, J. M. Raimond, C. Sayrin, R. Cortiñas, T. Cantat-Moltrecht, F. Assemat, I. Dotsenko, S. Gleyzes, S. Haroche, G. Roux, T. Jolicoeur, and M. Brune, "Towards quantum simulation with circular rydberg atoms," *Phys. Rev. X*, vol. 8, p. 011 032, 1 2018. [Online]. Available: `https://link.aps.org/doi/10.1103/PhysRevX.8.011032`.

[40] L. Pezzè, A. Smerzi, M. K. Oberthaler, R. Schmied, and P. Treutlein, "Quantum metrology with nonclassical states of atomic ensembles," *Rev. Mod. Phys.*, vol. 90, p. 035 005, 3 2018. [Online]. Available: `https://link.aps.org/doi/10.1103/RevModPhys.90.035005`.

[41] R. Sawant, O. Dulieu, and S. A. Rangwala, "Detection of ultracold molecules using an optical cavity," *Phys. Rev. A*, vol. 97, p. 063 405, 6 2018. [Online]. Available: `https://link.aps.org/doi/10.1103/PhysRevA.97.063405`.

[42] V. D. Vaidya, Y. Guo, R. M. Kroeze, K. E. Ballantine, A. J. Kollár, J. Keeling, and B. L. Lev, "Tunable-range, photon-mediated atomic interactions in multimode cavity qed," *Phys. Rev. X*, vol. 8, p. 011 002, 1 2018. [Online]. Available: `https://link.aps.org/doi/10.1103/PhysRevX.8.011002`.

[43] R. Landig, L. Hruby, N. Dogra, M. Landini, R. Mottl, T. Donner, and T. Esslinger, "Quantum phases from competing short- and long-range interactions in an optical lattice," *Nature*, vol. 532, pp. 476–4790, 2016.

[44] F. Dalfovo, S. Giorgini, L. P. Pitaevskii, and S. Stringari, "Theory of bose-einstein condensation in trapped gases," *Rev. Mod. Phys.*, vol. 71, pp. 463–512, 3 1999. [Online]. Available: `https://link.aps.org/doi/10.1103/RevModPhys.71.463`.

[45] B. Olmos, D. Yu, Y. Singh, F. Schreck, K. Bongs, and I. Lesanovsky, "Long-range interacting many-body systems with alkaline-earth-metal atoms," *Phys. Rev. Lett.*, vol. 110, p. 143 602, 14 2013. [Online]. Available: `http://link.aps.org/doi/10.1103/PhysRevLett.110.143602`.

[46] R. H. Lehmberg, "Radiation from an n-atom system. i. general formalism," *Phys. Rev. A*, vol. 2, pp. 883–888, 3 1970. [Online]. Available: `https://journals.aps.org/pra/pdf/10.1103/PhysRevA.2.883`.

[47] D. F. V. James, "Frequency shifts in spontaneous emission from two interacting atoms," *Phys. Rev. A*, vol. 47, pp. 1336–1346, 2 Feb. 1993. [Online]. Available: `https://link.aps.org/doi/10.1103/PhysRevA.47.1336`.

[48] K.-K. Ni, S. Ospelkaus, M. H. G. de Miranda, A. Pe'er, B. Neyenhuis, J. J. Zirbel, S. Kotochigova, P. S. Julienne, D. S. Jin, and J. Ye, "A high phase-space-density gas of polar molecules," *Science*, vol. 322, no. 5899, pp. 231–235, 2008, ISSN: 0036-8075. eprint: `http://science.sciencemag.org/content/322/5899/231.full.pdf`. [Online]. Available: `http://science.sciencemag.org/content/322/5899/231`.

[49] J. Deiglmayr, A. Grochola, M. Repp, K. Mörtlbauer, C. Glück, J. Lange, O. Dulieu, R. Wester, and M. Weidemüller, "Formation of ultracold polar molecules in the rovibrational ground state," *Phys. Rev. Lett.*, vol. 101, p. 133 004, 13 2008. [Online]. Available: https://link.aps.org/doi/10.1103/PhysRevLett.101.133004.

[50] S. Das, G. S. Agarwal, and M. O. Scully, "Quantum interferences in cooperative dicke emission from spatial variation of the laser phase," *Phys. Rev. Lett.*, vol. 101, p. 153 601, 15 2008. [Online]. Available: https://link.aps.org/doi/10.1103/PhysRevLett.101.153601.

[51] D.-w. Wang, Z.-h. Li, H. Zheng, and S.-y. Zhu, "Time evolution, lamb shift, and emission spectra of spontaneous emission of two identical atoms," *Phys. Rev. A*, vol. 81, p. 043 819, 4 2010. [Online]. Available: https://link.aps.org/doi/10.1103/PhysRevA.81.043819.

[52] T. Tokihiro, Y. Manabe, and E. Hanamura, "Superradiance of frenkel excitons in linear systems," *Phys. Rev. B*, vol. 47, pp. 2019–2030, 4 Jan. 1993. [Online]. Available: https://link.aps.org/doi/10.1103/PhysRevB.47.2019.

[53] S. Stellmer, R. Grimm, and F. Schreck, "Production of quantum-degenerate strontium gases," *Phys. Rev. A*, vol. 87, p. 013 611, 1 Jan. 2013. [Online]. Available: https://link.aps.org/doi/10.1103/PhysRevA.87.013611.

[54] T. Nicholson, S. Campbell, R. Hutson, G. Marti, B. Bloom, R. McNally, W. Zhang, M. Barrett, M. Safronova, G. Strouse, W. Tew, and J. Ye, "Systematic evaluation of an atomic clock at 210^{-18} total uncertainty," *Nature Communications*, vol. 6, p. 6896, 2015. [Online]. Available: http://dx.doi.org/10.1038/ncomms7896.

[55] L. Hu, N. Poli, L. Salvi, and G. M. Tino, "Atom interferometry with the Sr optical clock transition," *Phys. Rev. Lett.*, vol. 119, p. 263 601, 26 2017. [Online]. Available: https://link.aps.org/doi/10.1103/PhysRevLett.119.263601.

[56] H. Katori, T. Ido, Y. Isoya, and M. Kuwata-Gonokami, "Laser cooling of strontium atoms towards the quantum degenerate regime," in *Conference Digest. 2000 International Quantum Electronics Conference (Cat. No.00TH8504)*, 2000, 1 pp.–.

[57] G. Ferrari, R. E. Drullinger, N. Poli, F. Sorrentino, and G. M. Tino, "Cooling of Sr to high phase-space density by laser and sympathetic cooling in isotopic mixtures," *Phys. Rev. A*, vol. 73, p. 023 408, 2 Feb. 2006. [Online]. Available: https://link.aps.org/doi/10.1103/PhysRevA.73.023408.

[58] J. A. Giordmaine and T. C. Wang, "Molecular beam formation by long parallel tubes," *Journal of Applied Physics*, vol. 31, no. 3, pp. 463–471, 1960. eprint: https://doi.org/10.1063/1.1735609. [Online]. Available: https://doi.org/10.1063/1.1735609.

[59] C. L. Yaws and K. (Firm), *Chemical properties handbook : physical, thermodynamic, environmental, transport, safety, and health related properties for organic and inorganic chemicals*, English. [Place of publication not identified] : McGraw Hill, 1999, ISBN: 159124028X (electronic bk.) [Online]. Available: `http://accessengineeringlibrary.com/browse/chemical-properties-handbook`.

[60] C. L. Yaws, *Critical Property Data for Chemical Engineers and Chemists*. Knovel, 2012; 2013; 2014, ISBN: N/A. [Online]. Available: `https://app.knovel.com/hotlink/toc/id:kpYCPDCECD/yaws-critical-property/yaws-critical-property`.

[61] N. Ramsey, *Molecular beams*. Oxford University Press, 1985.

[62] M. Inguscio and L. Fallani, *Atomic Physics: Precise Measurements and Ultracold Matter*. Oxford Scholarship Online, 2013.

[63] V. I. Balykin, V. S. Letokhov, and V. I. Mushin, "Observation of the cooling of free sodium atoms in a resonance laser field with a scanning frequency," *JETP Lett.*, vol. 29, p. 560, 10 1979.

[64] I. R. Hill, Y. B. Ovchinnikov, E. M. Bridge, E. A. Curtis, and P. Gill, "Zeeman slowers for strontium based on permanent magnets," *Journal of Physics B: Atomic, Molecular and Optical Physics*, vol. 47, no. 7, p. 075 006, 2014. [Online]. Available: `http://stacks.iop.org/0953-4075/47/i=7/a=075006`.

[65] C. C. Bradley, J. G. Story, J. J. Tollett, J. Chen, N. W. M. Ritchie, and R. G. Hulet, "Laser cooling of lithium using relay chirp cooling," *Opt. Lett.*, vol. 17, no. 5, pp. 349–351, Mar. 1992. [Online]. Available: `http://ol.osa.org/abstract.cfm?URI=ol-17-5-349`.

[66] G. Reinaudi, C. B. Osborn, K. Bega, and T. Zelevinsky, "Dynamically configurable and optimizable zeeman slower using permanent magnets and servomotors," *J. Opt. Soc. Am. B*, vol. 29, no. 4, pp. 729–733, 2012. [Online]. Available: `http://josab.osa.org/abstract.cfm?URI=josab-29-4-729`.

[67] V Lebedev and D. M. Weld, "Self-assembled zeeman slower based on spherical permanent magnets," *Journal of Physics B: Atomic, Molecular and Optical Physics*, vol. 47, no. 15, p. 155 003, 2014. [Online]. Available: `http://stacks.iop.org/0953-4075/47/i=15/a=155003`.

[68] K. Lindquist, M. Stephens, and C. Wieman, "Experimental and theoretical study of the vapor-cell zeeman optical trap," *Phys. Rev. A*, vol. 46, pp. 4082–4090, 7 1992. [Online]. Available: `http://link.aps.org/doi/10.1103/PhysRevA.46.4082`.

[69] C. J. Foot, *Atomic Physicsk*. Oxford University Press, 2005.

[70] T. Bergeman, G. Erez, and H. J. Metcalf, "Magnetostatic trapping fields for neutral atoms," *Phys. Rev. A*, vol. 35, pp. 1535–1546, 4 Feb. 1987. [Online]. Available: `https://link.aps.org/doi/10.1103/PhysRevA.35.1535`.

[71] H. G. C. Werij, C. H. Greene, C. E. Theodosiou, and A. Gallagher, "Oscillator strengths and radiative branching ratios in atomic sr," *Phys. Rev. A*, vol. 46, pp. 1248–1260, 3 1992. [Online]. Available: https://link.aps.org/doi/10.1103/PhysRevA.46.1248.

[72] P. G. Mickelson, Y. N. M. de Escobar, P Anzel, B. J. DeSalvo, S. B. Nagel, A. J. Traverso, M Yan, and T. C. Killian, "Repumping and spectroscopy of laser-cooled sr atoms using the (5s5p) $^3p_2$ –(5s4d) $^3d_2$ transition," *Journal of Physics B: Atomic, Molecular and Optical Physics*, vol. 42, no. 23, p. 235 001, 2009. [Online]. Available: http://stacks.iop.org/0953-4075/42/i=23/a=235001.

[73] T. H. Loftus, T. Ido, M. M. Boyd, A. D. Ludlow, and J. Ye, "Narrow line cooling and momentum-space crystals," *Phys. Rev. A*, vol. 70, p. 063 413, 6 2004. [Online]. Available: https://link.aps.org/doi/10.1103/PhysRevA.70.063413.

[74] L. L. Smith, "A transportable strontium optical lattice clock towards space," PhD thesis, University of Birmingham, 2016.

[75] H. Katori, T. Ido, Y. Isoya, and M. Kuwata-Gonokami, "Magneto-optical trapping and cooling of strontium atoms down to the photon recoil temperature," *Phys. Rev. Lett.*, vol. 82, pp. 1116–1119, 6 Feb. 1999. [Online]. Available: https://link.aps.org/doi/10.1103/PhysRevLett.82.1116.

[76] T. H. Loftus, T. Ido, A. D. Ludlow, M. M. Boyd, and J. Ye, "Narrow line cooling: Finite photon recoil dynamics," *Phys. Rev. Lett.*, vol. 93, p. 073 003, 7 2004. [Online]. Available: https://link.aps.org/doi/10.1103/PhysRevLett.93.073003.

[77] R. Grimm, M. Weidemüller, and Y. B. Ovchinnikov, "Optical dipole traps for neutral atoms," in, ser. Advances In Atomic, Molecular, and Optical Physics, B. Bederson and H. Walther, Eds., vol. 42, Academic Press, 2000, pp. 95 –170. [Online]. Available: http://www.sciencedirect.com/science/article/pii/S1049250X0860186X.

[78] I. R. Hill, "Development of an apparatus for a strontium optical lattice optical frequency standard," PhD thesis, Department of Physics Imperial College London, 2007.

[79] J. E. Sansonetti and G. Nave, "Wavelengths, transition probabilities, and energy levels for the spectrum of neutral strontium (sri)," *Journal of Physical and Chemical Reference Data*, vol. 39, no. 3, p. 033 103, 2010. eprint: https://doi.org/10.1063/1.3449176. [Online]. Available: https://doi.org/10.1063/1.3449176.

[80] O. J. Luiten, M. W. Reynolds, and J. T. M. Walraven, "Kinetic theory of the evaporative cooling of a trapped gas," *Phys. Rev. A*, vol. 53, pp. 381–389, 1 Jan. 1996. [Online]. Available: https://link.aps.org/doi/10.1103/PhysRevA.53.381.

[81] A. Derevianko and H. Katori, "Colloquium: Physics of optical lattice clocks," *Rev. Mod. Phys.*, vol. 83, pp. 331–347, 2 2011. [Online]. Available: https://link.aps.org/doi/10.1103/RevModPhys.83.331.

[82] A. Kaplan, M. Fredslund Andersen, and N. Davidson, "Suppression of inhomogeneous broadening in rf spectroscopy of optically trapped atoms," *Phys. Rev. A*, vol. 66, p. 045 401, 4 2002. [Online]. Available: https://link.aps.org/doi/10.1103/PhysRevA.66.045401.

[83] K. I. Lee, J. A. Kim, H. R. Noh, and W. Jhe, "Single-beam atom trap in a pyramidal and conical hollow mirror," *Opt. Lett.*, vol. 21, no. 15, pp. 1177–1179, 1996. [Online]. Available: http://ol.osa.org/abstract.cfm?URI=ol-21-15-1177.

[84] S. Pollock, J. P. Cotter, A. Laliotis, and E. A. Hinds, "Integrated magneto-optical traps on a chip using silicon pyramid structures," *Opt. Express*, vol. 17, no. 16, pp. 14 109–14 114, 2009. [Online]. Available: http://www.opticsexpress.org/abstract.cfm?URI=oe-17-16-14109.

[85] M. Vangeleyn, P. F. Griffin, E. Riis, and A. S. Arnold, "Single-laser, one beam, tetrahedral magneto-optical trap," *Opt. Express*, vol. 17, no. 16, pp. 13 601–13 608, 2009. [Online]. Available: http://www.opticsexpress.org/abstract.cfm?URI=oe-17-16-13601.

[86] ——, "Laser cooling with a single laser beam and a planar diffractor," *Opt. Lett.*, vol. 35, no. 20, pp. 3453–3455, 2010. [Online]. Available: http://ol.osa.org/abstract.cfm?URI=ol-35-20-3453.

[87] G. Rosi, L. Cacciapuoti, F. Sorrentino, M. Menchetti, M. Prevedelli, and G. M. Tino, "Measurement of the gravity-field curvature by atom interferometry," *Phys. Rev. Lett.*, vol. 114, p. 013 001, 1 Jan. 2015. [Online]. Available: https://link.aps.org/doi/10.1103/PhysRevLett.114.013001.

[88] M. Schioppo, "Development of a transportable strontium optical clock," PhD thesis, Universitá degli studi di Firenze, Dipartimento di Fisica e Astronomia, 2010.

[89] M. Mauck, "Knife-edge profiling of Q-switched Nd:YAG laser beam and waist," *Appl. Opt.*, vol. 18, no. 5, pp. 599–600, Mar. 1979. [Online]. Available: http://ao.osa.org/abstract.cfm?URI=ao-18-5-599.

[90] J. M. Khosrofian and B. A. Garetz, "Measurement of a gaussian laser beam diameter through the direct inversion of knife-edge data," *Appl. Opt.*, vol. 22, no. 21, pp. 3406–3410, 1983. [Online]. Available: http://ao.osa.org/abstract.cfm?URI=ao-22-21-3406.

[91] R. W. P. Drever, J. L. Hall, F. V. Kowalski, J. Hough, G. M. Ford, A. J. Munley, and H. Ward, "Laser phase and frequency stabilization using an optical resonator," *Applied Physics B*, vol. 31, no. 2, pp. 97–105, 1983, ISSN: 1432-0649. [Online]. Available: https://doi.org/10.1007/BF00702605.

[92] S. Johnson, "Narrow linewidth lasers for use with neutral strontium as a frequency standard by," PhD thesis, University of Birmingham, 2013.

[93] F. J. Duarte, *Tunable Lasers Handbood*, ser. Optics and photonics. Academic press, 1995.

[94] M. Boshier, D. Berkeland, E. Hinds, and V. Sandoghdar, "External-cavity frequency-stabilization of visible and infrared semiconductor lasers for high resolution spectroscopy," *Optics Communications*, vol. 85, no. 4, p. 355, 1991, ISSN: 0030-4018. [Online]. Available: `http://www.sciencedirect.com/science/article/pii/0030401891904905`.

[95] P. Zorabedian and W. R. Trutna, "Interference-filter-tuned, alignment-stabilized, semiconductor external-cavity laser," *Opt. Lett.*, vol. 13, no. 10, p. 826, 1988. [Online]. Available: `http://ol.osa.org/abstract.cfm?URI=ol-13-10-826`.

[96] X. Baillard, A. Gauguet, S. Bize, P. Lemonde, P. Laurent, A. Clairon, and P. Rosenbusch, "Interference-filter-stabilized external-cavity diode lasers," *Optics Communications*, vol. 266, no. 2, pp. 609 –613, 2006, ISSN: 0030-4018. [Online]. Available: `http://www.sciencedirect.com/science/article/pii/S0030401806004561`.

[97] N. Seymour-Smith, P. Blythe, M. Keller, and W. Lange, "Fast scanning cavity offset lock for laser frequency drift stabilization," *Review of Scientific Instruments*, vol. 81, no. 7, p. 075 109, 2010. eprint: `https://doi.org/10.1063/1.3455830`. [Online]. Available: `https://doi.org/10.1063/1.3455830`.

[98] N. Ramsey, *Molecular Beams*. Oxford University Press, 1956.

[99] S. B. Nagel, C. E. Simien, S. Laha, P. Gupta, V. S. Ashoka, and T. C. Killian, "Magnetic trapping of metastable $^3p_2$ atomic strontium," *Phys. Rev. A*, vol. 67, p. 011 401, 1 Jan. 2003. [Online]. Available: `https://link.aps.org/doi/10.1103/PhysRevA.67.011401`.

[100] M. Boyd, "High precision spectroscopy of strontium in an optical lattice: Towards a new standard for frequency and time," PhD thesis, Jila, 2007.

[101] I. Courtillot, A. Quessada, R. P. Kovacich, J.-J. Zondy, A. Landragin, A. Clairon, and P. Lemonde, "Efficient cooling and trapping of strontium atoms," *Opt. Lett.*, vol. 28, no. 6, pp. 468–470, Mar. 2003. [Online]. Available: `http://ol.osa.org/abstract.cfm?URI=ol-28-6-468`.

[102] G. S. Cassany, "Cold atom physics using ultra-thin optical fibre," PhD thesis, Faculty of Mathematics and Natural Sciences Rheinische Friedrich-Wilhelms-University Bonn, 2008.

[103] G. Nootz. (2012). Fit 2d gaussian function to data, [Online]. Available: `https://uk.mathworks.com/matlabcentral/fileexchange/37087-fit-2d-gaussian-function-to-data`.

[104] G. H. Newsom, S O'Connor, and R. C. M. Learner, "Re-examination of the spectrum of strontium: Autoionization in the spectrum of neutral strontium," *Journal of Physics B: Atomic and Molecular Physics*, vol. 6, no. 10, p. 2162, 1973. [Online]. Available: `http://stacks.iop.org/0022-3700/6/i=10/a=028`.

[105] S. Stellmer, M. K. Tey, B. Huang, R. Grimm, and F. Schreck, "Bose-einstein condensation of strontium," *Phys. Rev. Lett.*, vol. 103, p. 200 401, 20 2009. [Online]. Available: `https://link.aps.org/doi/10.1103/PhysRevLett.103.200401`.

[106] P. G. Mickelson, Y. N. Martinez de Escobar, M. Yan, B. J. DeSalvo, and T. C. Killian, "Bose-einstein condensation of ^{88}Sr through sympathetic cooling with ^{87}Sr," *Phys. Rev. A*, vol. 81, p. 051 601, 5 2010. [Online]. Available: `https://link.aps.org/doi/10.1103/PhysRevA.81.051601`.

[107] R. Wiegner, J. von Zanthier, and G. S. Agarwal, "Quantum-interference-initiated superradiant and subradiant emission from entangled atoms," *Phys. Rev. A*, vol. 84, p. 023 805, 2 2011. [Online]. Available: `https://link.aps.org/doi/10.1103/PhysRevA.84.023805`.

[108] S. D. Jenkins and J. Ruostekoski, "Controlled manipulation of light by cooperative response of atoms in an optical lattice," *Phys. Rev. A*, vol. 86, p. 031 602, 3 2012. [Online]. Available: `https://link.aps.org/doi/10.1103/PhysRevA.86.031602`.